INVESTIGATION OF GH_2-GO_2 COMBUSTION

NAS 3-14379

Prepared For

NASA Lewis Research Center
Cleveland, Ohio 44135

Quarterly Report No. 2 — 15 January 1972

AEROJET LIQUID ROCKET COMPANY
A DIVISION OF AEROJET-GENERAL
SACRAMENTO, CALIFORNIA

QUARTERLY REPORT NO. 2

For Period Ending 26 December 1971

INVESTIGATION OF GH_2-GO_2 COMBUSTION

NAS 3-14379

D. F. Calhoon

15 January 1972

Design and Analysis Department
Aerojet Liquid Rocket Company
Sacramento, California

Prepared for

NASA-Lewis Research Center
Cleveland, Ohio 44135

Approved by:

D. L. Kors
Project Manager
Gas-Gas Combustion Program

AEROJET LIQUID ROCKET COMPANY

SACRAMENTO, CALIFORNIA • A DIVISION OF AEROJET-GENERAL

TABLE OF CONTENTS

FIGURE LIST

Figure List (cont.)

I. INTRODUCTION

The objective of this program is the development of an injector/combustion technology base for gaseous hydrogen-gaseous oxygen rocket engines. The end product of the program will be a design guide which includes a characterization of the injection process while relating high combustion performance and injector/chamber interactions to the design variables. Mr. L. Gordon is the NASA Lewis Research Center program manager.

In order to accomplish this objective, a six-task program is planned. Briefly, this program is structured to investigate the gas-gas mixing process from both an analytical and empirical viewpoint. Task I evaluates potential injector design concepts, culminating in selection of four element concepts worthy of further empirical investigation. Task II encompasses the fabrication, cold and combustion flow testing, and resulting data analysis of three of the four elements selected in Task I. The three element concepts cold flowed in Task II will be hot-fire tested in Task III with the intent of relating the cold flow data of Task II to the resulting single element performance and compatibility data generated in Task III. Three full-scale injectors will be designed, fabricated, and tested in Task IV. The designs will be based on the analytical and empirical information gathered in the preceding tasks. Data from Task II, Task III, and Task IV will be analyzed and correlated with the results of Task I during Task V. These correlations will form the substance of the design guide. Task VI includes the reporting requirements of the entire program.

During this reporting period, the Task II hardware was fabricated; the single-element cold flow data were generated; and the single-element hot flow data were generated. All of the above data were reduced and a large portion of the data was analyzed. The hot fire stand of Task III was fabricated and is awaiting delivery of hardware. The single-element chambers were designed as part of this task. Testing of this hardware is scheduled to begin in mid-January.

I, Introduction (cont.)

A large portion of this quarter's effort was directed at obtaining and analyzing data from prototype GO_2-GH_2 injection elements. The bulk of this testing was conducted with nonreacting propellants, N_2 to simulate the O_2 and H_2. A limited number of tests were conducted in a combusting environment, with the purpose of this testing being to evaluate the effects of combustion on cold flow mixture ratio and mass profiles. The cold flow testing was completed in 223 tests. E_m and E_c data have been generated for these data. Analytical model correlations of these data are well under way and will be completed in the next reporting period. The hot flow testing was completed in 36 tests; those data have been reduced and are documented in this report.

From these data, a number of significant conclusions can be drawn. These are listed as follows:

- Swirl and premix concepts are high mixing elements, insensitive to operating conditions.
- Triplet element potentially high performing, but very sensitive to design and operating variables.
- Parallel sheet element promising for HIPERTHIN application, better than doublet.
- Increased-shear elements increase mixing but not enough to warrant additional fabrication complexity.
- Coaxial element is poor mixing concept, sensitive to operating conditions.
- Combustion does impede the mixing process.

II. TECHNICAL PROGRESS SUMMARY

A. TASK I - INJECTOR DESIGN AND ANALYSIS

This task is complete.

B. TASK II - COLD FLOW MODEL FABRICATION

Fabrication of the various elements was completed. These elements are illustrated in Figure 1.

A hot flow probe was constructed and the existing chamber was modified to accommodate the hot probe at three axial stations. The probe is constructed of three concentric tubes. The combustion sample is drawn through the center tube and is routed to the mass spectrometer via heated tubing. The outer two tubes form the passage for entry and return of the probe coolant fluid. In this case, H_2 at approximately 250°F is used as coolant. The high temperature is required to ensure that the H_2O present in the combustion sample will be maintained in the vapor phase. This temperature is maintained throughout the system. All lines and valves associated with the mass spectrometer are steam jacketed or electrically heated. The hot flow chamber is also cooled with a high pressure steam jacket.

The cold flow chamber has been modified for the hot flow testing. Sampling bosses have been added at axial locations of 3.09, 5.15, and 7.17 in. (7.84, 13.08, and 18.2 cm) from the injector face. These locations correspond to probe locations of 11.8, 19.7, and 27.5 ox tube diameters away from the injector face.

The multiple elements have not been fabricated and will be committed to fabrication after initial analysis of the single-element cold flow data.

II, Technical Progress Summary (cont.)

C. TASK IIB - COLD FLOW MODEL TESTING AND ANALYSIS

1. Summary

During this period a significant portion of this task was completed. The single-element testing was concluded; data reduction and analysis programs were reduced to practice; and the analysis effort was initiated and is nearing completion.

In addition, the hot flow testing of this program was completed. The intent of this testing was to ascertain if combustion could influence the cold flow mixing work. The results of this testing do indeed indicate adverse influence on mixing profiles. In general, combustion inhibits mixing so that increased chamber length is required to complete the mixing process.

The cold flow data have been dumped onto master tape files. The basic engineering unit reduction has been completed for these tests and all tests have been reduced to the form of mass and mixture ratio profiles, complete with E_m, E_c, and other pertinent derived parameters (e.g., velocity ratio, momentum ratio, and Rupe number). Mixture ratio profiles have been developed that relate the combustion case to the identical cold flow analog.

The engineering unit file program is discussed. This program reduces the raw data to meaningful engineering parameters-such as weight flows, pressures mole fractions, temperatures and pressures-and formats the resulting data in an orderly array arranged sequentially by time and probe position. These data are then input into the Data Analysis Computer Program (DATNAL) where the key test analysis parameters are computed. Discussed in the bulk of this section are the techniques by which this program yields the parametric test data: the local mass and mixture ratio matrices, the compatibility coefficient (E_c), and the mixing coefficient (E_m).

II, C, Task IIB - Cold Flow Model Testing and Analysis (cont.)

Also included in this section is a discussion of the technique by which these parameters are evaluated. Although base bleed flow was utilized to suppress recirculation, a certain amount of recirculation could not be avoided. This is manifested in an overintegration of mass. That is, the program integrates more mass than is actually present. With base bleed, this excess mass was typically about 50% of the incoming mass flow. This was handled by only integrating radially to the point where the measured mass flux equaled the integrated flux. As an additional check, the data are tested for O/F consistency. This was established by inspection of the integrated O/F with the test O/F. Closure within 20% was defined as being valid data.

Results of the initial data analysis are presented. The results are in qualitative agreement with other cold flow testing conducted in support of the APS program. The swirl coaxial is a high mixing potential element. The increased shear element is better (higher E_m) than the coaxial but not as efficient as the swirler. The coaxial and increased shear element are sensitive to design and operating point while the swirler is not (or at least is only slightly sensitive). The external impinging triplet has potential but is extremely sensitive to both a good mixing operating point and geometry variables. The premix designs (both the triplet and pentad) are high mixing potential elements and are influenced only slightly be design and operating variables.

Also included in this quarterly report is the modeling of the cold flow data to reduce the data to a set of equations that relate the variables to each other and mixing efficiency. Modeling has been completed for the coaxial, like doublet, and parallel sheet elements and the applicable test data has been correlated. The model is based on boundary layer approximations and has the ability to predict the effects of length, element area ratio, mixture ratio, size, propellant temperature, and impingement angle.

II, C, Task IIB - Cold Flow Model Testing and Analysis (cont.)

The hot flow testing was completed during the period. This testing was conducted at one atmosphere, with the identical swirl coaxial element tested in the cold flow portion of the program. The intent of this testing was to ascertain if combustion influenced the data obtained in cold flow. The results indicate that, in fact, combustion does impede the mixing process.

2. Data Acquisition and Reduction

a. The Engineering Unit File Computer Program

The initial step in reduction of a typical cold flow test was creation of a tape Engineering Unit File (E.U.F.) and paper listing. Figure 2 shows the digital data listing for Test 122 (Run 129) of the cold test program. The E.U.F. program operates with tape input from the master raw data storage system. Card input to the E.U.F. program has been limited to the flow coefficients for the oxidizer, fuel, and helium upstream critical orifices.

The E.U.F. program lists rake pressure and composition data on the first page of the printout. The position number in column two indicates the rake position being sampled. The composition and pressure lists indicate whether the rake data at the time indicated are in the pressure or composition mode, "yes" being an affirmative answer to either. The uncorrected rake delta pressure is shown in column three. The raw signal is recorded over the linear range of the ΔP transducer and transmitted with the units psia/volt. Stepper position 21 records the transducer tare (i.e., zero shift). To obtain the summary delta pressure readings (shown on page 5 of Figure 2), the ΔP tare of position 21 is subtracted from the pressure reading of each rake position. These pressures are utilized in the data analysis program to calculate local mass fluxes. When the composition sampling process is taking place, the mole fraction data of columns 6 to 9 (page 1) become meaningful. For the particular test shown, the mass spectrometer

monitored H_2, He, N_2 on channels 26 to 28, respectively. Two corrections are made to specie mole fraction data before entering it in the E.U.F. summary table. The raw mass spectrometer peak voltage reading (for a particular species) is reduced according to the average voltage residual recorded during the time in which pressure data are being sampled. That is, the mass spectrometer transmits a small voltage reading (on the order of ten percent of a typical steady-state peak height sample) when it is not actually sampling gas, which is subtracted from regular composition voltage values. The second correction involves adjusting the mole fraction data to maintain consistency with a known composition calibration gas, sampled by the mass spectrometer in Stepper Switch position 22. Essentially, the calibration gas is utilized to calculate the constants K_1, K_2, and K_3 in the following equation. The equation is derived from the fact that the partial pressure of a particular species is proportional to its mole fraction in a gaseous mixture.

$$X_1 = \frac{K_1 \cdot P_{H1}}{K_1 \cdot P_{H1} + K_2 \cdot P_{H2} + K_3 \cdot P_{H3}}$$

where: X_1 = mole fraction of species one
P_{H1} = mass spectrometer peak height voltage for species one
P_{H2} = mass spectrometer peak height voltage for species two
P_{H3} = mass spectrometer peak height voltage for species three

When both of the aforementioned adjustments have been made, the composition data for each rake position are entered in the E.U.F. summary table.

The remaining three columns of page 1 of Figure 2 show the time-based test weight flows. They are calculated with the compressible sonic flow equation shown below, based on measured upstream orifice total pressures and temperatures.

$$\dot{w}_{sonic} = A\, C_d \cdot P_o \sqrt{\frac{\gamma \cdot g}{R \cdot T_o} \left(\frac{2}{\gamma+1}\right)^{\frac{\gamma+1}{\gamma-1}}}$$

On page 3, the remaining time-based system variables are listed. Manifold temperatures were calculated with standard chromel-alumel thermocouple response curves contained within the E.U.F. program. The three manifold and one chamber pressure transducers measure gauge pressures recorded in the units millivolts/psig, the E.U.F. program converting to psia. The remaining total and static pressures read the rake pressure data.

The test system variables are averaged over the entire test period and are shown at the top of the test summary page of Figure 2. The data for each rake position are listed for both the average of the number of samples taken with that probe and the last sample output taken with the probe. For the test shown, only one scan was taken for each probe position. Since steady-state pressure and composition data are obtained with the first sample, subsequent scans are not required. The data summary as shown is stored on tape and readily available for direct input to the data analysis program, DATNAL.

b. The Data Analysis Computer Program (DATNAL)

Following tape storage of the engineering unit file summary block, the data analysis program computes the key test analysis parameters. Figure 3 is a seven-page detail of the DATNAL output for Test 122 (Run 129). DATNAL reads the engineering file for the particular test from tape. Input is completed by card read-in of the particular element geometric variables (flow area and injection angle).

Parametric test data comprise the first output block of DATNAL as shown on page 1 of Figure 3. The following block details the calculated injection variables, to be used for correlative type analysis. The 24 variables listed are calculated in a separate program subroutine, based on element flow areas, manifold temperatures and pressures, chamber pressure, and measured mass flow rates. The continuity equation is the basis of calculation for parameters, including injection velocity terms.

Page 2 of the DATNAL listing shows the measured ΔP and static pressure matrices. The data for the outside four radial positions was flopped from quadrant one (bounded by the 0- and 90-degree radial positions) to fill the nonmeasured quadrants. Figure 18 of Reference 1 shows the rake element locations. Probe 1 lies on the zero-degree boundary, while probe 8 lies on the ninety-degree boundary. The measured total pressure matrix is calculated by adding corresponding terms of the delta pressure and static pressure matrices.

Pages 4, 5 and 6 of Figure 3 detail the local mass flux and mixture ratio calculations performed in DATNAL. The local mixture ratio matrix is calculated with the equation shown below, from the mole fraction data obtained from the E.U.F. program.

$$(O/F)_L = \frac{(MF_{N2})_L \times MW_{N2}}{(MF_{H2})_L \times MW_{H2}}$$

where:
MF_{N2} = local nitrogen mole fraction
MF_{H2} = local hydrogen mole fraction
MW_{N2} = molecular weight of nitrogen
MW_{H2} = molecular weight of hydrogen

The subsonic compressible flow equation is used to calculate the local total mass flux.

Ref. 1 - Calhoon, D. F., Investigation of GH_2-GO_2 Combustion Quarterly Rpt. No. 1, 11 October 1971

$$\dot{w} = A \cdot C_d \cdot P_o \sqrt{\frac{2g\,\gamma}{(\gamma-1)\,RT_o}\left[\left(\frac{P_s}{P_o}\right)^{\frac{2}{\gamma}} - \left(\frac{P_s}{P_o}\right)^{\frac{\gamma+1}{\gamma}}\right]}$$

The gaseous mixture properties (ratio of specific heats, molecular weight) used to solve the equation are calculated based on the mole fraction data input from the E.U.F. program. In essence, local properties are obtained for the flowing mixture based on mass or mole weighting local nitrogen, hydrogen, and helium properties. The local oxidizer flux and fuel matrices of page 3 were obtained by multiplying the respective local mass flows by the associated nitrogen and hydrogen mass fraction, respectively. Through the first five pages of output, DATNAL has essentially summarized the chamber flow field on a local basis.

On page 6 of the DATNAL output, the local compatibility coefficient (E_c) is displayed for the chamber flow field. E_c is calculated from the following equation, the development of which is detailed in Reference 1.

$$E_c = \frac{DB_\ell \left(\frac{\dot{w}}{A}\right)_\ell^{0.8} \left(\frac{1}{1 + T_{wg}/T_o}\right)_\ell^{0.8} (T_o - T_{wg})_\ell}{DB_n \left(\frac{\dot{w}}{A}\right)^{0.8} \left(\frac{1}{1 + T_{wg}/T_o}\right)_n^{0.8} (T_o - T_{wg})_n}$$

E_c is currently being calculated on a local basis only for all cold flow tests. Further treatment of E_c will be made during the next reporting period. The differences in local mass distribution inherent between cold flow tests and hot firings make the $\frac{\dot{w}}{A}$ term in the E_c calculation worthy of investigation. For this reason, calculation of E_c may change after correlations are performed between cold and hot tests. Also for the above reason, a single integrated E_c value has not been calculated for cold flow tests to date.

II, C, Task IIB - Cold Flow Model Testing and Analysis (cont.)

After the local mass flux and mixture ratio matrices have been established, DATNAL characterizes the total chamber flow field. The total, fuel, and oxidizer local mass flux matrices are integrated over the entire chamber. Page 7 displays the integrated flow rates, values being computed from chamber centerline through six radial positions (five rake element locations and the wall). The integrated mixture ratio through any radial location is calculated by dividing the integrated oxidizer flow rate by the integrated fuel flow rate. Typically, integrated flow rates do not equal measured flow rates when the entire chamber flow field is examined. Most tests are characterized by higher than measured integrated flow rates; the reason is suspected to be chamber recirculation zones. To characterize all cold flow tests on a common basis, key analysis parameters are typically compared at the radial location, $\bar{R}$. $\bar{R}$ is the radial location at which the integrated mass flow rate (oxidizer and fuel) equals the measured flow rate. If the flow field integrates low, $\bar{R}$ is equated to the chamber wall radius (0.75 in.).

The analysis parameters E_m, N_m and percent c* are also shown on page 7. E_m is the mixing coefficient, defined by the equation below with the nomenclature defined in Reference R.

$$E_m = 100 \left[1 - \sum_{o}^{n} \frac{A_i M_{ti}}{\dot{w}_o} \left(\frac{\dot{w}_o}{\dot{w}_t} - \frac{M_{oi}}{M_{ti}} \right) \right] \Bigg/ \left[- \sum_{n}^{\bar{n}} \frac{A_i M_{ti}}{\dot{w}_f} \left(\frac{\dot{w}_o}{\dot{w}_t} - \frac{M_{oi}}{M_{ti}} \right) \right]$$

E_m is the central parameter in cold flow element modeling. It is calculated for the six flow regions formed by considering each rake probe radial location to be the outside flow streamline. E_m is also calculated at $\bar{R}$ by interpolating between the E_m values at the bounding radial positions. The $\bar{R}$ E_m is the value which is usually utilized in intra- and inter-element correlative analysis. The E_m function and its role in analysis of the cold flow tests is more thoroughly discussed in Section II,C,3, Data Analysis and Correlation.

N_m (ETAM on page 7) is a mass-weighted mixture ratio distribution term defined by the following equation:

$$N_m = 100 \left[\sum_{o}^{n} \left(\frac{\dot{w}_i}{\dot{w}_t} \right) \times \frac{(O/F)_i}{(O/F)_o} + \sum_{n}^{\bar{n}} \left(\frac{\dot{w}_i}{\dot{w}_t} \right) \left(\frac{(O/F)_o}{(O/F)_i} \right) \right]$$

where:

$\dot{w}_i$ = local total mass flux (oxidizer + fuel)

$\dot{w}_t$ = measured total mass flux, lb/sec-in.^{2}

$(O/F)_i$ = local mixture ratio

$(O/F)_o$ = measured mixture ratio

n = number of samples in which $(O/F)_i < (O/F)_o$

$\bar{n}$ = number of samples in which $(O/F)_i > (O/F)_o$

Effectively, N_m indicates the mass-weighted deviation from nominal mixture ratio. N_m is calculated through the same flow field boundaries as E_m. Its value at $\bar{R}$ is also characterized in the last data block on page 7 of DATNAL. Percent nominal c* is the final analysis parameter calculated in DATNAL. Based on a 300 psia GO_2-GH_2 propellant combination and the test local mixture ratio matrix, a local characteristic exhaust velocity matrix is established by interpolating with a mixture ratio versus c* data block located in DATNAL. The local c* distribution is mass-weighted, integrated, and divided by the total integrated mass flow rate to produce a c* value characteristic of a particular test. Percent nominal c* is found by dividing test c* by nominal c* at the flow field integrated mixture ratio. Percent c* is calculated for the same regions and at $\bar{R}$ in similar manner to E_m and N_m.

3. Data Analysis and Correlation

As described in the preceding paragraphs, the test data points have been reduced through DATNAL using automated data reduction techniques. These tests are summarized on Figure 4. Figure 4 tabulates a brief description of the injection element design parameters, some basic operating parameters, injection parameters, and calculated mixing efficiency parameters. Other additional correlating parameters are calculated and tabulated on individual DATNAL output sheets for each test (see Figure 3, page 1 of 7) for more detailed analysis and correlation but were omitted from Figure 4 for brevity and conciseness. Figure 4 is an informal work sheet and should be considered preliminary data.

a. Theoretical Background

Figure 5 is a pictorial representation of the cold flow field downstream of a typical shear coaxial element within the mixing (combustion) chamber. A high velocity axial jet exists at the chamber axis at the injector face plane. A null injection zone occurs immediately outboard of the active element to the chamber half-radius. A porous (Rigimesh) injector face plate bleeds helium from the half-radius to the chamber wall, resulting in a helium gas velocity on the order of 4.6 meters/sec (15 fps). Due to momentum transfer between the injected gas jet and relatively quiescent gases in the chamber, the jet velocity decelerates and the jet boundary spreads. Although the helium bleed is intended to suppress flow recirculation, the cold flow data indicate it is not entirely successful in doing so. The element jet entrains a portion of the chamber gases and accelerates it downstream. This results in an aspiration effect, resulting in a low static pressure zone around the element which creates a flow recirculating annulus between the element and helium bleed flow. The helium-rich flow is forced against the chamber wall and it also has its own recirculation zone.

The ideal situation would be to start integrating the oxidizer and fuel mass fluxes at the chamber axis and proceed radially outward until the integrated total mass flow rate (oxidizer plus fuel) identically equals the sum of the measured oxidizer and fuel flow rates and to also have the integrated O/F be identically equal to the measured (input) mixture ratio. The radial position at which the integrated flow rate equals the measured flow rate is defined as $\bar{R}$ and the mixing efficiency calculated from all the mass contained within $\bar{R}$ is the primary choice for the data correlation.

However, since the fuel element is outboard of the oxidizer in the coaxial, flat "I", pentad, and external impinging F-O-F triplets, the fuel diffuses radially outward faster than the oxidizer, resulting in an integrated O/F which is usually on the order of 15% higher than measured O/F. Since E_m is normalized on the basis of integrated O/F, it may sometimes be desirable to evaluate E_m at some radial position (usually outboard) other than $\bar{R}$ in which the integrated O/F is closer to measured O/F. The automated data reduction program sets all negative dynamic pressures at zero and assumes stationary flow in the negative velocity recirculation zones because the sampling probe is not calibrated to accurately determine the magnitude of negative dynamic heads. On the other hand, all positive dynamic heads are assumed to be element flow in the forward direction and its flow rate is integrated even if it is that portion of the recirculation zone flowing in the forward direction (see Figure 5). Thus, it is not surprising that, if all flow in the positive direction is integrated from the chamber axis to the wall (r = 1.9 cm), the integrated mass flow rate is on the order of 50% to 100% higher than the measured flow rate. The local mixture ratio of probe positions beyond $\bar{R}$ and in the recirculation zone are usually fuel rich compared to the oxidizer-rich regions near the axis. The reason can be seen from Figure 5.

Because of the recirculatory flow field, the simplifying mathematical assumption of irrotational flow cannot be made to define the flow stream function and velocity potential. However, a qualitative schematic cartoon depicting possible "stream functions" and pseudo-equipotential "velocity potentials" is shown on Figure 5 for clarity of discussion. The maximum velocity potential occurs at the injection element plane. The potential function decreases as the jet diffuses and the streamlines diverge. The potential function decreases in a fan about the circulation point which acts like a vortex eye in the recirculation region. The minimum potential in the recirculation region occurs on a surface between the eye and the maximum potential surface at the element exit. The magnitude of the step discontinuity in the velocity potential is dependent upon the strength of the vortex circulation. The latter, in turn, is dependent on the physical spacing between the eye and jet boundary and the reduced potential recirculation gas which is accelerated by the high velocity potential jet through viscous shear forces. However, because of the rotational flow circulation induced discontinuity in the velocity potential immediately outside the element jet, a strong velocity potential gradient exists in the radial as well as axial direction. This causes the outer gas (fuel) stream function to rapidly diffuse radially outward, becoming quickly entrained in the fuel-rich recirculation zone leaving the jet core to be oxidizer-rich relative to the measured or injected O/F. The numerical values assigned to the velocity potentials shown on Figure 5 are shown to enhance conceptual understanding only and are not indicative of a quantitative analysis.

Extensive effort has been taken to understand the basic flow and mixing mechanism so that the DATNAL computer program can be modified to the extent necessary to reflect accurate and meaningful data and injection parameters prior to any attempt to correlate data. This was considered to be necessary because of the large mass of data acquired on this cold flow test program. It would be better to check the data in great detail first and acquire high confidence in the basic data rather than attempt correlations of low confidence data and encounter correlative anomalies later. With this in mind, the

data on Figure 4 are separated into groups of variable confidence ratings. After scanning the local mass and mixture ratio distributions at each probe position for reasonableness on each test, the integrated O/F was compared to the measured O/F at $\bar{R}$; if integrated O/F is within $\pm$20% of measured O/F at $\bar{R}$, the E_m value at $\bar{R}$ is given a high confidence rating indicated by an asterisk to the left of the test number in Figure 4. Of course, this assumes $\bar{R}$ is a reasonable value consistent with similar element types, thrust per element (F/E) and axial position (L/D). Furthermore, the E_m at $\bar{R}$ is compared vs E_m values evaluated at other nearby radial positions to check the sensitivity of E_m to assumed radial boundary.

If these conditions are not satisfied, it may be preferable to evaluate E_m at another radial boundary where the integrated O/F is closer to the measured O/F. A second condition of acceptability was selected for which integrated O/F is within $\pm$10% of measured O/F and the integrated oxidizer plus fuel flow rate is within $\pm$25% of measured flow rates. If this condition is satisfied, the data point is likewise indicated by an asterisk. On some tests, the integrated O/F is always biased higher or lower than the measured O/F at all radial positions. Nevertheless, the data are considered acceptable if the deviation from perfect mixing $(1 - E_m)$ varied by less than $\pm$10% at all reasonable radial boundaries; e.g., if E_m = 50% $\pm$ 5%, 80% $\pm$ 2%, 90% $\pm$ 1%, etc., at any radius. A fourth condition of acceptability is if E_m is between 90% to 100% and does not vary by more than $\pm$1% from a nominal value over a wide range of radii, it is indicated by an asterisk.

All tests marked by an asterisk on Figure 4 are considered to be sufficiently accurate or insensitive to variation that they may be considered ready for data correlation. Some tests are characterized by widely varying values of E_m which are usually indicative of radial mixture ratio variations. Since the uncertainty associated with these tests may prejudice the data

correlations a tentiative compromise value or a "most probable" value is indicated by an open diamond symbol (◇) to the left of the test number column on Figure 4. These values when used in any potential correlation, are specially marked and viewed with suspicion until they are compared with similar elements, similar test conditions, similar L/D, etc., until the credibility of their data is established. The values in Figure 4 have been treated in this manner and represent the best possible value for that particular test.

b. Cold Flow Data Analysis

The pertinent cold flow data of this program have been reduced by the techniques discussed earlier in this report. The resulting data are displayed in graphical form in Figures 6 through 42. The first four figures are summary graphs of ERE for all injectors as a function of thrust per element (F/E), length, element area ratio (A_f/A_o), and mixture ratio (O/F). The remaining figures depict compatibility and mixing efficiency at a detailed level by element type.

The effect of sample position in L/D, where D is the oxidizer orifice diameter or equivalent diameter is shown in Figure 5 for the area ratio one, mixture ratio four point elements. The overall characteristics of the elements are as expected, increasing E_m with increasing length. The swirl coaxial, premix pentad, and triplet are grouped together at high mixing efficiencies. The coaxial element has the lowest E_m of any element tested on this basis. The remaining elements group between the extremes of the shear coaxial and the swirl coaxial elements. When these elements are compared on a thrust/element basis, the same effects are noted (See Figure 7); i.e., the premix designs and the swirl coaxial element are high performing elements while the shear coaxial is a low performing element. With the exception of the swirl

coaxial element, the data trends are in the expected direction, reduced mixing with larger elements. The swirl coaxial element maximizes at 20 lb/element. It would appear that the fuel annulus size and radial oxidizer momentum are related. It is also interesting to note that the parallel sheet element mixes better than the like doublet elements over the thrust range tested in this program. In addition, the parallel sheet element at low (3 lbf [13 Newtons]) approaches the mixing efficiency of the best elements. For small thrust/element injectors (such as HIPERTHIN), these data indicate that the parallel sheet element is a viable element concept.

Area ratio influences for the basic element concepts are illustrated in Figure 8. Both shear mixing elements, the coaxial and increased shear element decrease in performance as area ratio is increased. It should be noted that the area ratio was varied by changing only the fuel geometry. The oxidizer diameter was held constant. The trends noted in Figure 8 are, therefore, not unexpected. Decreasing area ratio is in the direction of both smaller fuel annulus widths and higher velocity ratios--both effects which analytically are predicted to lead toward increased mixing efficiency. The swirl coaxial and premix designs are insensitive to area ratio influences, an effect that is somewhat surprising for the premix case. Cold flow testing by ALRC on an element design similar to the premix triplet design revealed that mixing efficiency was significantly impacted by orifice geometry changes. See Reference R for these data. Although the single-element injectors of both these series were similar, two important geometry differences are evident. The mixing cup length of this program was significantly longer than that of Reference 2. For this program, cup depths ranged from 1.15 to 4.75 L/D, where L is the cup depth and D is the oxidizer hole diameter. For the program of Reference 2, the ratio, on the same basis, was 0.1. The increased mixing cup depth forces mixing and therefore attenuates the effects of area ratio and mixture ratio variations. Also geometry was varied for rectangular fuel orifice shapes only, no I fuel channels were investigated on this program. Referring again to Figure 8, note that external impinging triplet data are very sensitive to area ratio influences,

Ref. 2 - Kors, D. L., Calhoon, D. F., Gaseous Oxygen/Gaseous Hydrogen Injector Element Modeling, AIAA Paper No. 71-674, June 14-18, 1971

optimizing at an A_f/A_o of 1.25. This element type, in general, is sensitive to most geometry and hydraulic variations.

The effect of mixture ratio on E_m is illustrated in Figure 9. Again, the swirl coaxial and premix designs are reasonably insensitive to this influence, while the shear coaxial element decreases in efficiency as a function of increasing mixture ratio. The remaining element types exhibit only a small parametric change.

Detailed parametric curves of the coaxial family of elements are illustrated in Figures 10 through 19. Included in this family are the shear, increased shear, and swirl coaxial elements. Figure 10 compares these elements on a length basis (L/D), where D is the oxidizer tube diameter. The effect of increased shear area and swirl is evident. These elements are compared on a mixture ratio basis in Figure 11, the swirl coaxial showing no influence and the shear and increased shear coaxial decreasing in efficiency with increasing mixture ratio. This effect is due to an increased V influence. The effects of area ratio (or fuel slot width) for these elements are illustrated in Figures 12, 13 and 14. In general, decreasing area ratio is in the direction of increased E_m for the three coaxial type elements. The swirl coaxial data in Figure 14 indicate an optimum in thrust size at 15 lbf/element (67 Newtons /element). This indicates that the radial component of momentum and the physical size are related or that there is a fuel momentum to oxidizer radial momentum ratio which produces optimum mixing. These effects are being investigated and will be reported in the next report period. The effect of swirl magnitude for various area ratio elements is illustrated in Figure 15. These data indicate that rather large changes in potential performance can be obtained with a rather moderate amount of oxidizer radial momentum.

II,C, Task IIB- Cold Flow Model Testing and Analysis (cont.)

The effect of lower propellant temperature on E_m is shown in Figure 16. With the exception of the swirler data, E_m increases with decreasing temperature. This trend is contrary to hot-fire data generated with ACPS size hardware, 1500 lbf on Contract NAS 3-14352. These data resulted in a significant reduction in performance when tested with cold propellants. The resulting conclusion is that the temperature influence noted in hot testing results from the combustion influence on the mixing/reaction processes.

The compatibility characteristics of the three elements are indicated in Figures 17 through 19. Here, the compatibility is defined as being proportional to the local mixture ratio measured at the edge of the flow field, (O/F)L nominalized by the overall integrated O/F $(O/F)_i$. The open symbols are the worst (most oxidizer-rich) O/F measured at the flow field boundary, the closed the best (most fuel-rich), and the half-open the average value. The resulting data band accounts for circumferential variation in the element flow field. Inspection of Figure 17, where the coaxial and swirl coaxial elements are compared on the above basis, reveals that in the near zone (close to the injector face) the coaxial element is benign as compared to the swirler. This effect was noted in combustion testing of full-scale hardware in Contract NAS 3-14354. In this testing with comparable chambers, the near zone heat flux using a swirler element was higher than the equivalent coaxial element. As a function of A_f/A_o, the coaxial element becomes more benign with increasing area ratio (see Figure 19). This fuel rich boundary is reflected in the low E_m data for this element, which was previously discussed. In general, those elements that exhibit high potential compatibility suffer from a low mixing rate.

An equivalent data set for the premix designs is illustrated in Figures 20 through 27. With the exception of length, these elements are relatively insensitive to design and operating variables. As discussed earlier, the fact that they are insensitive is somewhat surprising and can be attributed to mixing cup depths that attenuated the expected differences. The compatibility variations are not negligible as shown in Figures 25, 26 and 27.

Large differences in maximum and minimum local O/F indicate a streak potential. Note, for the premix triplet in Figure 26, that increasing the element width ratio tend to stratify the flow field. This can be explained by considering the geometry of the injector pattern. At a narrow fuel slot width, the available fuel momentum is concentrated on the center of the oxidizer stream, penetrating the bulk of the oxidizer and resulting in a homogenous flow field. As this penetration is reduced, the fuel, rather than penetrating the oxidizer stream, displaces it radially. The net effect is to form an edge condition that is alternately fuel and oxidizer rich at 90-degree intervals. The pentad element does not appear to be as sensitive because the available momentum of any one fuel stream is only half of the equivalent triplet. In no case does the pentad completely penetrate the oxidizer stream and, in general, always tends to displace rather than penetrate. The streaking characteristics of the $A_f/A_o = 1.0$ triplet element can be attenuated by reducing the fuel momentum. This is illustrated in Figure 27, where the observed streak characteristic was modified by reduced momentum as the fuel orifice area was increased at a constant mixture ratio.

Data similar to those presented earlier for the premix and shear designs are found for the like doublet element in Figures 28 through 32. Particular attention should be directed at Figures 28, 29 and 30, where the element spacing effects are parametrically illustrated. These data indicate that an optimum is found at a fuel to oxidizer spacing of 0.1 in. (0.254 cm). Element spacing lower than the optimum have lower mixing efficiency because, when the elements are close together, the primary fans interact strongly forming secondary fans. These fans are nonhomogenous in nature with fuel on one side of the fan and oxidizer on the other. When the doublet spacing is larger than the optimum value, mixing is inhibited simply because the elements are too far apart. Compatibility of this element, as shown in Figure 32 was not good since large circumferential variations in O/F or streaks were measured.

Data for the parallel sheet elements are found in Figures 33 through 37. As a function of length, thrust/element, and propellant temperature, the data appear to be well behaved and show the expected trends. As a function of O/F, the data increase in mixing efficiency, contrary to the trend of the similar coaxial element. Compatibility effects are as expected: wide O/F variations with $(O/F)_L$ depending on which side the element is probed.

The external impinging F-O-F triplet data are depicted in Figures 38 through 41. In general, this element configuration is very sensitive to all operating and geometry variables. Refer to Figure 38 where mixing efficiencies for various impingement angles and area ratios as a function of thrust/element are depicted. At the 15 lbf level, the extreme sensitivity of mixing efficiency with impingement angle is noted. One also notes that area ratio influences are optimized in the 1.0 to 1.25 A_f/A_o range. These data are cross plotted in Figures 39 and 40. Referring to Figure 39, one notes that the $A_f/A_o = 0.96$ mixing efficiency increases dramatically with impingement angle. Inspection of the detailed flow field reveals that, as the radial momentum component is increased by increasing the impingement angle, increased penetration of the axial oxidizer jet occurs, thus yielding a more homogenous flow field. However for the area ratio = 0.50 data, a contrary trend is noted. In this case, overpenetration is achieved and increasing the impingement angle only amplifies the excess penetration of the fuel. Mixing was also determined to be a strong function of mixture ratio coupled with impingement angle. On the fuel-rich side of the optimum, overpenetration occurred; on the oxidizer-rich side, underpenetration occurred (See Figure 41). In general, the compatibility of this element is expected to be poor. Figure 42 indicates the degree and magnitude of the potential compatibility problem for the overpenetrated oxidizer jet. The entire flow field boundary is oxidizer rich and varies widely in the circumferential direction.

II, C, Task IIB - Cold Flow Model Testing and Analysis (cont.)

c. Mathematical Cold Flow Model Analysis

Approximate first order mathematical models are being developed to describe the fundamental mixing processes for the various basic element types. The solutions from these mathematical models can then be used to correlate the interdependent effects of primary design parameters and operating conditions on the various element mixing efficiencies and element compatibility characteristics. Approximate models have been completed for the shear coaxial element, like doublet element, and parallel sheet element. These models are able to predict the following experimental cold flow effects:

(1) The effect of progressively increasing axial displacement (L' or L/D) on maximum measured dynamic head and maximum deviation from equilibrium specie concentration on the element centerline.

(2) The effect of injector O/F variation.

(3) The effect of fuel to oxidizer orifice area ratio, A_f/A_o.

(4) The effect of fuel to oxidizer injection dynamic head ($\Delta P_f/\Delta P_o$) ratio.

(5) Effect of varying element size, F/E.

(6) Effect of propellant temperature, T_P.

(7) Effect of impingement angle, θ.

(1) Physical Basis for Mathematical Model Formulation

The cold flow tests were conducted with three distinct gaseous species. The fuel element flows actual H_2. The oxidizer element uses N_2 to simulate O_2. A helium bleed flow is superimposed atop the two active propellants above to suppress element recirculation. A state of perfectly uniform mixing (E_m = 1.00) can be defined by a gas mixture distribution in which all three gas species are in equilibrium in a fixed relative proportion

(constant O/F) at all points. This is the equilibrium mole fraction that each gas specie must asymptotically approach in an infinite length chamber. At the exit of the fuel and oxidizer element orifices, the initial composition must be 100% mole fraction of H_2 and N_2, respectively. At the element exit, $E_m = 0$ (by definition).

In the first approximation, the rate of change of E_m from 0 to 100% is determined by the mathematical mixing model. Early in the cold flow data analysis effort, it was noted that the empirical rate of change of species mole fraction from its 100% pure initial value to its asymptotic equilibrium value was directly proportional to the rate of change in local element dynamic head, starting from its initial injection value to its asymptotic uniform negligible value. The above merely proved that the empirical mass transfer rate was found to be directly proportional to the momentum transfer rate. The latter was calculated analytically by assuming initial potential flow characteristics at the element exit and using classical simplified boundary layer solutions to calculate the downstream momentum transfer (dynamic head dissipation) rate. Therefore, it is reasonable to assume that, if the analytical model can predict the rate of change of element dynamic head and species composition which is empirically measured, the significant parameters in the analytical solution can likewise correlate the empirical rate of change in the mixing distribution.

All of the elements tested on this program utilize sharp edge inlet orifices to minimize fabrication cost. Since all elements tested fit into a single injector/chamber fixture, they all have nearly constant orifice length. Therefore, the variation in F/E tested results in widely varying element L/D. Thus, as a preliminary step to the mathematical model formulation, it was necessary to conduct an element hydraulic analysis to define the actual

flow characteristics. The automated DATNAL computer program utilized the geometric orifice area and assumed that both fuel and oxidizer discharge coefficients, C_{D_f} and C_{D_o} = 1.00. This was done for expedience since the data reduction and DATNAL analyses had to be performed prior to the empirical data correlation and C_D's were not available at that time.

The element C_D is calculated theoretically based upon the physical contraction coefficient at the vena contracta (C_{co}), orifice Reynolds number, and orifice L/D using the mathematical hydraulic model developed in Reference R and using the method eluded to in Reference R. These values of C_D are then used to define an average effective element injection velocity which is related to the injection velocity originally calculated on the DATNAL program by the equation below.

$$V_{i,\text{effective}} = V_{i_J} = \frac{V_{i,\text{DATNAL}}}{C_{D_i}} \tag{1}$$

Strictly speaking, the actual injection velocity on the element centerline is inversely proportional to the physical contraction coefficient at the vena contracta (C_{coi}), resulting in a higher local velocity than that calculated by Equation (1). Elsewhere, the local injection velocity is less than V_{i_J}, but to consider the detail injection velocity and mass profile with boundary layer effects results in an unnecessarily complex mathematical solution without significantly enhancing the overall results. Therefore, using the effective C_D squares off the actual injection velocity profile, permitting it to be replaced by an equivalent potential flow jet at the injector face. By definition, the injection dynamic head is calculated as follows:

$$P_{Do_i} = 1/2\ \rho_i\ V_{i_J}^2 \tag{2}$$

For simple cylindrical orifices drilled in a flat plate with moderate L/D, the theoretically calculated injection dynamic head is in close agreement with the empirical injection ΔP measured from the injection manifold pressure to P_c. This verifies the accuracy of the predicted hydraulic analyses. However, long L/D elements, swirler coaxial elements, internal premix triplet and pentad elements, and other special cases must have their experimental injection ΔP's reduced by the pressure losses attributed to friction, internal expansion, and turbulent dissipation to provide an accurate measure of corrected injection dynamic head at the injector face.

The element hydraulic analysis results were used to define the injection velocity, injection dynamic head, and effective element area at the initial starting point at the element exit. Downstream from the injector face boundary layer, growth rates were calculated to predict the rate of change of local dynamic head and species composition. These mathematically predicted trends were then plotted and compared with the empirical data to verify the significance of the primary design and operating parameters.

(2) Mathematical Mixing Models for Various Element Types

First order analytical approximations have been completed for the various shear and viscous mixing elements. A brief summary of their mathematical development is described in the following subsections.

(a) Shear Coaxial Element

The shear coaxial element is mathematically characterized by a circular jet of effective diameter $C_{D_o}^{1/2} \cdot D_o$ with a concentric annular fuel orifice surrounding it. The effective fuel annulus width is $t_f = 1/2\ C_{D_f}\ (D_{f2} - D_{f1})$. The fuel hydraulic diameter is calculated using the standard relationship,

$$D_{H_f} = \frac{4\left[\frac{\pi}{4}\left(D_{f2}^2 - D_{f1}^2\right)\right]}{\pi\left(D_{f2} + D_{f1}\right)} = \left(D_{f2} - D_{f1}\right) \tag{3}$$

where: D_{f2} = outer fuel annulus diameter
D_{f1} = inner fuel annulus diameter

The diameter-based Reynolds number is calculated for both fuel and oxidizer elements using the hydraulic diameter.

$$Re_{D_i} = \frac{\rho_i \, V_{i_J} \, D_i}{\mu_i} \tag{4}$$

The Reynolds number for gas/gas propellants is on the order of 10^5 so that the turbulent flat plate boundary layer solution is transformed to the form

$$\frac{\delta_o}{R_o} = \frac{0.75\ (L/D_o)^{0.8}}{Re_{D_o}^{0.2}} \tag{5}$$

and

$$\frac{\delta_f}{t_f} = \frac{0.75\ (L/D_{H_f})^{0.8}}{Re_{D_{H_f}}^{0.2}} \tag{6}$$

where: δ = velocity boundary layer thickness
R_o = oxidizer radius (1/2 D_o)
t_f = fuel annulus width, 1/2 $(D_{f2} - D_{f1})$

Equations (5) and (6) above can evaluate the relative velocity boundary layer thickness as a function of the axial distance from the injector face, L.

To be exact, the injection velocity profile has to be integrated to simultaneously satisfy the momentum and continuity equations in the manner described in Reference R. However, for mathematical simplicity, the assumption can be made that the initial potential flow diameter is reduced radially inward at the same rate that the boundary layer grows radially outward. Then a reduced oxidizer potential flow boundary coefficient, C_b, can be defined by

$$C_b = (\sqrt{C_{D_o}} - \delta_o/R_o)^2 \tag{7}$$

Similarly, an increased oxidizer boundary layer contraction coefficient, C_c, can be defined by

$$C_c = (\sqrt{C_{D_o}} + \delta_o/R_o)^2 \tag{8}$$

Next, it is approximated that the local oxidizer velocity profile in the boundary layer varies linearly from V_{o_J} at C_b to zero velocity at C_c as shown schematically in Figure 43. The momentum transfer (dynamic head dissipation) rate can now be calculated by integrating the dynamic head throughout the local velocity profile.

$$P_D(L) = \frac{1}{C_c \pi R_o^2} \left\{ \int_o^{R_o\sqrt{C_b}} (1/2\ \rho_o\ V_{o_J}^2)\ 2\pi r dr \right.$$

$$\left. + \int_{R_o\sqrt{C_b}}^{R_o\sqrt{C_c}} 1/2\ \rho_o \left[V_{o_J} \left[1 - \left(\frac{r/R_o - \sqrt{C_b}}{\sqrt{C_c} - \sqrt{C_b}} \right) \right] \right]^2 2\pi r dr \right\}$$

which integrates to

$$P_D(L) = (1/2\ \rho_o\ V_{o_J}^2)\left[\frac{C_b}{C_c} + \frac{3C_c - C_b - 2\frac{C_b^2}{C_c} - 4/3\left[1 - \left(\frac{C_b}{C_c}\right)^{3/2}\right]}{\left[\sqrt{C_c} - \sqrt{C_b}\right]^2}\right]$$

Using the definition of injection dynamic head from Equation (2), the local to initial dynamic head ratio is

$$\frac{P_D(L)}{P_{D_o}} = \frac{C_b}{C_c} + \frac{3C_c - C_b - 2\frac{C_b^2}{C_c} - 4/3\left[1 - \left(\frac{C_b}{C_c}\right)^{3/2}\right]}{\left[\sqrt{C_c} - \sqrt{C_b}\right]^2} \qquad (9)$$

Once the dynamic head ratio is mathematically accounted for, the local oxidizer composition can be calculated from

$$X_o(L) = X_{o,eq} + \frac{P_D(L)}{P_{D_o}}(1.000 - X_{o,eq}) \qquad (10)$$

where: $X_o(L)$ = local mole fraction of oxidizer propellant

$X_{o,eq}$ = equilibrium mole fraction of oxidizer propellant based on overall O/F and helium flow rate

To make the mathematical solution computationally tractable for manual calculation, it was discovered that the initial dynamic head decay could be adequately approximated by neglecting the contribution to the total dynamic head in the boundary layer. This is mathematically handled by neglecting the second term in the right-hand member of Equation (9) and simplifying it to

$$\frac{P_D(L)}{P_{D_o}} \simeq \frac{C_b}{C_c} = \frac{\left[\sqrt{C_{D_o}} - \delta_o/R_o\right]^2}{\left[\sqrt{C_{D_o}} + \delta_o/R_o\right]^2} \qquad (11)$$

The analytically predicted local dynamic head using the approximation of Equation (11) is plotted on Figure 44 vs L/D for the 67 Newton (15 lbf) shear coaxial element. The experimental oxidizer dynamic head measured on the element axis using probe number 6 is shown for comparison. Figure 44 shows that, in spite of the many gross mathematical approximations which were made, the calculated dynamic head decay rate based on a viscous boundary layer mechanism closely approximates the experimental trend.

Likewise, the maximum measured oxidizer mole fraction on the coaxial element axis is plotted on Figure 45 vs the analytically predicted local composition using Equations (10) and (11). Again, the mathematically predicted N_2 composition profile provides an adequate first order approximation to the measured local compositions.

The mathematical treatment of the annular fuel dynamic head dissipation rate is conceptually similar using the boundary layer solutions except for differences in the boundary conditions which are dictated by the fuel orifice geometry. First of all, Equation (6) shows that the fuel hydraulic diameter is used in the Reynolds number and L/D terms in the right member but the geometric annulus dimension is used for the denominator in the left member. A second difference is that the fuel viscous drag dissipates itself in two directions: radially inward toward the oxidizer and radially outward toward the chamber wall. Furthermore, since t_f is generally much less than $1/2\ D_f$, the boundary layer expansion occurs two-dimensionally for the fuel rather than radially as for the circular oxidizer element. Therefore, the annular fuel boundary coefficient and contraction coefficients comparable to Equations (7) and (8) must be redefined as follows:

$$C_b = C_{D_f} - 2(\delta_f/t_f) \quad (12)$$

$$C_c = C_{D_f} + 2(\delta_f/t_f) \quad (13)$$

The dynamic head associated with the two-dimensional annular fuel velocity profile described by Equations (12) and (13) was numerically integrated. The solution is shown on Figure 46. Because the fuel element potential flow width is narrow in comparison to the oxidizer, $1/2\ C_{D_f}\ (D_{f2} - D_{f1}) << \sqrt{C_{D_o}} \times D_o$, and because the fuel drag occurs on two surfaces instead of one, a numerical comparison of Equation (12) with Equation (7) shows that the fuel potential core is dissipated in much shorter axial distances from the injector face than the oxidizer. At axial distances greater than the critical length when fuel $C_b = 0$, Figure 47 characterizes the local to initial fuel dynamic head ratio. The calculated fuel dynamic head profile is also shown on Figure 44. It is obvious that the calculated fuel dynamic head dissipation rate occurs considerably faster than for the oxidizer. The experimental dynamic pressure downstream of the fuel annulus was not available for direct comparison with the analysis. This is because the midpoint of the fuel annulus occurs on a 0.092-in. radius and the nearest experimental probes are on a 0.125-in. radius. Near the injector face where the gradients are steep, the 0.033-in. radial mismatch is significant in comparison with the fuel annulus dimension (t_f = 0.028 in.). Nevertheless, for lack of better data, the eight probes on the 0.125-in. radius were averaged as a measured lower limit of the fuel dynamic head.

Likewise, the calculated fuel mole fraction profile is plotted on Figure 45, and the 0.125-in. radius probe measured compositions were averaged and plotted with the full realization that the actual maximum fuel mole fraction might be somewhat higher than shown.

It should be remembered that, near the injector face, the radial dynamic head gradient and species gradient are very steep. A deviation as small as one probe diameter from perfect concentricity between the element centerline and the probe measurement position could significantly influence the measured data. Thus, it is probable that the real (undetected) data may actually be in better agreement with the analytical prediction than the experimentally measured data shown in Figures 44 and 45. Therefore, it can be concluded that the viscous boundary layer solutions provide an acceptable theoretical model of the shear coaxial mixing rate as a function of length.

Another operating parameter which was analytically evaluated was the influence of O/F on the mixing rate for a constant injection element geometry and fixed L/D. The 67 Newton (15 lbf) shear coaxial element was evaluated at L/D = 7 for O/F = 2.0, 4.0, and 6.5. At low O/F, the fuel to oxidizer injection dynamic head ratio increases and, at high O/F, it decreases. The previously developed shear coaxial model was applied to the mixture ratio survey tests. It was found that the measured fuel and oxidizer dynamic head variation with O/F variation was reasonably approximated. The fuel and oxidizer mole fractions predicted by Equation (10), however, were significantly in error. At low O/F, the oxidizer mole fraction was overpredicted and the fuel mole fraction was underpredicted. The opposite occurred at high O/F. After considerable thought, the following explanation was conceived.

Throughout the above model development, the fuel and oxidizer elements were treated independently as if each were acting alone. Then the solutions were superimposed to infer overall mixing influences. In reality, the two solutions must be coupled and the interaction of one must be considered on the other. Equation (10) is only valid upstream of the point where the oxidizer and fuel boundary layers initially come into contact. Downstream of this point, the two jets combine to act as one. The contribution of

each to the resultant jet must be proportional to their respective mole fractions since mixing occurs on a molecular basis. Since the rapid mixing zone near the injector face is controlled by Newton's equations of motion, the primary normalizing parameter must be the injection dynamic head since this provides the mixing potential. Therefore, define an equivalent injection dynamic head, P_{DE}, which is the overall result of the separate fuel and oxidizer contributions.

$$P_{DE} = \frac{\frac{\dot{w}_o}{MW_o} \times P_{D_o} + \frac{\dot{w}_f}{MW_f} \times P_{DF}}{\frac{\dot{w}_o}{MW_o} + \frac{\dot{w}_f}{MW_f}}$$

The above relationship can be simplified to

$$P_{DE} = \frac{P_{D_o} + \frac{MW_o/MW_f}{O/F} \times P_{D_f}}{1 + \frac{MW_o/MW_f}{O/F}} \qquad (14)$$

After a combination of analytical considerations, plus empirical trial and error, it was determined that the fuel and oxidizer compositions could best be correlated by the following equation:

$$X_i(L) = X_{i,eq} + \left(\frac{P_D(L)}{P_{D_{o,i}}}\right)\left(\frac{P_{D_{o,i}}}{P_{DE}}\right)(1.000 - X_{i,eq}) \qquad (15)$$

The reason that the O/F = 4 data shown on Figure 45 did not require the equivalent dynamic head ratio term is because the oxidizer and fuel injection dynamic heads were 6.3 and 6.8 psi, respectively. Using Equation (14), P_{DE} = 6.7 psia and the factor is close to unity for both the oxidizer and fuel compositions and was not missed.

The problem with the shear coaxial element is that the fuel jet is diffused much faster and approaches the equilibrium fuel composition at a much faster rate than the oxidizer. This always results in an oxidizer-rich core region which is the greatest obstacle to achieving high E_m. Therefore, to achieve high mixing efficiency, the analytical model dictates the necessity of accelerating the oxidizer diffusion rate and retarding the fuel dispersion rate. The analytical model predicts that this can only be done by reducing the oxidizer injection dynamic head and increasing the fuel injection dynamic head as required by Equation (15). In practice, this is achieved by either operating at low O/F or decreasing A_f/A_o. The experimental data shown on Figures 8 and 11 confirm both analytical predictions.

Since the mass diffusion rate can be analytically described by viscous boundary layer solutions, all element design parameters and operating conditions are either automatically accounted for or implied in such parameters as the Reynolds number, L/D, propellant density, viscosity and molecular weight, pressure, temperature, orifice geometry, weight flow rate, mixture ratio, injection dynamic heads, injection velocity, etc.

It has been adequately demonstrated that, when the test design parameters and operating conditions are properly described in the mathematical model, the model will quantitatively predict the experimentally measured mixing efficiency trends. Therefore, it stands to reason that, if any single design parameter or single variation in operating condition is parametrically analyzed by the mathematical model while holding all other parameters constant, the model must be able to predict the trend which can be expected by the real world variation on the element mixing characteristics.

The one-to-one correspondence between analytically predicted mixing profiles and the experimental cold flow mixing data as shown in Figure 48 demonstrates the practical utility of developing an

approximate mathematical mixing model to correlate and better understand the experimental data. Much higher confidence can be placed in correlations which have a logical theoretical basis because the model can be used to evaluate subtle second and third order effects on the design extrapolation which would otherwise be neglected if based only on empirical first order correlations.

(b) Like-on-Like Doublet Element

The like-on-like doublet element incorporates both impingement and shear principles. The impingement momentum is mathematically characterized to describe a gaseous potential flow spray fan similar to a conventional liquid propellant spray fan. Viscous boundary layer effects are assumed to occur on the spray fan surfaces and the two solutions are coupled.

A like doublet is mathematically characterized by equal stream diameters, equal density, equal injection velocity and momentum from the opposing orifices. Thus, the spray fan is symmetrical. If the resultant spray fan is initially analyzed as a bounded potential core, the spray fan propagation angle normal to the impingement plane can be mathematically shown to be

$$\alpha = \sin^{-1} (\tan \theta) \tag{16}$$

where: α = spray fan half angle

θ = impinging doublet half angle ($\theta \leq \pi/4$ radian)

From continuity considerations, the potential core local spray fan thickness can be shown to be

$$\frac{t_f}{D} = \frac{\pi C_D}{4 \, (L/D) \cos \theta \tan \alpha} \tag{17}$$

where: t_f = potential flow spray fan thickness

The width of the spray fan is 2L tan α.

The potential spray fan surfaces are acted upon by viscous forces. The flat plate turbulent boundary layer solution shows that

$$\delta = \frac{0.375\ L}{(L/D)^{0.2}\ Re_D^{0.2}} \tag{18}$$

The viscous effects on the narrow edges of the spray fan can be neglected. However, there is a critical L/D at which the velocity boundary layers acting from both of the flat surfaces on the spray fan become equal to the potential flow spray fan thickness. Equating Equation (17) to twice Equation (18), the critical L/D is

$$\frac{L_{crit}}{D} = \frac{\pi C_D\ Re_D^{0.2}}{3\ \cos\ \theta\ \tan\ \alpha} \tag{19}$$

$$t_{f,min} = \frac{\pi C_D \cdot D}{4\ (L_{crit}/D)\ \cos\ \theta\ \tan\ \alpha}$$

or

$$t_{f,min} = \frac{3D}{4\ Re_D^{0.2}} \tag{20}$$

$$\text{Max spray fan width} = 2L_{crit}\ \tan\ \alpha$$

Equation (19) shows that increasing the orifice C_D or Reynolds number will increase the critical L/D, whereas increasing the doublet impingement half angle decreases it. Equation (20) shows that the

minimum equivalent potential spray fan thickness is directly proportional to the orifice diameter (implies F/E and injection dynamic head influence) and inversely proportional to the one-fifth power of Reynolds number. The physical significance of the minimum potential spray fan thickness is as follows. When the viscous boundary layer effects propagate all the way through the potential fan, the normal impingement component of the doublet injection momentum which was assumed to cause the fan spreading rate has been largely dissipated. Therefore, beyond L_{crit} the potential core is assumed to be limited to a pure axial displacement. The experimental test data support this simplified asymptotic mathematical approximation.

Compare calculated δ from Equation (18) with potential thickness, t_f, defined by Equation (17) if $L < L_{crit}$. In that case,

$$\frac{C_b}{C_D} = 1 - 2\ (\delta/t_f) \tag{22}$$

$$\frac{C_c}{C_D} = 1 + 2\ (\delta/t_f) \tag{23}$$

Use Equation (22) with Figure 46 to predict P_D/P_{D_o}.

If $L > L_{crit}$, use 2δ from Equation (18) and $t_{f,min}$ from Equation (20) in conjunction with Figure 47 to predict P_D/P_{D_o}. In either case, the calculated P_D/P_{D_o} ratio can be used with Equation (15) to predict the axial mole fraction profile.

The above like doublet model explains the empirically observed effect of axial length variation shown in Figure 49. It also predicts the observed trends for O/F survey, A_f/A_o variation, and F/E variation.

The only test variation which has not yet been adequately characterized by the mathematical model has been the effect of variable spacing between doublet pairs. It is suspected that doublet spacing affects the fuel/oxidizer fan interaction and the actual secondary impingement fan deformation and distortion in the real world has not yet been characterized mathematically. However, the empirical data show this is probably a second order effect (see Figure 29) and its accurate model development has been deferred due to lack of funds.

(c) Parallel Sheet Element

The parallel sheet element was evaluated for potential HIPERTHIN injector applications. An actual HIPERTHIN element was not cold flow tested for two reasons. Its manufacturing cost is higher on a small scale test element because of the relatively extensive fabrication setup in comparison to a single interchangeable machined orifice plate for the other elements tested. The second reason is that, because of its normally small element size, the cold flow distribution would have to be tested much closer to the injector face to be realistic. If this were done, a completely new set of instrumentation would have been required to sample the data. The parallel sheet element was tested at F/E = 222 Newtons (50 lbf) and 13 Newtons (3 lbf). This was done for ease of testing with the expectation that the results could be extrapolated down to a HIPERTHIN scale.

Mathematically speaking, the parallel sheet element should be the simplest element to model based on viscous boundary layer growth rates. However, the theoretical hydraulic analysis revealed that, because of the 60° contracting mitre bend in the fuel orifice plate, the resulting fuel stream was canted 0.57 radian (33°) and 0.37 radian (21°) toward the axial oxidizer jet in the high and low thrust elements, respectively. The experimental cold flow

distribution data confirm that the fuel was indeed canted by some unknown angle toward the oxidizer. Furthermore, because the oxidizer manifold inlet diameter was smaller than the high thrust parallel sheet oxidizer element widest dimension, the oxidizer jet only effectively filled approximately one-half the geometric oxidizer width. The local species distribution data, local dynamic head data, and overall oxidizer element ΔP data conclusively confirmed this effect. Therefore, although the geometric A_f/A_o ratio was unity, the actual ratio was closer to two because of halving C_{D_o}. Another factor to consider is that, in actual practice, a HIPERTHIN injector would have a multitude of adjacent elements surrounding and interacting with it. The tested single cold flow element only had an opposite propellant on one side, leaving the other side unconstrained to diffusion. The results of the above deviations from ideal parallel sheet design were included in the mathematical model formulation.

Based on the calculated hydraulic behavior of the parallel sheet elements as actually tested, its descriptive model is a combination of partial parallel sheet and partial unlike impinging doublet characteristics. The canted fuel stream caused the formation of a weakly divergent spray fan and, consequently, some fan spreading and potential spray fan thinning with increasing L. The like doublet equations derived in Section II,C,3,c,(2)(b) can be modified to describe unlike doublet characteristics if θ, the effective impingement half angle, is taken to be the effective angle between the initial injected angle and the resultant hydraulic momentum angle, and the problem is treated like a mirror image for the oxidizer and fuel relative to itself. Otherwise, the basic concept of the mathematical model equations previously described for the shear coaxial and like-on-like doublet elements were used to describe the parallel sheet elements.

II, C, Task IIB - Cold Flow Model Testing and Analysis (cont.)

Variations in axial length, O/F, F/E, and propellant temperature were mathematically evaluated. Initially, there was some deviation noticed between measured and predicted rates of change in the species mole fractions. After a period of analytical reasoning and pondering over the physical situation, the following modification was evaluated in the predicted species mole fraction equation.

$$X_i(L) = X_{i,eq} + \left(\frac{P_D(L)}{P_{D_o}}\right)\left(\frac{P_{D_i}}{P_{DE}}\right)^f (1.000 - X_{i,eq}) \qquad (24)$$

In going from Equation (10) to Equation (15), the addition of the (P_{D_i}/P_{DE}) ratio was empirically justified on the basis that it accounted for interpropellant interactions. In going further from Equation (15) to Equation (24), the interaction term was raised to the exponent f. The term f is the ratio of the common fuel-oxidizer wetted perimeter available for interpropellant interaction divided by the total fuel or oxidizer wetted perimeter available for diffusion and shear mixing. For example, in the low F/E parallel sheet element, the fuel and oxidizer elements were at equal width. Neglecting end effects on the 10:1 aspect ratio slot, both the oxidizer and fuel f exponents were set equal to 0.5 since only half (side facing each other) of their total perimeter is available for interaction. In the high thrust parallel sheet element, the oxidizer f is equal to 0.5 because of the side facing the fuel. The fuel f parameter, however, is only equal to 0.25 because only the center half of the side facing the oxidizer element is interacting due to the hydraulic inlet restricted oxidizer element width. When Equation (24) was applied to all the parallel sheet element mathematical models, consistency between measured and predicted mole fractions was considerably improved. With this change, the model was able to successfully predict the empirical effects of L, O/F, F/E, and T_p variations.

These parallel sheet elements illustrate a special situation in which the quality of the pure analysis would probably be better than the quality of the experimental data. If the mathematical model were used to evaluate nonimpinging element characteristics in which both the fuel and oxidizer gas jets were truly parallel and the multiple element interactions were considered with purely viscous drag induced diffusion mechanisms, the mathematically predicted mixing efficiency would probably be more accurate than the present experimental single-element cold flow data.

In retrospect, the nominal O/F shear coaxial model should have been described by Equation (24) instead of Equation (10). The effect of (P_{D_i}/P_{DE}) was not missed because both oxidizer and fuel injection dynamic heads were approximately equal and the ratio was close to unity. In the shear coaxial O/F variation model, the oxidizer f exponent was coincidentally set equal to unity as it should have been because the oxidizer element is completely surrounded by the fuel annulus. In hindsight, the fuel f exponent should have been set approximately equal to 0.5 instead of 1.0 because the interaction only occurs on the inside surface of the fuel annulus. This error in the fuel exponent was not recognized because the 14/(O/F) term in the equivalent injection dynamic head parameter (see Equation (14)) heavily weights P_{DE} toward the fuel side. Consequently, the (P_{D_f}/P_{DE}) ratio is close to unity and the error in the exponent was not detected at that time. In the like doublet model, both fuel and oxidizer f exponents were again set equal to 1.0. This may have been an adequate approximation because the fuel to oxidizer doublet spacing (which was experimentally varied) was small in comparison to the total spray fan width. Finally, it took the parallel sheet data to refine Equation (24) to its present status. There are probably additional modifications to Equation (24) which are required to further improve its accuracy in describing special element types.

The above mixing model progression graphically illustrates an intriguing dilemma. That is, an exact mathematical model which rigorously and simultaneously accounts for all physical considerations becomes cumbersome, unwieldy, and finally totally intractable mathematically. On the other hand, an approximate mathematical model such as was derived above can be relatively straightforward, easily hand calculated, and sheds considerable valuable physical insight into the process being investigated with a relatively modest expenditure of time and funding. However, it must be realized that this method too has its limitation. Its limitation is that, because it is an approximate model, exact correlation between analytical prediction and measured data cannot always be expected. Therefore, if only minor deviations occur between prediction and data because of neglected second order effects or because of coincidental test conditions, these errors must be attributed to either the analytical or measurement "noise level" without being aware of the analytical shortcomings within the approximate model. Therefore, the only way that the accuracy of the approximate model can be further improved is to encounter significant and recognizable errors between analysis and data. In other words, successful predictions cannot further improve model accuracy; only through failure can there be a possibility for further refinement. The necessary failure can only be achieved by experience. This means that, ideally, every Task IIB cold flow condition which was experimentally tested should be analytically modeled. Unfortunately, this is beyond the scope of the current program.

In spite of the limitations in the approach taken by the approximate mathematical model tempered by empirical data and experience, this method provides the maximum return for the time and money spent. A conceptually similar approach marrying theoretical/approximate mathematical analysis and experimental data has been proven by ALRC in its success liquid propellant injector hydraulic, atomization, and vaporization dependent energy release model developments.

II,C, Task IIB - Cold Flow Model Testing and Analysis (cont.)

(d) Other Element Mixing Models

The approximate mathematical model development effort is currently in progress for the conventional external impinging F-O-F triplet element family.

The swirler coaxial and increased shear coaxial element model description requirement is conceptually understood but has not yet been performed. Although no significant analytical difficulties are anticipated, only peripheral evaluations are presently scoped for these elements.

No analytical effort has yet been made to describe internal premix triplet and pentad elements. The conceptual premixing mechanism is understood based on a scrutiny of the experimental cold flow data. The required initial approach to the mathematical model description has been identified.

d. Hot Flow Testing

It has been ALRC's belief that cold flow testing alone could not completely describe the mixing process. Combustion does impact the mixing profiles generated in cold flow testing. In Reference 2, this impact was described both analytically and empirically for a conventional shear coaxial element. In general, the combustion adversely biased the mixture ratio profiles; i.e., mixing profiles measured in cold flow were displaced axially by combustion. As part of this program, the effects of combustion were studied for a high mixing efficiency element, the swirl element.

II, C, Task IIB - Cold Flow Model Testing and Analysis (cont.)

A hot flow test series was conducted with the objective of determining whether combustion influenced the profiles of a swirl coaxial element. The experimental program measured the mixture ratio distribution of both hot and cold flow gas flow fields generated with identical hardware and flow conditions. The only difference between these tests was that, in one case, the H_2-O_2 propellants were burning and, in the other case, they were not. The hot flow hardware was, in fact, the hardware of the cold flow program.

This testing was conducted in the steam-cooled chamber and utilized a double-walled, hot H_2 cooled probe* to withdraw the gas sample. The sample was routed into the mass spectrometer via copper steam-heated tubing. The resulting data conclusively indicated a combustion mixture ratio profile substantially different than the cold flow profile. These data are presented in Figure 50 as a function of the probe radial and axial distance. This figure indicates that the cold flow mixture ratio gradients had essentially dissipated at the first axial position, indicative of the desirable mixing qualities of the swirl coaxial element. Comparing the hot flow profiles with the cold flow profiles at the same length, it is apparent that the mixture ratio profiles are steeper (greater deviations from uniformity) and persist to 7.17 in. (18.25 m) These data substantiate that the combustion does adversely affect the mixing. These data are plotted in a different format in Figure 51; they indicate that three mixing zones are possible:

(1) The near zone where copious mass transfer takes place and combustion is initiated.

(2) An intermediate zone where the large density changes of combustion products displace the oxidizer inward and the fuel outward.

(3) A region where the continued rotation of the oxidizer-rich core promotes radial diffusion of the oxidizer-rich products into the fuel-rich mantle.

*Particular care must be taken in this type of testing to ensure that the combustion products (H_2O) do not condense anywhere in the system. Thus, all components were heated to over 250°F during testing using either steam or heated hydrogen.

D. TASK IIIA - SINGLE-ELEMENT HOT FIRING DESIGN AND FABRICATION

The single-element hot firing stand is complete and the hot fire hardware is being installed. The hot fire chambers have been designed and fabricated. Three 50-lbf-thrust chambers were built and are shown in Figure 52. Two chambers are 2.0 in. long with a 2.5 and 3.5 contraction ratio. The third chamber is 5.5 in. long with a 2.5 contraction ratio. All the chambers have a area ratio, $A_e/A_t = 1.75$. They will be heat sink in type and are designed to have a 2-sec duration while maintaining adequate thermal response. Twelve thermocouples are buried at approximately midwall depth. The thermocouples are located 0.5-in. apart axially and in three rows, 45° apart circumferentially. Provisions are made for a spark type igniter to be located in the chamber wall. The two P_c taps are located near the injector face and at the entrance to the convergent section of the nozzle.

The three injectors to be tested are the 0.5 A_f/A_o swirl coaxial, 0.5 A_f/A_o coaxial, and the 33% premix triplet. This hardware is currently being modified from the cold flow hardware and will be manufactured and tested during the next reporting period.

III. CURRENT PROBLEMS

No technical problems are evident at this time. The program has slipped approximately one and a half months. It is anticipated that some portion of this time can be recovered in the hot fire testing.

IV. WORK PLANNED

The remaining single-element cold flow data will be analyzed in the next report period. The hot fire single-element injectors will be tested and the data analysis will be initiated.

V. CONSUMABLES

The table below lists the consumption to date of propellants and gases together with the anticipated usage during the following month:

	Consumed to Date	Predicted for Next Month
H_2	5946 lbs	200 lbs
He	1926 lbs	0 lbs
N_2	13.1 tons	7 tons

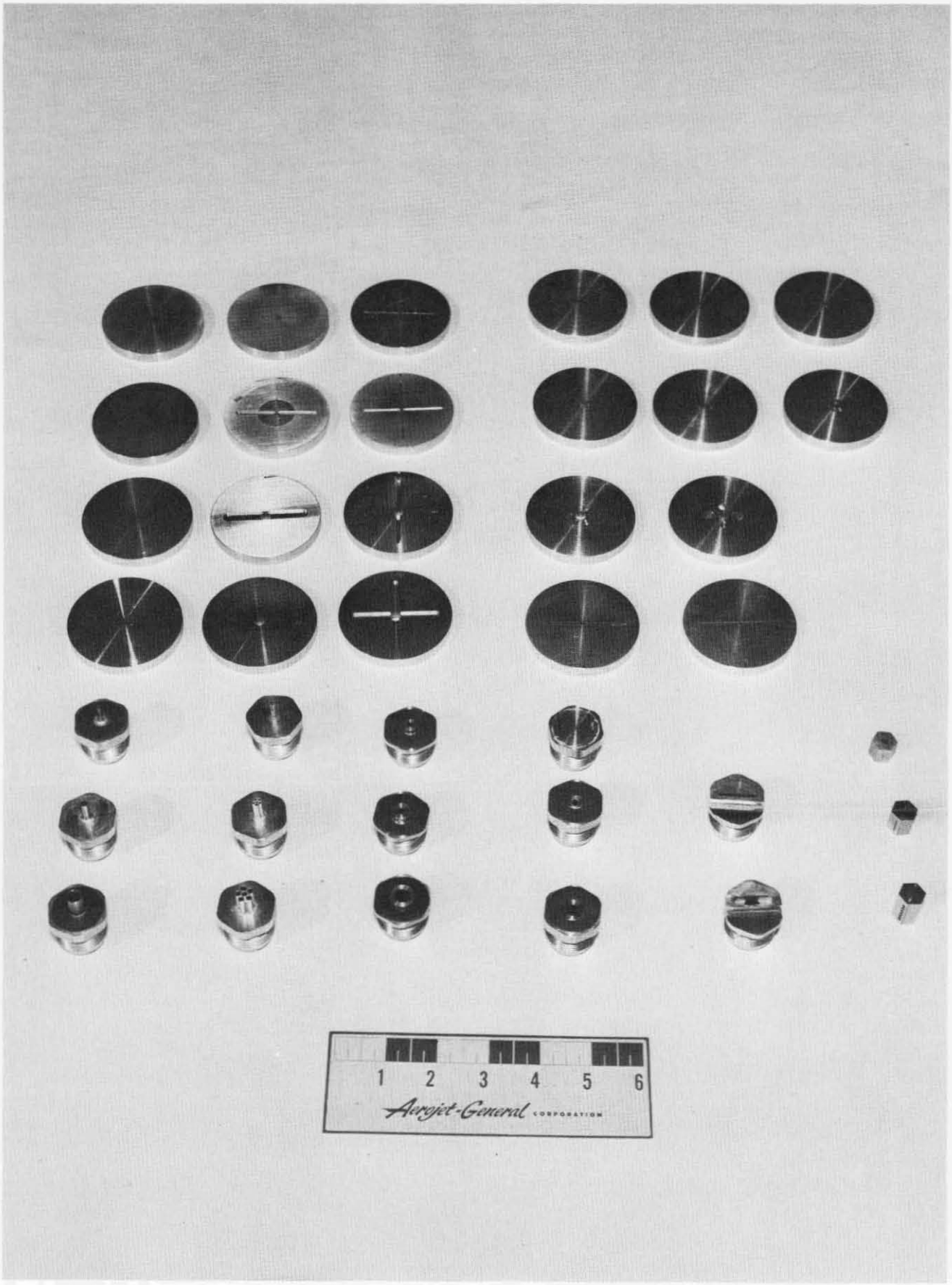

SELECTED COLD FLOW ELEMENTS

GAS/GAS COMBUSTION PROGRAM ALRC CONTRACT NAS3-14379

SPECIES ONE IS H2
SPECIES TWO IS HE
SPECIES THREE IS N2
SPECIES FOUR IS NONE

DIGITAL DATA LISTING

ALPHA DESIG.*TRIPLET-90(15) RAKE LOC.*L/D=7.0 1.0 IN RUN NO 129
29 NOV 71 TEST NO. ~~114~~ 122

CHANNEL	099	002	025	003	003	026	027	028	029	009	015	012
						****** MOLE FRACTIONS ******				OX	FUEL	HE
	TIME (SEC)	POS	ΔP (PSIA)	COMP	PRESS	SPEC 1	SPEC 2	SPEC 3	SPEC 4	MASS FLOW (LBM/SEC)	MASS FLOW (LBM/SEC)	MASS FLOW (LBM/SEC)
	.00	1	.01	NO	YES	.1635	.6543	.1822	.0000	.0281	.0071	.0310
	1.80	2	.01	NO	YES	-.4030	1.3659	.0371	.0000	.0281	.0071	.0310
	3.80	3	.00	NO	YES	-.4869	1.3083	.1787	.0000	.0281	.0071	.0310
	5.80	4	.06	NO	YES	-.2899	1.1389	.1510	.0000	.0281	.0071	.0310
	7.40	5	.43	NO	YES	.0695	1.0742	-.1437	.0000	.0281	.0071	.0310
	9.00	6	.35	NO	YES	.1954	.7952	.0095	.0000	.0281	.0071	.0310
	10.60	7	.02	NO	YES	.2717	.4853	.2430	.0000	.0281	.0071	.0310
	12.20	8	.02	NO	YES	-.8057	1.5613	.2444	.0000	.0281	.0071	.0310
	13.80	9	.21	NO	YES	.2219	.7354	.0427	.0000	.0281	.0071	.0310
	15.40	10	.34	NO	YES	-.2067	.9376	.2691	.0000	.0281	.0071	.0310
	17.20	11	.34	NO	YES	.4654	.5237	.0109	.0000	.0281	.0071	.0310
	18.90	12	.33	NO	YES	-.0004	1.0651	-.0646	.0000	.0281	.0071	.0311
	20.50	13	.34	NO	YES	-.1572	.8792	.2780	.0000	.0281	.0071	.0311
	22.10	14	.12	NO	YES	-.0065	.9966	.0099	.0000	.0281	.0071	.0310
	23.70	15	.11	NO	YES	.2205	.7784	.0011	.0000	.0281	.0071	.0310
	25.30	16	.20	NO	YES	.0603	.9611	-.0215	.0000	.0281	.0071	.0311
	27.10	17	.10	NO	YES	******	2.9208	-.5102	.0000	.0281	.0071	.0311
	28.90	18	.06	NO	YES	-.0492	1.1378	-.0886	.0000	.0281	.0071	.0311
	30.50	19	.55	NO	YES	.4523	.4376	.1102	.0000	.0281	.0071	.0311
	32.10	20	.03	NO	YES	.0380	1.0424	-.0804	.0000	.0281	.0071	.0311
	33.70	21	.06	NO	YES	.0548	.9170	.0281	.0000	.0281	.0071	.0311
	35.30	22	-3.94	NO	YES	******	1.6179	.5337	.0000	.0281	.0071	.0311
	37.10	23	.04	NO	YES	-.0023	1.0176	-.0152	.0000	.0281	.0071	.0311
	38.80	24	.04	NO	YES	-.9867	2.0827	-.0960	.0000	.0281	.0071	.0311
	42.20	1	-10.64	YES	NO	.2537	.6538	.0925	.0000	.0281	.0071	.0311
	43.80	2	-10.66	YES	NO	.2681	.6441	.0877	.0000	.0281	.0071	.0311
	45.40	3	-10.67	YES	NO	.2738	.6524	.0738	.0000	.0281	.0071	.0311
	46.90	4	-10.68	YES	NO	.2716	.6555	.0729	.0000	.0281	.0071	.0311
	48.50	5	-10.69	YES	NO	.3185	.6082	.0733	.0000	.0281	.0071	.0311
	50.10	6	-10.69	YES	NO	.3424	.5832	.0745	.0000	.0281	.0071	.0311
	51.70	7	-10.68	YES	NO	.3079	.6218	.0702	.0000	.0281	.0071	.0311
	53.80	8	-10.71	YES	NO	.2787	.6479	.0734	.0000	.0282	.0071	.0311
	55.70	9	-10.71	YES	NO	.2999	.6191	.0810	.0000	.0282	.0071	.0311
	57.70	10	-10.71	YES	NO	.3167	.6065	.0768	.0000	.0281	.0071	.0311
	59.30	11	-10.72	YES	NO	.3238	.6025	.0737	.0000	.0282	.0071	.0311
	61.30	12	-10.71	YES	NO	.3383	.5914	.0703	.0000	.0281	.0071	.0311
	63.10	13	-10.71	YES	NO	.3463	.5829	.0708	.0000	.0282	.0071	.0311
	65.10	14	-10.72	YES	NO	.2705	.6649	.0646	.0000	.0282	.0071	.0311
	67.10	15	-10.72	YES	NO	.2498	.6864	.0638	.0000	.0282	.0071	.0311
	68.70	16	-10.73	YES	NO	.2630	.6765	.0605	.0000	.0282	.0071	.0311
	70.80	17	-10.72	YES	NO	.3140	.6156	.0704	.0000	.0282	.0071	.0311
	72.80	18	-10.72	YES	NO	.3089	.6202	.0710	.0000	.0282	.0071	.0311
	74.80	19	-10.72	YES	NO	.3473	.5765	.0762	.0000	.0282	.0071	.0311
	76.80	20	-10.72	YES	NO	.3224	.6059	.0717	.0000	.0282	.0071	.0311
	78.90	21	-10.29	YES	NO	.2868	.6427	.0705	.0000	.0282	.0071	.0311

FIG. 2 Pg 1

29 NOV 71 TEST NO. II→122

CHANNEL	099	002	025	003	003	026	027	028	029	009	015	012
	TIME (SEC)	POS	ΔP (PSIA)	COMP	PRESS	******* MOLE FRACTIONS ******* SPEC 1	SPEC 2	SPEC 3	SPEC 4	OX MASS FLOW (LBM/SEC)	FUEL MASS FLOW (LBM/SEC)	HE MASS FLOW (LBM/SEC)
	80.90	22	-10.66	YES	NO	.2324	.7134	.0542	.0000	.0282	.0071	.0311
	82.80	23	-10.39	YES	NO	.2976	.6368	.0656	.0000	.0282	.0071	.0311
	84.90	24	-10.34	YES	NO	.3035	.6331	.0634	.0000	.0282	.0071	.0311

Fig 2 PS2

29 NOV 71 TEST NO. IN122

CHANNEL	099	022	024	023	011	017	014	008	005	006	007
	TIME (SEC)	TMAN OX (DEG R)	TMAN FUEL (DEG R)	TMAN HE (DEG R)	PMAN OX (PSIA)	PMAN FUEL (PSIA)	PMAN HE (PSIA)	PC (PSIA)	PTOT1 (PSIA)	PTOT2 (PSIA)	PSTAT (PSIA)
	.00	495.4	519.8	514.7	313.4	314.5	663.7	303.2	301.9	302.5	302.4
	1.80	495.4	519.7	514.7	313.5	314.5	663.6	303.2	301.8	302.2	302.1
	3.80	495.5	519.8	514.6	313.8	314.3	663.7	303.1	301.8	302.1	302.0
	5.80	495.4	519.6	514.1	312.9	314.1	663.5	303.1	301.3	302.1	302.1
	7.40	495.6	519.8	514.2	312.5	314.0	663.7	302.9	301.9	301.9	301.8
	9.00	495.6	519.7	514.1	312.6	314.1	663.8	303.0	301.9	301.8	301.8
	10.60	495.6	519.7	513.9	313.2	314.1	663.6	302.8	301.4	302.1	301.9
	12.20	495.6	519.7	513.9	313.0	314.0	663.5	302.8	301.5	301.4	302.0
	13.80	495.7	519.7	513.8	313.0	313.9	663.6	303.1	301.6	301.3	301.9
	15.40	495.6	519.6	513.6	313.3	313.8	663.6	302.9	301.7	295.1	302.0
	17.20	495.7	519.5	513.6	313.1	313.9	663.7	302.8	301.6	301.4	301.3
	18.90	495.6	519.5	513.5	312.4	313.8	664.1	302.6	301.5	301.1	301.4
	20.50	495.7	519.5	513.4	312.7	313.8	663.9	302.9	301.2	301.7	301.5
	22.10	495.7	519.4	513.3	312.4	313.8	663.7	302.9	301.2	301.4	301.4
	23.70	495.6	519.3	513.3	312.7	313.7	663.6	302.7	301.2	301.4	301.5
	25.30	495.2	519.0	512.9	312.0	313.7	663.8	302.4	300.1	301.0	301.2
	27.10	495.3	518.9	513.0	312.0	313.8	663.6	302.8	300.6	300.8	301.2
	28.90	495.5	519.1	513.0	312.1	313.6	663.6	303.1	301.3	301.1	301.3
	30.50	495.1	518.7	512.6	313.1	313.6	663.7	302.6	299.9	301.3	301.1
	32.10	495.5	519.0	513.0	312.4	313.5	663.7	303.0	301.2	301.1	301.3
	33.70	495.5	518.8	512.9	312.6	313.6	663.9	302.9	301.3	301.1	301.4
	35.30	495.5	518.8	512.8	312.6	313.7	663.9	302.9	301.3	297.4	301.4
	37.10	495.2	518.4	512.5	313.3	313.4	663.8	302.6	300.8	301.0	301.3
	38.80	495.6	518.8	512.9	312.7	313.5	664.0	302.6	301.8	301.2	301.3
	42.20	495.1	518.2	512.4	312.0	312.7	663.6	301.6	139.1	300.3	301.1
	43.80	495.1	518.2	512.4	312.3	312.6	663.8	301.6	141.8	300.2	300.9
	45.40	495.3	518.2	512.4	311.9	312.5	664.0	301.6	141.4	300.0	300.9
	46.90	495.3	518.1	512.4	311.6	312.7	663.9	301.7	140.6	300.3	301.0
	48.50	495.2	518.1	512.3	311.7	312.6	663.8	301.4	139.1	300.2	300.7
	50.10	495.2	517.9	512.3	311.3	312.6	663.8	301.5	139.7	299.9	300.6
	51.70	495.4	518.1	512.4	311.4	312.6	663.9	301.6	145.2	300.4	300.7
	53.80	495.1	517.8	512.1	311.4	312.7	664.1	301.4	130.2	300.3	300.5
	55.70	495.0	517.8	512.1	311.0	312.6	663.9	301.4	133.0	300.2	300.5
	57.70	495.3	517.8	512.3	311.7	312.5	663.9	301.4	137.0	298.1	300.6
	59.30	494.9	517.5	512.0	311.1	312.4	664.0	301.4	138.6	300.3	300.4
	61.30	494.9	517.5	511.9	311.0	312.5	664.0	301.3	136.8	300.1	300.1
	63.10	494.9	517.4	511.8	311.3	312.5	664.1	301.2	293.4	156.1	300.2
	65.10	494.8	517.2	511.7	310.9	312.4	664.3	301.4	299.7	142.6	300.3
	67.10	494.7	517.2	511.7	310.9	312.4	664.1	301.3	299.7	139.6	300.2
	68.70	494.3	516.8	511.4	310.7	312.3	663.9	301.4	298.8	141.2	300.2
	70.80	494.4	516.9	511.5	311.9	312.5	664.0	301.3	299.7	139.9	300.2
	72.80	494.5	517.0	511.7	311.0	312.3	664.1	301.4	300.1	141.6	300.2
	74.80	494.6	517.0	511.6	310.8	312.3	664.1	301.4	299.8	147.4	300.1
	76.80	494.3	516.7	511.4	311.9	312.3	664.3	301.3	299.4	145.9	300.1
	78.90	494.4	516.9	511.5	310.8	312.0	664.1	301.3	299.5	205.3	234.1

FIG 2 pg 3

29 NOV 71 TEST NO. TR122

CHANNEL	099	022	024	023	011	017	014	008	005	006	007
	TIME (SEC)	TMAN OX (DEG R)	TMAN FUEL (DEG R)	TMAN HE (DEG R)	PMAN OX (PSIA)	PMAN FUEL (PSIA)	PMAN HE (PSIA)	PC (PSIA)	PTOT1 (PSIA)	PTOT2 (PSIA)	PSTAT (PSIA)
	80.90	494.4	516.7	511.6	312.2	313.2	664.6	302.2	301.1	220.9	300.7
	82.80	494.2	516.6	511.5	311.3	311.9	664.1	301.3	292.2	202.1	231.9
	84.90	494.3	516.6	511.5	310.7	311.9	664.1	301.2	299.6	203.3	235.9

FIG 2 PG 4

DATA SUMMARY TEST NO. 119-122

	OX MASS FLOW (LBM/SEC)	FUEL MASS FLOW (LBM/SEC)	HE MASS FLOW (LBM/SEC)	TMAN OX (DEG R)	TMAN FUEL (DEG R)	TMAN HE (DEG R)	PMAN OX (PSIA)	PMAN FUEL (PSIA)	PMAN HE (PSIA)	PC (PSIA)	MIXTURE RATIO
TEST AVERAGE	.0281	.0071	.0311	495.2	518.4	512.7	312.1	313.2	663.9	302.2	3.9610

STEADY STATE PRESSURE & COMPOSITION DATA

STEPPER SWITCH POS.	ΔP SCANI VLV (PSIA)		MOLE FRACTIONS SPEC 1		SPEC 2		SPEC 3		SPEC 4		PTOT 1 (PSIA)		PTOT 2 (PSIA)		PSTAT (PSIA)	
	AVE	LAST	AVE	LAST	AVE	LAST	AVE	LAST	AVE	LAST	AVE	LAST	AVE	LAST	AVE	LAST
1	.00	.00	.2200	.2200	.6744	.6744	.1056	.1056	.0000	.0000	301.9	301.9	302.5	302.5	302.4	302.4
2	.00	.00	.2332	.2332	.6663	.6663	.1005	.1005	.0000	.0000	301.8	301.8	302.2	302.2	302.1	302.1
3	.00	.00	.2387	.2387	.6766	.6766	.0847	.0847	.0000	.0000	301.8	301.8	302.1	302.1	302.0	302.0
4	.00	.00	.2367	.2367	.6796	.6796	.0836	.0836	.0000	.0000	301.3	301.3	302.1	302.1	302.1	302.1
5	.37	.37	.2798	.2798	.6355	.6355	.0847	.0847	.0000	.0000	301.9	301.9	301.9	301.9	301.8	301.8
6	.29	.29	.3019	.3019	.6116	.6116	.0865	.0865	.0000	.0000	301.9	301.9	301.8	301.8	301.8	301.8
7	.00	.00	.2701	.2701	.6487	.6487	.0811	.0811	.0000	.0000	301.4	301.4	302.1	302.1	301.9	301.9
8	.00	.00	.2432	.2432	.6724	.6724	.0844	.0844	.0000	.0000	301.5	301.5	301.4	301.4	302.0	302.0
9	.15	.15	.2624	.2624	.6443	.6443	.0933	.0933	.0000	.0000	301.6	301.6	301.3	301.3	301.9	301.9
10	.28	.28	.2780	.2780	.6333	.6333	.0887	.0887	.0000	.0000	301.7	301.7	295.1	295.1	302.0	302.0
11	.28	.28	.2847	.2847	.6300	.6300	.0853	.0853	.0000	.0000	301.6	301.6	301.4	301.4	301.3	301.3
12	.27	.27	.2983	.2983	.6201	.6201	.0816	.0816	.0000	.0000	301.5	301.5	301.1	301.1	301.4	301.4
13	.28	.28	.3057	.3057	.6121	.6121	.0823	.0823	.0000	.0000	301.2	301.2	301.7	301.7	301.5	301.5
14	.06	.06	.2359	.2359	.6899	.6899	.0742	.0742	.0000	.0000	301.2	301.2	301.4	301.4	301.4	301.4
15	.05	.05	.2171	.2171	.7098	.7098	.0730	.0730	.0000	.0000	301.2	301.2	301.4	301.4	301.5	301.5
16	.14	.14	.2293	.2293	.7013	.7013	.0694	.0694	.0000	.0000	300.1	300.1	301.0	301.0	301.2	301.2
17	.04	.04	.2757	.2757	.6430	.6430	.0813	.0813	.0000	.0000	300.6	300.6	300.8	300.8	301.2	301.2
18	.00	.00	.2710	.2710	.6471	.6471	.0820	.0820	.0000	.0000	301.3	301.3	301.1	301.1	301.3	301.3
19	.49	.49	.3064	.3064	.6050	.6050	.0885	.0885	.0000	.0000	299.9	299.9	301.3	301.3	301.1	301.1
20	.00	.00	.2834	.2834	.6336	.6336	.0830	.0830	.0000	.0000	301.2	301.2	301.1	301.1	301.3	301.3
21	.00	.00	.0000	.0000	.0000	.0000	.0000	.0000	.0000	.0000	301.3	301.3	301.1	301.1	301.4	301.4
22	.00	.00	.2017	.2017	.7364	.7364	.0619	.0619	.0000	.0000	.0	.0	.0	.0	.0	.0
23	.04	.04	.0000	.0000	.0000	.0000	.0000	.0000	.0000	.0000	300.8	300.8	301.0	301.0	301.3	301.3
24	.04	.04	.0000	.0000	.0000	.0000	.0000	.0000	.0000	.0000	301.8	301.8	301.2	301.2	301.3	301.3

***** STEPPER SWITCH POS. LEGEND *****

POS. 1-20	TOTAL PRESSURE PROBE ELEMENTS BEING READ (POS. NUMBER CORRESPONDS TO ELEMENT NO.)
POS. 21	THREE PROBE STATIC PRESSURES READ AND AVERAGED (ZERO ΔP CHECK)
POS. 22	CALIBRATION GAS SPECIES DATA FROM MASS SPEC
POS. 23	AMBIENT REFERENCE PRESSURES

FIG 2 PG 5

AEROJET LIQUID ROCKET COMPANY
ANALYSIS OF COLD-FLOW INJECTOR TEST RESULTS

RUN NO. 129 TEST NO. 122

TEST DATA

CHAMBER DIAMETER	=	1.50	INCH
AXIAL POSITION	=	1.00	INCH
OXIDIZER FLOW RATE	=	.02813	LBM/SEC
FUEL FLOW RATE	=	.00710	LBM/SEC
HELIUM FLOW RATE	=	.03107	LBM/SEC
MIXTURE RATIO	=	3.96	(COLD FLOW)
FUEL MAN. PRESS.	=	313.2	PSIA
OX. MAN. PRESS.	=	312.1	PSIA
HE MAN. PRESS.	=	663.9	PSIA
FUEL MAN. TEMP.	=	518.4	DEG RANKINE
OX. MAN. TEMP.	=	495.2	DEG RANKINE
HE MAN. TEMP.	=	512.7	DEG RANKINE

CALCULATED TEST VARIABLES

N2 INJECTION VEL.	=	155.90	FT/SEC
H2 INJECTION VEL.	=	598.99	FT/SEC
HE INJECTION VEL.	=	15.31	FT/SEC
N2 MOMENTUM	=	4.39	LB-FT/SEC-SEC
H2 MOMENTUM	=	4.25	LB-FT/SEC-SEC
MOMENTUM RATIO	=	.97	WFVF/WOVO
MOMENTUM DIFF.	=	-.13	LB-FT/SEC-SEC
VELOCITY RATIO	=	3.84	VF/VO
VELOCITY DIFF.	=	443.09	FT/SEC
VEL. RATIO--HE/N2	=	.10	VHE/VO
FUEL-OX SOURCE VEL.	=	209.85	FT/SEC
DELTA P OXID INJ.	=	9.92	PSI
DELTA P FUEL INJ.	=	10.99	PSI
OX INJ STIFFNESS	=	.0328	ΔP/PC
FUEL INJ STIFFNESS	=	.0364	ΔP/PC
OX AREA RATIO	=	.0092	AO/ACHAM
FUEL AREA RATIO	=	.0088	AF/ACHAM
VELOCITY-AREA RATIO	=	3.6771	AF*VF/AO*VO
MIXTURE-AREA RATIO	=	.2416	AF*WF/AO*WO
MOMENTUM-AREA RATIO	=	.9283	AF*VF*WF/AO*VO*WO
OX PCT TOTAL FLOW	=	.7984	WO/WO+WF
FUEL EQ OF STATE	=	.8510	TF/PC*MWF
OX EQ OF STATE	=	.0585	TO/PC*MWO
NORM/AX INJ MOM	=	.4068	

FIG 3 Pg 1

MEASURED ΔP (PSIA)

ANGLE (DEG)	RADIAL POSITION (IN) .0000	.1250	.2500	.3750	.5000	.6250
0.	.2906	.3676	.0000	.0000	.0000	.0000
45.	.2906	.0411	.1373	.1158	.0462	.0580
90.	.2906	.2703	.2818	.2797	.1453	.0000
135.	.2906	.0000	.1373	.1158	.0462	.0580
180.	.2906	.0000	.0000	.0000	.0000	.0000
225.	.2906	.0000	.1373	.1158	.0462	.0580
270.	.2906	.2785	.2818	.2797	.1453	.0000
315.	.2906	.4928	.1373	.1158	.0462	.0580

MEASURED P-TOTAL (PSIA)

ANGLE (DEG)	RADIAL POSITION (IN) .0000	.1250	.2500	.3750	.5000	.6250
0.	302.1106	302.2176	302.0900	301.9600	302.0600	302.4500
45.	302.1106	301.2411	301.3373	301.7633	301.5162	301.4880
90.	302.1106	301.7003	301.6118	302.2397	302.0653	301.9700
135.	302.1106	301.3200	301.3373	301.7633	301.5162	301.4880
180.	302.1106	301.9500	302.0900	301.9600	302.0600	302.4500
225.	302.1106	301.2700	301.3373	301.7633	301.5162	301.4880
270.	302.1106	301.7685	301.6118	302.2397	302.0653	301.9700
315.	302.1106	301.5928	301.3373	301.7633	301.5162	301.4880

MEASURED P-STATIC (PSIA)

ANGLE (DEG)	RADIAL POSITION (IN) .0000	.1250	.2500	.3750	.5000	.6250
0.	301.8200	301.8500	302.0900	301.9600	302.0600	302.4500
45.	301.8200	301.2000	301.2000	301.6475	301.4700	301.4300
90.	301.8200	301.4300	301.3300	301.9600	301.9200	301.9700
135.	301.8200	301.3200	301.2000	301.6475	301.4700	301.4300
180.	301.8200	301.9500	302.0900	301.9600	302.0600	302.4500
225.	301.8200	301.2700	301.2000	301.6475	301.4700	301.4300
270.	301.8200	301.4900	301.3300	301.9600	301.9200	301.9700
315.	301.8200	301.1000	301.2000	301.6475	301.4700	301.4300

Fig 3 Pg 2

CALCULATED RESULTS

LOCAL OX FLUX (LBM/SEC-SI)

ANGLE (DEG)	RADIAL POSITION (IN) .0000	.1250	.2500	.3750	.5000	.6250
0.	.08803	.09697	.00000	.00000	.00000	.00000
45.	.08803	.03130	.04969	.05097	.03002	.03422
90.	.08803	.08081	.08539	.08783	.06577	.00000
135.	.08803	.00000	.04969	.05097	.03002	.03422
180.	.08803	.00000	.00000	.00000	.00000	.00000
225.	.08803	.00000	.04969	.05097	.03002	.03422
270.	.08803	.08275	.08539	.08783	.06577	.00000
315.	.08803	.11679	.04969	.05097	.03002	.03422

LOCAL FUEL FLUX (LBM/SEC-SI)

ANGLE (DEG)	RADIAL POSITION (IN) .0000	.1250	.2500	.3750	.5000	.6250
0.	.02211	.02304	.00000	.00000	.00000	.00000
45.	.02211	.00763	.01180	.01118	.00642	.00783
90.	.02211	.02127	.02050	.01980	.01330	.00000
135.	.02211	.00000	.01180	.01118	.00642	.00783
180.	.02211	.00000	.00000	.00000	.00000	.00000
225.	.02211	.00000	.01180	.01118	.00642	.00783
270.	.02211	.02212	.02050	.01980	.01330	.00000
315.	.02211	.02909	.01180	.01118	.00642	.00783

Fig 3 Pg 3

LOCAL MIXTURE RATIO (O/F)

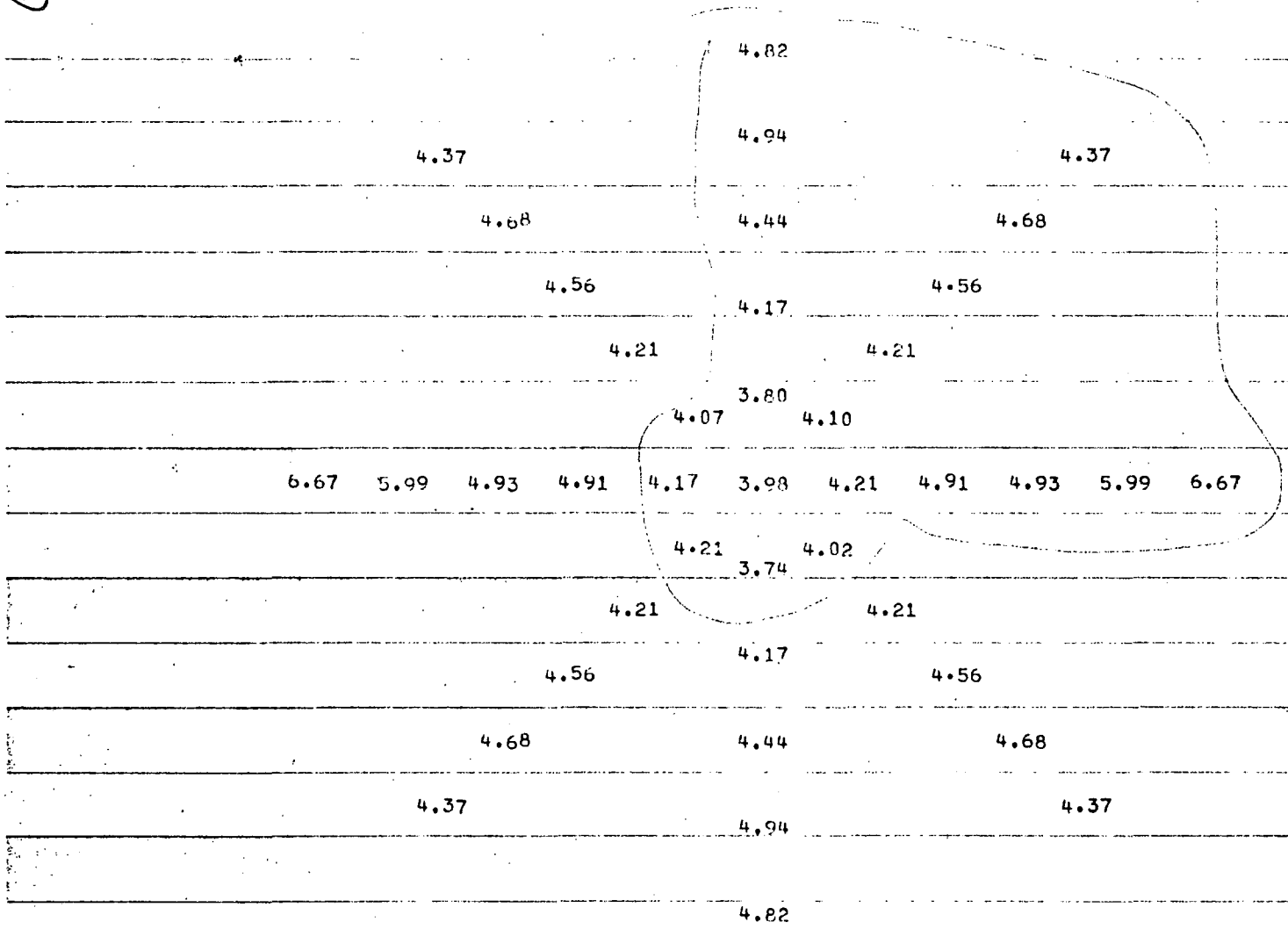

RB3 pg4

LOCAL MASS FLUX (LBM/SEC-SI)

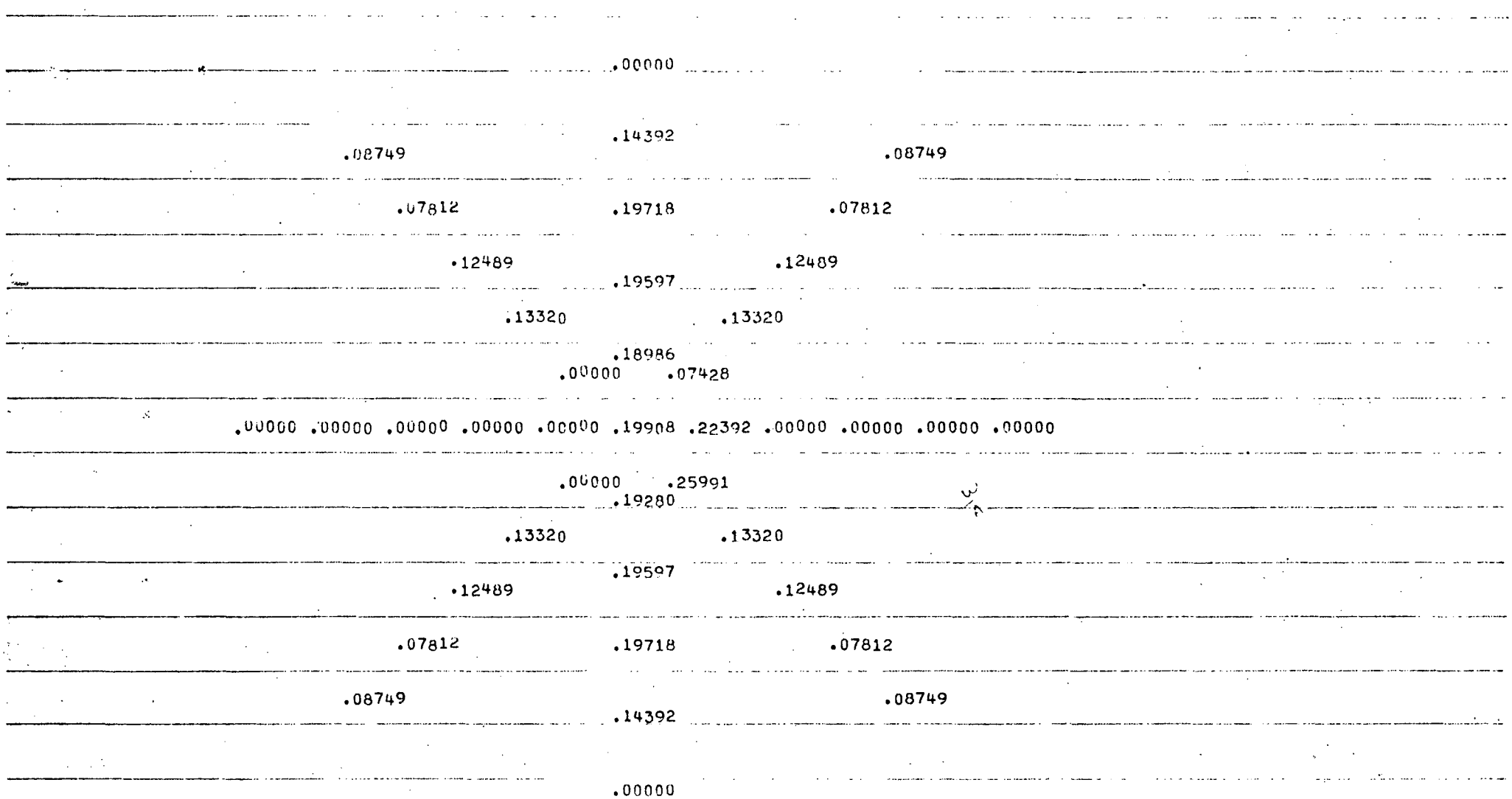

FIG 3 Pg 5

LOCAL COMPATABILITY COEFFICIENT

.00

.00

.00 .00

.00 1.63 .00

1.04 1.04

1.62

1.05 1.05

1.57

.00 .73

.00 .00 .00 .00 .00 1.67 1.79 .00 .00 .00 .00

.00 2.09

1.60

1.05 1.05

1.62

1.04 1.04

.00 1.63 .00

.00 .00

.00

.00

FIG 3 pg 6

		RADIAL POSITION INTEGRATED TO						
		.7500	.6250	.5000	.3750	.2500	.1250	
MEASURED OVERALL MIXTURE RATIO	=	3.9610						
INTEGRATED MIXTURE RATIO	=	4.4099	4.4177	4.3549	4.2021	4.0456	3.9710	
MEASURED OVERALL MASS FLOW RATE	=	.0663						LBM/SEC
MEASURED OVERALL OX FLOW RATE	=	.0281						LBM/SEC
MEASURED OVERALL FUEL FLOW RATE	=	.0071						LBM/SEC
INTEGRATED MASS FLOW RATE	=	.1335	.1099	.0839	.0521	.0243	.0071	LBM/SEC
INTEGRATED OX FLOW RATE	=	.0550	.0458	.0352	.0217	.0102	.0031	LBM/SEC
INTEGRATED FUEL FLOW RATE	=	.0125	.0104	.0081	.0052	.0025	.0008	LBM/SEC
MIXING COEFFICIENT	=	97.61	97.22	97.18	98.05	98.24	98.85	PERCENT
ETAM	=	95.95	95.32	95.39	96.42	97.72	97.81	PERCENT
PERCENT NOMINAL CSTAR	=	99.93	99.91	99.91	99.93	99.95	99.98	PERCENT

CALCULATED RESULTS AT RADIAL LOCATION SHOWING INTEGRATED
MASS FLOW RATE (OX+FUEL) EQUAL TO MEASURED FLOW RATE

RADIAL POSITION	=	.4387
INTEGRATED MIXTURE RATIO	=	4.2966
INTEGRATED OX FLOW RATE	=	.0286
INTEGRATED FUEL FLOW RATE	=	.0067
MIXING COEFFICIENT	=	97.61
ETAM	=	95.90
PERCENT NOMINAL CSTAR	=	99.92

FIG 3 P87

FIG 9

SHEET 1 OF 11

TEST DATA SUMMARY

	Test No.	Run No.	Basic Elem.	Variation	F/E	A_s/A_o	T_o	T_f	ΔP_{oj}	ΔP_{fj}	$\omega_s V_s/\omega_o V_o$ Normal	$\omega_s V_s/\omega_o V_o$ Ax. Mom.	V_s/V_o	L/D	O/F	$\bar{R}$	$(O/F)_I$	E_m	η_m	$\%C^*$
	Units →	—	—	—	Lbf	—	°R	°R	psi	psi	—	—	—	—	—					
*	1	6	Co-Ax	Swear	15	0.99	518	540	6.41	7.02	0.94	0.00	3.72	3	3.97	.211	3.77	47.8	58.0	85.79
*	2	5					517	541 (535)	5.72	6.33	0.94	0.00	3.73	7	3.96	121% Mass Int. .500	4.06	72.1	62.9	96.83
◇	3	7					519	542	6.34	6.78	0.95	0.00	3.74	15	3.94	145% Mass Int. .500	4.63	96.5	94.3	99.95
*	4	8					517	542	6.33	6.93	0.95	0.00	3.75	30	3.94	45% M.I. .750	4.20	97.9	96.3	99.85
*	5	9					504	530	5.27	14.11	3.65	0.00	7.35	7	2.01	.362	2.43	82.4	75.7	98.43
	6	10					500	529	14.88	1.72	0.35	0.00	2.29	7	6.49	120% M.I. .275	6.74	55.4	52.0	93.66
*	7	11					229.7	371.7 (338)	7.29	1.64	1.30	0.00	5.44	7	4.19	214% M.I. .625	4.38	79.9	69.0	98.19
* ◇	8	13		3 Hole Swirler			519	541	26.50	3.85	0.92	(0.42) 0.00	3.68	3	3.99	.538	2.95	92.5	87.4	99.59
	9	12					514	541	26.52	3.99	(0.66) 0.92	(0.42) 0.00	3.68	7	4.02	.330	2.81	98.2	97.1	99.98
	10	14					515	542 (535)	25.96	3.21	0.92	(0.42) 0.00	3.69	15	4.01	43% M.I. .504 .75	5.30	98.5	97.6	99.99
	11	15					516	542	26.13	3.31	0.92	(0.42) 0.00	3.69	30	4.01	23% M.I. .750	3.19	99.9	99.8	100.00
	12	16					518	543	20.06	10.58	(2.29) 3.17	(0.18) 0.00	6.84	7	2.16	.412	3.15	95.6	92.9	99.93
*	13	17					510	541	35.07	-0.14	(0.26) 0.35	(0.64) 0.00	2.30	7	6.49	.325	7.67	96.9	95.5	100.01
	14	18					207.5	348.8 (317)	8.48	0.58	(1.07) 1.49	(0.21) 0.00	5.93	7	3.99	.325	7.24	95.1	95.4	100.08
	15.2	20		6 Hole Swirler			513	531	15.21	4.44	(0.26) 0.93	(.21) 0.00	3.68	7	3.96	.334	5.13	94.3	91.2	99.83
*	16	22		Increased Shear		0.88	509	529	13.84	17.20	1.04	0.00	4.12	3	3.98	.444	3.88	73.3	68.6	96.61
*	17	21					512	530 (526)	13.45	16.93	1.04	0.00	4.12	7	3.97	.361	4.20	83.1	75.4	99.05
◇	18	23					509	529	13.15	16.81	1.03	0.00	4.11	15	3.99	.439	3.08	98.1	96.7	99.96
◇	19	24					507	528	13.55	17.04	1.03	0.00	4.12	30	3.99	.500	5.00	99.4	99.0	100.00

	Test No.	Run No.	Basic Elem.	Elem. Variation	F/E	A_s/A_o	T_o	T_t	ΔP_{os}	ΔP_{ts}	$\dot{w}_s V_s/\dot{w}_o V_o$	Norm Ax. Mom.	V_s/V_o	L/D	θ/F	$\bar{R}$	$(\theta/F)_s$	E_m	η_m	%C*
	20.0	27	Co-Ax	Increased Swirl	15	0.88						0.00		7		Data Not Available				
*	20.1	28		½ $\dot{w}_{No}$			501	528	9.39	48.30	4.11		8.27	7	2.01	.290	2.77	98.0	97.1	99.96
*	20.2	29		0 $\dot{w}_{No}$			502	527	10.48	50.11	4.13		8.27	7	2.00	.136	4.39	95.1	96.5	99.81
*	21	25					500	529	17.25	6.93	0.24		2.00	7	8.35	.462	6.26	80.2	73.6	99.90
*	22	26					207.2	361.7 (330)	2.76	4.84	1.75	0.00	6.94	7	3.97	.281	5.85	86.9	80.4	99.29
*	23	30		Shear	3	0.49	536	537	11.63	41.32	1.76	0.00	7.08	7	4.01	.448	~~4.02~~ 3.96	89.7	85.9	100.19
*	24	31					533	540	11.10	41.66	1.80		7.18	15	4.00	.264	4.50	95.8	93.4	99.80
*	25	32					532	543	8.48	112.3	7.27		14.51	15	2.00	~~.252~~ .250	~~2.72~~ 2.70 (95% Mix. Integral m)	~~94.2~~ 95.2	~~91.8~~ 91.7	~~99.76~~ 99.75
*	26	33					532	537	14.22	20.25	0.79	0.00	4.77	15	6.01	.185	6.96	92.0	93.3	100.69
*	27	34		2 Hole Shaker			529	537	21.10	44.54	1.77	0.31	7.14	15	4.04	.444	4.47	96.4	93.5	99.93
	28	35					530	542	14.06	114.4	7.25	0.094	14.50	15	2.00	.362	2.70	96.5	93.6	99.87
*	29	36					529	538	23.62	20.94	0.79	0.51	4.79	15	6.02	.239	6.50	96.2	94.5	100.02
(30) *	31	37	Flat "I" Triplet		15	0.98	514	527	44.62	40.82	0.92	0.92	8.66	3	3.97	.319	4.55	87.7	83.9	100.23
*	32	38					509	522	44.20	39.97	0.93	0.93	3.67	7	5.96	.672	4.42	94.0	89.8	100.06
*	33	39					514	525	43.70	39.65	0.94	0.94	3.69	15	3.93	.463	4.41	98.3	97.6	99.98
	34	40					514	526	43.29	39.78	0.93	0.93	3.67	30	3.96	~~.372~~ .375	~~4.64~~ 4.66 (1½% M.I.)	~~99.1~~ 99.0	~~98.9~~ 98.9	~~99.99~~ 99.99
◇ *	35	41					513	520	52.91	54.58	2.59	2.59	6.09	7	2.36	.150	2.62	88.4	82.3	98.43
*	36	42					502	523	36.22	28.26	0.38	0.38	2.38	7	6.22	.595	7.48	96.3	93.4	99.83
	37	44					234.6	310.7	18.78	12.75	1.15	1.15	4.64	7	4.05	~~.252~~ .250	~~3.16~~ 7.98	~~90.1~~ 90.1	~~88.2~~ 88.2	~~100.48~~ 100.48
◇																				

SHT 3 OF 11

	Test No.	Run No.	Basic Elem.	Elem. Variation	F/E	A_t/A_o	T_o	T_t	ΔP_{o3}	ΔP_{s3}	$\dot{w}_o V_t / \dot{w}_t V_o$	Norm Ax Mom.	V_t/V_o	L/D	θ/F	$\bar{R}$	$(\theta/F)_s$	E_m	η_m	% C^*
◇	38	45	Flat "I" Triplet		50	0.50	522	493	40.56	54.84	1.69	1.69	6.68	7	3.94	.625	5.72	89.9	81.4	99.33
◇	39	46					520	495	41.57	55.00	1.74	1.74	6.79	3	3.91	.657	5.49	89.0	81.9	98.17
✳	40	47		67%	3	2.05	537	532	23.92	11.24	0.42	0.42	1.67	15	4.02	.219	4.61	95.6	94.0	99.99
	41	49		34%		0.69	536	532	48.93	53.48	1.27	1.27	5.04	7	3.98	.625	5.22	95.2	91.8	101.65
◇	42	48					536	533	49.38	53.59	1.27	1.27	5.05	15	3.98	.214	4.94	98.6	97.3	100.06
✳	43	50					537	528	68.88	57.65	4.93	4.93	9.90	15	2.01	.234	2.54	97.7	96.6	99.87
✳ ◇	44	51					525	520	38.84	49.66	0.55	0.55	3.33	15	6.01	.249	6.71	96.9	94.6	100.07
✳	44.6	52					518	516	40.86	114.07	0.57	0.57	3.39	15	5.94	.229	6.82	97.0	94.9	100.17
✳	44.4	53					521	515	50.20	109.88	1.24	1.24	4.98	15	4.01	.195	5.15	99.0	98.4	100.02
✳	44.2	54					526	513	70.39	96.43	4.93	4.93	9.87	15	2.00	.202	2.60	98.3	97.4	99.96
	45	55		32%	50	0.48	511	498	40.21	40.30	1.77	1.77	6.97	3	3.93	.650	5.42	91.4	85.4	99.10
✳	46	56	Pentad		3	2.02	520	517	46.26	29.86	0.43	0.43	1.72	15	3.98	.375	4.68	96.6	93.8	100.07
	47	57					523	516	47.56	30.90	0.43	0.43	1.71	7	3.99	.625	4.81	91.0	85.4	100.80
	48	58		34%		0.43	522	518	45.84	29.86	2.00	2.00	7.99	15	4.00	.213	5.42	98.6	98.1	99.97
	48.2	59					529	516	64.31	39.52	7.91	7.91	15.76	15	1.99	.250	2.48	97.1	95.2	100.00
	48.6	60					525	514	42.01	28.05	0.14	4.82	4.82	15	6.55	.514	8.45	97.0	94.3	100.00
	50 ~~47~~	62 ~~55~~	Doublet			1.00	532	524	←			.58	6.88	15	1.99	.631	2.30	93.0	87.5	99.7
	49 ~~50~~	63 ~~52~~					531	523				.58	3.42	15	4.00	.451	4.90	91.5	87.3	99.83

FIG. 4
SHT 4 OF 11

SHT 4 OF 11

Test No.	Run No.	Basic Elem	Elem. Variation	F/E	A_s/A_o	T_o	T_t	ΔP_{os}	ΔP_{ts}	$\dot{w}_s\sqrt{\theta_s}/\dot{w}_o$	Nozz. Mom. A_s/A_o	V_s/V_o	L/D	O/F	$\bar{R}$	$(O/F)_t$	E_m	η_m	% C^*
51	61	Doublet		3	1.00								15		(No Data)				
51.4	64		0°	15	0.51								7						
51.5	65		90° C.W.			532	512	17.83	32.98	1.63	0.58	6.56	7	4.02	.750	5.06 (37% M.I.)	81.4	73.2	97.27
52	87	Co-Ax Shear		3	0.99	534	539 (536)	11.66			0.00		15	3.81	.750	4.77 (Wt)	77.5	67.9	100.44
53	88					533	542	12.14			0.00		7	3.94	.75	5.39 ~	56.0	41.2	100.44
54	89					199	181	-.24			0.00		15	4.00	.190	4.92	84.8	76.1	98.34
55	91		2 Hole Swirler			459	487 (485)	24.03					15	3.97	.225	5.10	91.4	90.1	100.07
56	92					501	531 (481)	25.11					7	3.97	.500	4.24	87.3	79.0	101.38
57	90					200	180	2.72					15	3.98	.271	5.05	95.3	93.4	100.03
58	93		Increased Shear		1.59	531	535 (485)	17.66			0.00		7	3.94	.750	4.03 (100% M.I.)	70.5	58.4	98.81
59	94					530	538	18.04			0.00		15	3.95	.688	4.31 (Wt) 61% Mass Interaction	81.4	72.0	99.35
60	84	Co-Ax Shear		50	0.50	491	520	8.06			0		7	3.81	.750	3.52	73.1	66.2	96.57
61	83					490.6	521	8.16			0		3	3.81	.7293	5.60	63.4	59.5	95.07
62	85		3 Hole Swirler			497	520	29.20					7	3.76	.750	80% Mass Interaction 5.39	95.8	920	99.9
63	86		6 Hole Swirler			506	521	14.9					7	3.78	.375	4.38	94.0	88.9	99.91
65	66	Pentad	67%	50	0.95	532	497	41.24	34.56	0.88	0.88	3.48	7	3.94	.727	6.65	91.5	84.6	99.55
65.1	67					530	498	42.07	34.91	0.88	0.88	3.49	3	3.95	.375	4.54	87.3	83.6	97.90
66	68		32%			539	497	41.07	39.76	0.87	0.87	3.43	3	3.94	.375	5.16	91.4	86.5	99.64
67	69												3						
* 67	70					497.6	399.9	39.47	36.87	0.74	0.74	2.95	3	3.99	.744	(No Mass Spec. Composition Data)			

One Test

(4A)

← Fuel Manifold Pressure Instrumentation → Line leakage occurred these tests – Must Approximate Fuel Injector ΔP from other tests with similar type elements and run conditions to calculate full injection parameters

FIG 9

SHT 5 OF 11

Test No.	Run No.	Basic Elem.	Elem. Var	F/E	A_c/A_o	T_o	T_f	ΔP_{oj}	ΔP_{tj}	$w_c V_c / w_o V_o$	Norm Av. Mom.	V_c/V_o	L/D	O/F	$\bar{R}$	$(O/F)_s$	E_m	η_m	% C^*
68.0	71	Parallel Sweet	0°	50	1.00	491	527	49.33	10.28	1.01	0	3.89	3	~~3.84~~					
68.1	72		90° C.W.										3	3.84	.397	7.94	63.4	55.0	92.73
69.0	73		0°			491	526	50.67	9.82	1.01	0	3.88	7	3.83	.750	5.68	86.3	77.3	98.98
69.1	74		90° C.W.										7						
70.0	75		0°			491	524	51.14	9.48	1.00	0	3.86	15	3.85	.619	6.44	96.0	92.7	99.95
70.1	76		90° C.W.										15						
71.0	77		0°			491	526						3	2.50	.483	4.60	61.0	53.8	91.01
71.1	78		90° C.W.										3						
72.0	79		90° C.W.			485	525						3	5.77	.750	8.54	72.9	65.7	95.93
72.1	80		0°										3						
73.0	81		0°			366	430						3	3.88	.315	6.92	71.8	63.8	94.91
73.1	82		90° C.W.										3						
74	215		0°	3		507	523	14.11	9.48	.90	0	3.59	7	3.99	.375	(152% M.I.) 4.34	92.2	89.9	100.18
9.74	216		90° C.W.										7						
9.75	217		90° C.W.			512	526	11.22	22.46	2.96	0	6.51	7	2.20	.375	(152% M.I.) 3.26	90.8	88.3	99.37
75	218		0°										7						
76	219		0°			509	522	14.90	4.26	0.41	0	2.41	7	5.92	.500	(151% M.I.) 5.91	94.4	91.6	100.97
9.76	220		90° C.W.										7						
77.6	161	Doublet .200" Spacing	90° C.C.W.	15	1.00	502	526	16.94	4.23	.36	.58	2.28	7	6.38	.750	(73% M.I.) 8.06	84.7	76.9	99.14
77.5	162		0°										7						
77.3	163		0°			503	525	9.95	18.05	3.69	.58	7.32	7	1.98	.750	3.39	78.2	69.6	94.94
77.4	164		90° C.C.W.										7						
77.2	165		90° C.C.W.			498	525	13.40	6.93	.94	.58	3.70	7	3.96	.75	5.23	80.4	69.8	98.4
97.1	166	.200" Spacing	0°										7						

Fuel Manifold Pressure Error on These Tests

SHT 6 OF 11

Test	Run	Elem	Variation	F/E	A_E/A_o	T_o	T_f	ΔP_{oJ}	ΔP_{fJ}	$w_E V_E / w_o V_o$	Norm Av. Mom	V_E/V_o	L/D	O/F	$\bar{R}$	$(O/F)_I$	E_m	η_m	% C^*
78.1	139	Doublet - .100" Spacing	0°	1.5	1.00	509	525	10.81	6.66	.88	.58	3.56	3.1	4.03	.624	5.29 (51% Mass Int.)	70.7	61.3	95.38
78.2	140		90° C.C.W.										3.1						
79.1	141		0°			508	525	9.99	8.47	.92	.58	3.64	7	3.95	.750	5.05 (79% M.I.)	85.5	76.0	98.85
79.2	142		90° C.C.W.										7						
80.1	143		0°			507	525	10.18	7.35	.92	.58	3.64	15	3.95	.750	4.75 (64% M.I.)	95.5	91.6	99.88
80.2	144		90° C.C.W.										15						
81.1	145		0°			506	525	10.35	9.32	.92	.58	3.64	30	3.96	.750	4.55	97.8	95.7	99.48
81.2	146		90° C.C.W.										30						
82.11	147		0°										7						
82.12	148		0°			512	525	7.20	21.66	8.67	.58	7.23	7	1.97	.25	3.85	82.6	72.3	97.52
82.2	149		90° C.C.W.										7						
83.2	150		90° C.C.W.			501	525	13.61	5.68	.136	.58	2.29	7	6.36	.75	7.52	86.5	79.2	99.75
83.1	151		0°										7						
84.11	152		0°			Missing Cold Test - Not Recorded							7						
84.12	153		0°			on Tape @ Aerophysics Lab							7						
84.13	154		0°										7						
85.1	155	.050" Spacing	0°			506	525	12.89	11.40	.92	.58	3.65	7	3.96	.75	5.09	82.0	71.8	98.42
85.2	156		90° C.C.W.										7						
85.4	157		90° C.C.W.			506	525	9.86	30.80	8.68	.58	7.29	7	1.98	.375	3.32	82.3	72.8	97.85
85.3	158		0°										7						
85.5	159		0°			497	525	16.04	5.50	.136	.58	2.29	7	6.41	.541	8.29	85.6	78.2	100.02
85.6	160		90° C.C.W.										7						
* 86	95	Flat "I" Triplet		3	1.01	538	541	48.60	45.18	0.88	0.88	3.49	15	3.97 est.	.565	4.93	97.9	96.1	100.14
87	96					210.8	182.0	18.81	22.09	0.73	0.73	2.95	15	4.03	.554.75	7.0	≥ 72	≥ 64	≥ 96
* 88	99		34%		???	533	544	75.15	37.95	0.89	0.89	3.53	15	3.98	.249	4.58	98.1	97.4	99.96

Note: Test 87 Distribution is Approximate & is Result of 2 Phase Ox. Inj.

SHT 7 OF 11

	Test	Run	Elem	Var		F/E	A_s/A_o	T_o	T_f	ΔP_{OJ}	ΔP_{FS}	$\dot{w}_s V_s t / \dot{w}_o V_o$	$\frac{\text{Norm}}{A_x \cdot M_{mm}}$	V_s/V_o	L/D	O/F	$\bar{R}$	$(O/F)_s$	E_m	η_m	% C^*
*	89	100	Flat "I" Triplet	67%		15	0.99	517	535	41.91	36.22	0.95	0.95	3.73	7	3.91	.604	4.98	95.3	91.7	99.92
*	90	101						510	531	43.74	37.99	0.94	0.94	3.70	3	3.96	.517	4.16	90.2	87.2	100.33
*	91	104				50	1.01	480	518	34.94	31.33	0.98	0.98	3.82	3	3.89	.556	5.09	85.1	80.6	99.48
*	92	106						395.6	423.4	27.45	23.57	0.98	0.98	3.79	3	3.89	.367	5.62	84.2	81.3	99.33
	93	171		67%			0.51	490	530	34.28	43.45	2.06	2.06	7.82	3	3.86	.611	5A9	89.6	85.1	99.79
*	94	105					1.01	482	518	34.27	30.89	1.03	1.03	3.91	7	3.79	.481	4.56	97.1	95.9	99.96
*	95	103	Pentad			15	0.98	503	528	37.99	34.79	0.95	0.95	3.76	7	3.95	.575	4.70	92.6	88.8	99.79
*	96	102						513	533	38.65	35.55	0.94	0.94	3.72	3	3.96	.506	4.20	90.3	87.5	100.26
*	97	98		34%		3	1.00	522	539	50.94	45.33	0.91	0.91	3.61	15	3.98	.290	4.69	98.6	97.9	100.01
	98	97						204.5	177.0	3.76	0.90	0.72	0.72	2.95	15	4.08	45% .75	60 to 80	85 to 91	80 to 88	102 to 106
								Test 98 Data Indicates Two Phase Oxidizer Injection Distribution; Mixing Efficiency Data Probably Meaningless												
◇	99	107	Co-Ax	Shear			2.01	524	531	12.33	1.47	.45	0.00	1.77	15	3.96	.575	4.18 (127% M.I.)	72.0	66.1	96.32
	100	109		4 Hole Swirler				521	526	16.19	1.59	.44	.28	1.76	15	3.98	.625	4.35 (113% M.I.)	87.7	81.2	99.73
◇	101	108		2 Hole Swirler				524	529	19.10	1.70	.44	.59	1.76	15	3.97	.625	4.31 (112% M.I.)	91.6	86.8	99.89
◇	102	110		Increased Shear			2.87	520	525	17.14	2.16	0.32	0.00	1.25	15	3.90	.417	3.94	86.1	79.4	99.41
*	103	111		Shear		50	0.99	483	519	7.03	5.56	1.03	0.00	3.93	7	3.82	.658	4.41	74.0	67.7	96.12
*	104	112						481	518 (511)	7.30	5.83	1.02	0.00	3.92	3	3.84	.633	5A9	49.5	49.0	85.98
*	105	113						395.5	425.5 (419)	7.05	5.21	1.00	0.00	3.89	3	3.87	.726	4.96	50.9	57.7	87.25
*	106	116		3 Hole Swirler				479	515	25.20	8.13	1.01		3.90	7	3.85	.750	(79% M.I.) 4.10	94.3	90.0	99.78

FIG 9
SHT 8 OF 11

SHT 8 OF 11

	TEST	RUN	ELEM	VAR	F/E	A_t/A_o	T_o	T_f	ΔP_{oJ}	ΔP_{fJ}	$w_o V_e / w_f V_o$	$\frac{\text{NORM}}{A_t, \text{mm}}$	V_e/V_o	L/D	O/F	$\bar{R}$	$(O/F)_s$	E_m	η_m	$\%C^*$
◇	107	115	Co-Ax	3 HOLE SWIRLER	50	0.99	479	515 (508)	26.43	8.03	0.98		3.83	3	3.92	.750	5.44 (94% MASS FLOW INDICATION)	94.5	89.8	99.87
◇	108	114		↓	↓	↓	396.5	428.5 (421.5)	21.53	5.61	1.08		4.05	3	3.74	.660	6.04	93.2	87.8	99.67
	109	117		INCREASED SWIRL		1.10	480	525	11.55	8.58	0.98	0.00	3.68	7	3.77	.745	6.12	82.0	76.6	98.36
	110	118		↓		↓								3	(NO DATA AVAILABLE)					
*	111	122	TRIPLET	60° IMP.	15	0.96	500	524	11.12	4.84	0.96	0.26	3.83	3	3.98	.358	4.61	65.0	62.7	94.12
*	112	123					497	522	10.79	4.65	0.97	0.26	3.85	7	3.97	.678	3.37	82.4	72.6	98.58
*	113	124					495	522	10.87	4.78	0.96	0.26	3.84	15	3.99	.716	4.59	95.0	90.8	99.93
*	114	125					496	522	10.98	4.61	0.96	0.26	3.83	30	3.99	.375 to .700	(79% M.I.) 4.80	98.9	98.2	99.99
*	115	126					503	522	7.80	10.08	3.80	0.44	7.57	7	1.99	.631	2.34	86.2	78.4	98.84
*	116	127					487	519	13.56	2.95	0.38	0.14	2.41	7	6.42	.314	6.68	77.3	69.6	99.02
	117	128					279.1	289.9	6.46	2.70	1.14	0.29	4.15	7	3.64	.643	4.41	78.1	67.5	98.31
*																				
*	118	136		45° IMP			488	516	10.33	8.23	0.97	0.20	3.85	7	3.99	.750	(93% M.I.) 5.55	57.9	49.3	93.59
	119	134					488	513	10.40	8.70	0.98	0.20	3.87	3	3.96	~~.308~~	~~9.94~~	~~63.9~~	~~50.1~~	~~93.85~~
*																.375	(11% M.I.) 9.01	59.1	45.7	94.42
	120	135					483	514	12.90	4.90	0.37	0.11	2.40	3	6.44	~~.513~~	~~8.42~~	~~44.7~~	~~30.8~~	~~90.04~~
*																.688	(11% M.I.) 6.30	46.8	43.9	93.49
	121	133					497	515	7.39	20.23	3.81	0.32	7.57	3	1.99	~~.254~~	~~3.59~~	~~34.6~~	~~68.8~~	~~93.55~~
◇																.750	(0.2% M.I.) 2.83	63.4	50.7	90.29
*	122	129		90° IMP			495	518	9.92	10.99	0.97	0.41	~~3.84~~ 3.84	7	3.96	.439	4.30	97.6	95.9	99.92
																~~.250~~	~~4.05~~			
*	123	130					492	516	9.97	10.76	0.98	0.41	3.86	3	3.95	.307	4.49	91.7	89.8	99.03
	124	132					485	514	11.96	6.35	0.38	0.21	2.41	3	6.38	.375	8.84	73.7	70.5	99.98
◇																~~.203~~	~~11.69~~	~~89.4~~	~~88.4~~	~~99.50~~
◇	125	131					496	515	7.69	23.59	3.85	0.73	7.62	3	1.98	.350	(0.2% M.I.) 2.20	73.4	62.4	95.54
																~~.386~~	~~8.44~~	~~69.6~~	~~57.5~~	~~94.98~~

FIG. 4
SHT 9 OF 11

SHT 9 OF 11

	TEST	RUN	ELEM	VAR	F/E	A_e/A_o	T_o	T_f	ΔP_{OJ}	ΔP_{FJ}	$\dot{w}_f V_f / \dot{w}_o V_o$	$\frac{\text{Norm}}{Ax.Mm}$	V_f/V_o	L/D	O/F	$\bar{R}$	$(O/F)_s$	E_m	η_m	%C*
	126	175	TRIPLET	60°/IMP	3	1.02	515	530	10.29	6.92	0.89	0.25	3.54	15	3.98	.252	4.58	97.9	97.2	99.44
	127	176					197	(Cold Propellant Test - 2 Phase Ox)						15	4.03	(Data Not Applicable)				
226	1.01270	177					503	530	10.38	18.89	2.51	0.40	6.02	15	2.40	.316	2.98	92.2	88.4	99.55
	128	172				0.51								15		(No Data Available)				
	129	173					521	533	5.47	105.07	7.17	0.50	14.18	15	1.98	.299	2.27	97.8	97.0	99.99
	130	174					519	531	9.84	20.05	.79	.23	4.69	15	5.96	.266	6.95	93.2	90.2	99.59
*	131	121	FLAT "I" TRIPLET			2.02	519	531	38.59	27.03	0.45	0.45	1.77	15	3.98	.630	4.64	95.6	92.8	100.01
	132	168			50		486	530	35.77	27.30	0.51	.51	1.97	3	3.83	.486	4.73	88.9	83.5	99.43
	133	167					492	525	54.41	51.94	1.95	1.95	3.79	3	1.94	.381	2.68	89.2	85.2	99.46
	134	169					485	530	27.66	16.67	.23	.23	1.81	3	5.77	.720	6.50	84.0	74.8	99.00
*	135	119	FLAT "I" TRIPLET - 34%		3	2.02	529	534	40.52	32.67	0.46	0.46	1.78	15	3.90	.278	4.32	98.9	98.2	99.97
*	136	120	PENTAD	34%			520	531	47.30	36.57	0.44	0.44	1.76	15	3.99	.249	4.73	99.1	98.4	100.04
	137	170			50	0.51	489	530	35.30	60.77	2.02	2.02	7.74	3	3.84	.682	5.36	90.0	85.7	98.52
(138 Missing)																				
	139	214	TRIPLET	45°/IMP		0.50	483	507	10.60	22.91	2.03	.27	7.73	4.9	3.81	.621	4.81	91.0	86.1	99.80
	140	204		60°/IMP			479	512	9.03					3	3.83	.240	3.88	83.4	81.1 ~	97.06
	240	205					482	512	9.02	25.05	2.03	.37	7.78	7	3.84	.594	4.64	96.2	93.0	99.87
	340	206					479	512	8.97	24.50	2.01	.37	7.77	4.9	3.86	.435	4.49	90.8	85.7	99.21
	141	218		90°/IMP			481	530	7.37	38.07	4.99	.78	12.44	4.9	2.49	.393	3.48	83.8	76.2	97.87
	142	210					484	530	9.56	22.40	2.13	.60	8.10	4.9	3.80	.427	5.22	84.0	75.9	97.70
	143	212					477	530	9.90	14.66	1.34	.49	6.46	4.9	4.83	.441	6.96	85.2	77.3	98.37

FIG. 9
SHT 10 OF 11

SHT 10 OF 11

	TEST	RUN	ELEM	VAR	F/E	A_t/A_o	T_o	T_f	ΔP_{OJ}	ΔP_{FJ}	$\dot{\omega}_s V_s/\dot{\omega}_o V_o$	$\frac{\text{Norm}}{\text{Ax. Mom}}$	V_f/V_o	L/D	O/F	$\bar{R}$	$(O/F)_s$	E_m	η_m	% C^*
(145)	144	213	TRIPLET	60°/IMP.	50	0.96	481	508	9.82	6.36	1.06	.28	4.01	4.9	3.80	.585	4.57	97.2	95.7	99.97
	146	207				2.00	486	511	9.55	3.81	.50	.17	1.92	4.9	3.86	.697	4.78	93.2	88.3	99.83
	147	208					481	509	7.93	8.45	1.33	.31	3.13	4.9	2.35	.715	3.21	92.3	86.5	98.93
	148	209					476	~~510~~ 510	10.50	1.31	.22	.092	1.28	4.9	5.83	.653	6.72	78.6	69.6	98.48
	149	178	TRIPLET	60°/IMP	3	2.00	505	530	7.67	2.10	.47	.13	1.86	15	3.93	.270	4.93	94.2	92.1	99.99
	151	223					511	523	13.23	1.04	.46	.16	1.80	7	3.95	.250	4.70	83.3	79.3	98.74
	152	222					512	526	10.55	2.69	1.46	.32	3.23	7	2.21	.367	2.57	95.1	91.7	99.75
	153	221					508	521	13.64	?	.20	.086	1.20	7	5.96	.500	6.90	75.0	73.7	101.91
LOST-D	154	192	CO-AX	SHEAR	50	1.98								16.5	(NO DATA)					
	~~254~~ ~~193~~																			
*	254	193					480	513	8.96	3.09	0.49	0.00	1.93	3	3.90	.750	4.60 (85% MASS INTEGRATION)	41.2	42.0	80.01
*	354	194		($\chi\dot{\omega}_{Ro}$)			481	514	9.23	3.39	0.60	0.00	1.95	3	3.86	.750	4.84 (78% MASS INTEGRATION)	49.1	47.7	83.14
	454	195		($O\,\dot{\omega}_{Ro}$)			482	513	9.22	3.29	.51	0.00	1.95	3	3.84	~~.362~~ .375	~~4.32~~ 3.77 (LOST % M.I.)	~~43.8~~ 41.8	~~43.1~~ 49.6	~~81.04~~ 77.62
*	155	196					483	512	7.07	5.02	1.23	0.00	3.03	3	2.46	.750	3.21 (27% MASS INTEGRATION)	42.9	40.8	81.10
*	156	197					479	512	9.70	1.81	.22	0.00	1.29	3	5.83	.750	5.55 (99% MASS INTEGRATION)	47.8	44.5	83.41
*	157	199		3 HOLE SWIRLER			482	510	23.74	2.85	.51	.56	1.94	3	3.84	.576	4.49	94.9	91.5	99.81
*	158	198					491	512	18.36	4.71	1.14	.37	2.89	3	2.54	.750	1.85 (81% MASS INTEGRATION)	39.1	39.4	85.53
*	159	200					481	511	25.61	1.29	.22	.73	1.29	3	5.78	.750	7.11 (77% MASS INTEGRATION)	94.1	89.8	99.96

Sheet 11 of 11

	TEST	RUN	ELEM VAR		F/E	A_t/A_0	T_0	T_f	ΔP_{0J}	ΔP_{tJ}	w_{tk}/w_{t0}	$\frac{\text{NORM}}{A_x M_{mm}}$	V_t/V_0	L/D	O/F	$\bar{R}$	$(O/F)_S$	E_m	η_m	% C^*
*	160	201	C_0-A_x	INCREASED SHEAR	50	2.12	490	510	6.10	4.46	0.94	0.00	2.53	3	2.70	.750	3.91 (90% MASS INTEGRATION)	56.8	49.9	87.99
*	260	202					482	510	9.63	5.20	0.46	0.00	1.78	3	3.90	.500 .750 T_0	6.27 (91% MASS INTEGRATION)	48.7	45.8	86.44
*	360	203					483	510	8.29	1.59	0.23	0.00	1.27	3	5.44	.750	8.82 (99% MASS INTEGRATION)	44.5	45.3	85.31
	161	179	FLAT "I" TRIPLET	33%	15	0.99	510	530	40.32	37.51	.94	.94	3.70	3	3.93	~~.750~~ .500	~~4.54~~ (95% MI)	93.3	90.0	100.54
	162	180					506	530	36.71	34.38	.93	.93	3.70	7	3.96	.750	4.28	93.8	88.8	100.09
	163	181					507	530	36.66	34.26	.93	.93	3.70	15	3.96	.250	3.82	94.9	90.6	99.78
	164	182					509	530	36.52	33.91	.93	.93	3.68	30	3.96	.750	5.04 (99% MI)	95.3	91.1	99.81
	165	183					515	530	56.37	68.35	3.70	3.76	7.30	7	1.97	.749	2.26	92.4	86.5	99.64
	965	184					510	530	56.95	69.27	3.68	3.68	3.68	3	1.99	.750	1.99 (93% MI)	88.8	83.5	95.43
	166	185					496	530	32.77	25.28	.36	.36	2.33	3	6.44	.250	6.13 (95% MI)	96.6	93.2	99.34
(167)	168	191	PENTAD	33%			502	530	38.94	36.09	.94	.94	3.73	30	3.96	.750	5.70 (93% MI)	94.0 (98.5)	89.9	99.78
																	(LOWER LIMIT; ONLY 3 WIDE O/F POINTS AVG'D; $P_0 \neq 0$)			
	169	189					501	530	39.24	36.28	.94	.94	3.73	7	3.97	.625	4.77 (95% MI)	93.0	91.7	99.87
	170	190					502	530	38.82	35.92	.95	.95	3.74	15	3.95	.750	4.57 (95% MI)	98.1	96.6	99.99
	171	188					499	530	40.33	38.00	.95	.95	3.75	3	3.97	.595	4.21	92.3	88.3	100.30
	172	187					506	530	58.92	65.85	3.73	3.73	7.40	3	1.98	.375	1.98 (72% MI)	93.1	89.5	97.98
	173	186					506	530	32.56	26.19	.36	.36	2.31	3	6.35	.250	7.57 (93% MI)	91.3	89.5	101.35

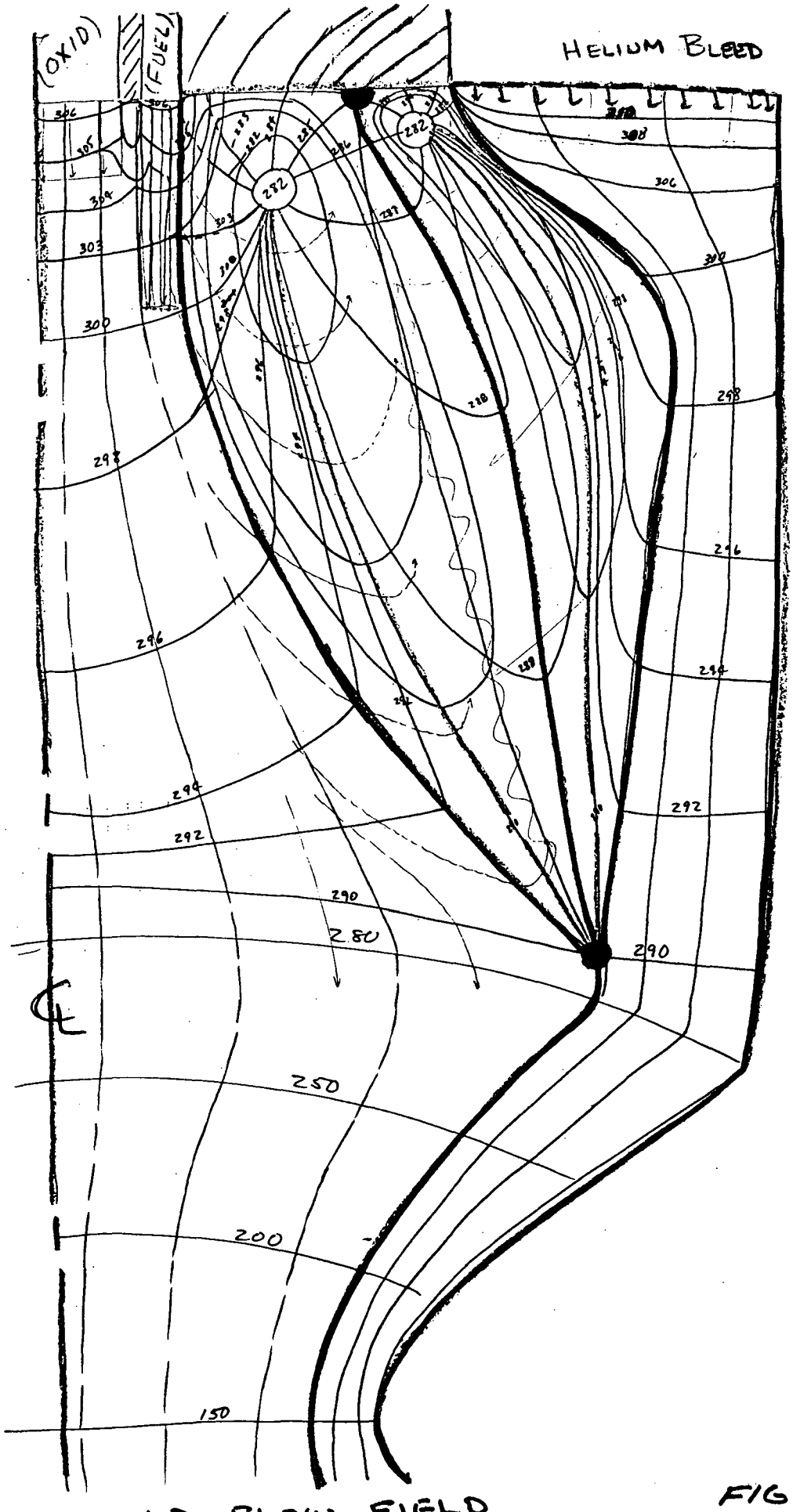

COLD FLOW FIELD

FIG 5

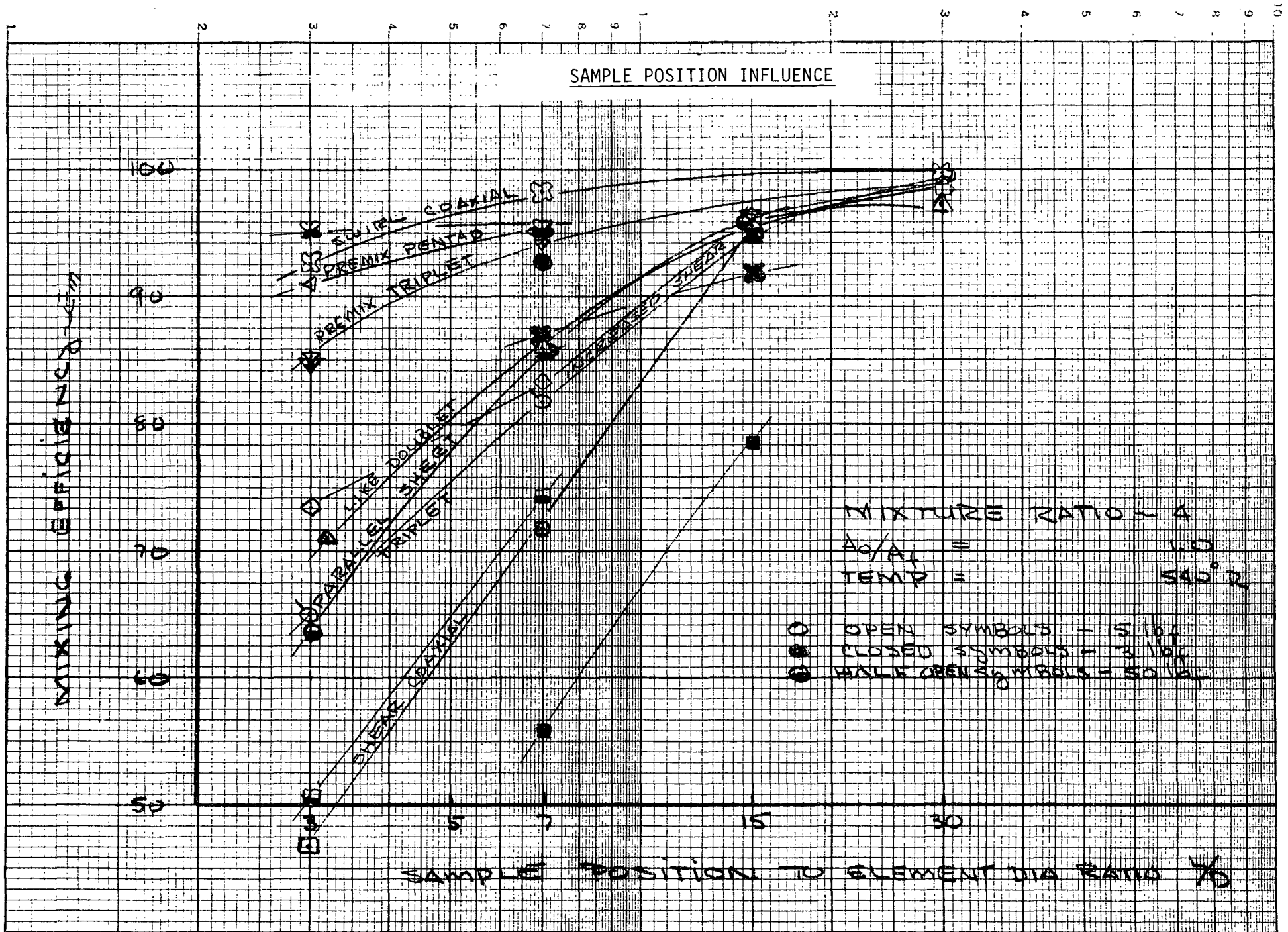

FIG 6

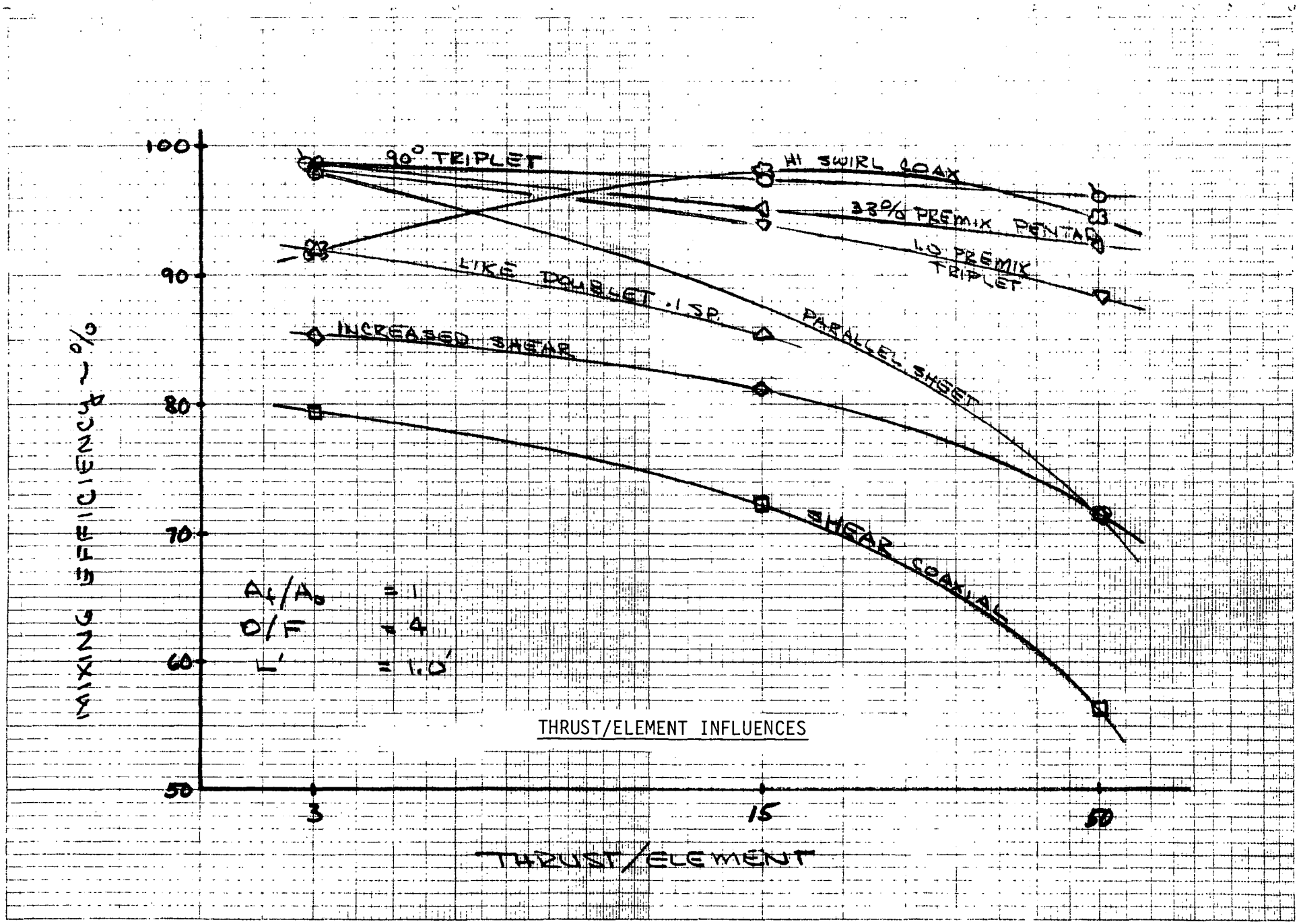

THRUST/ELEMENT INFLUENCES

FIG 7

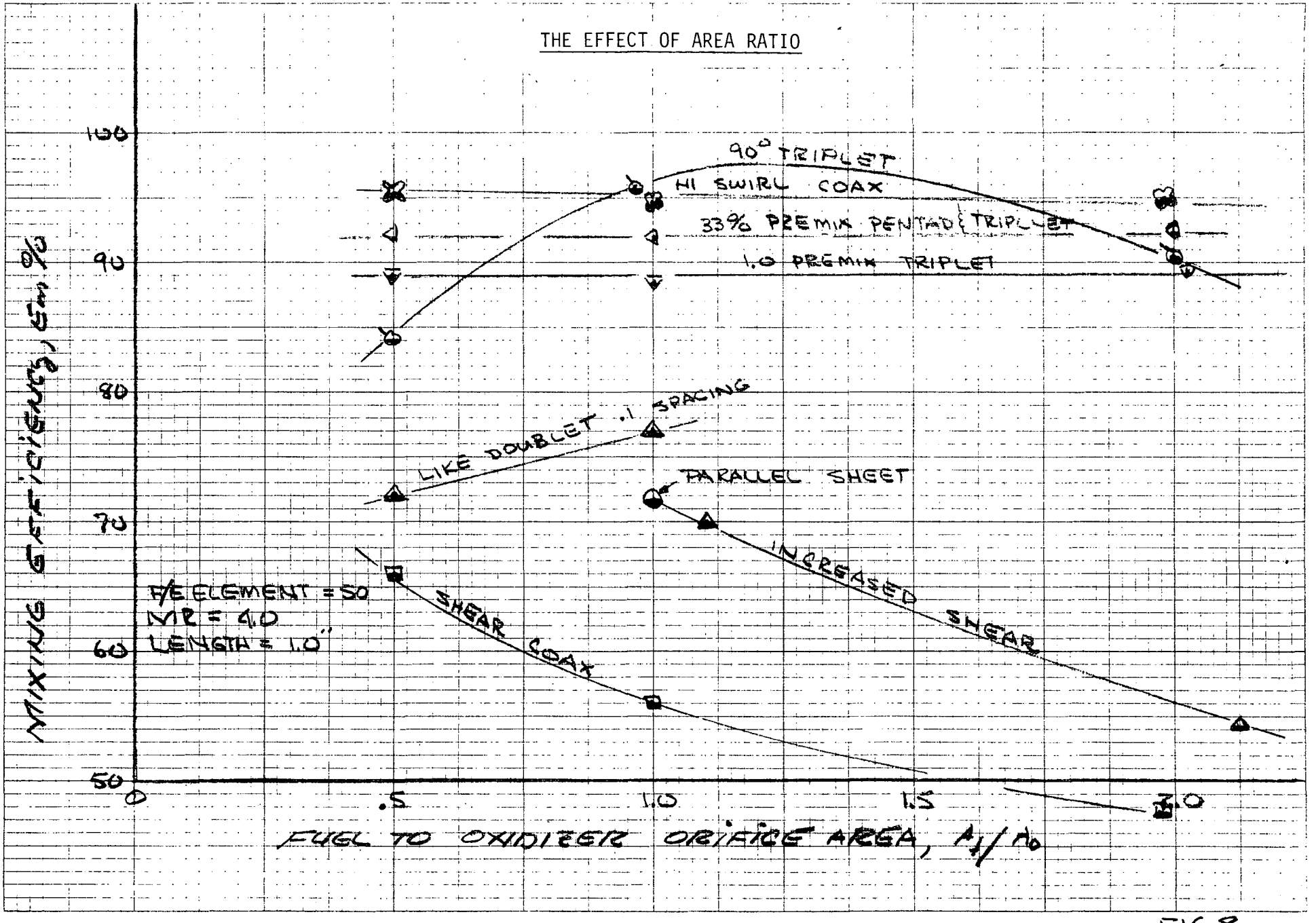

FIG.8

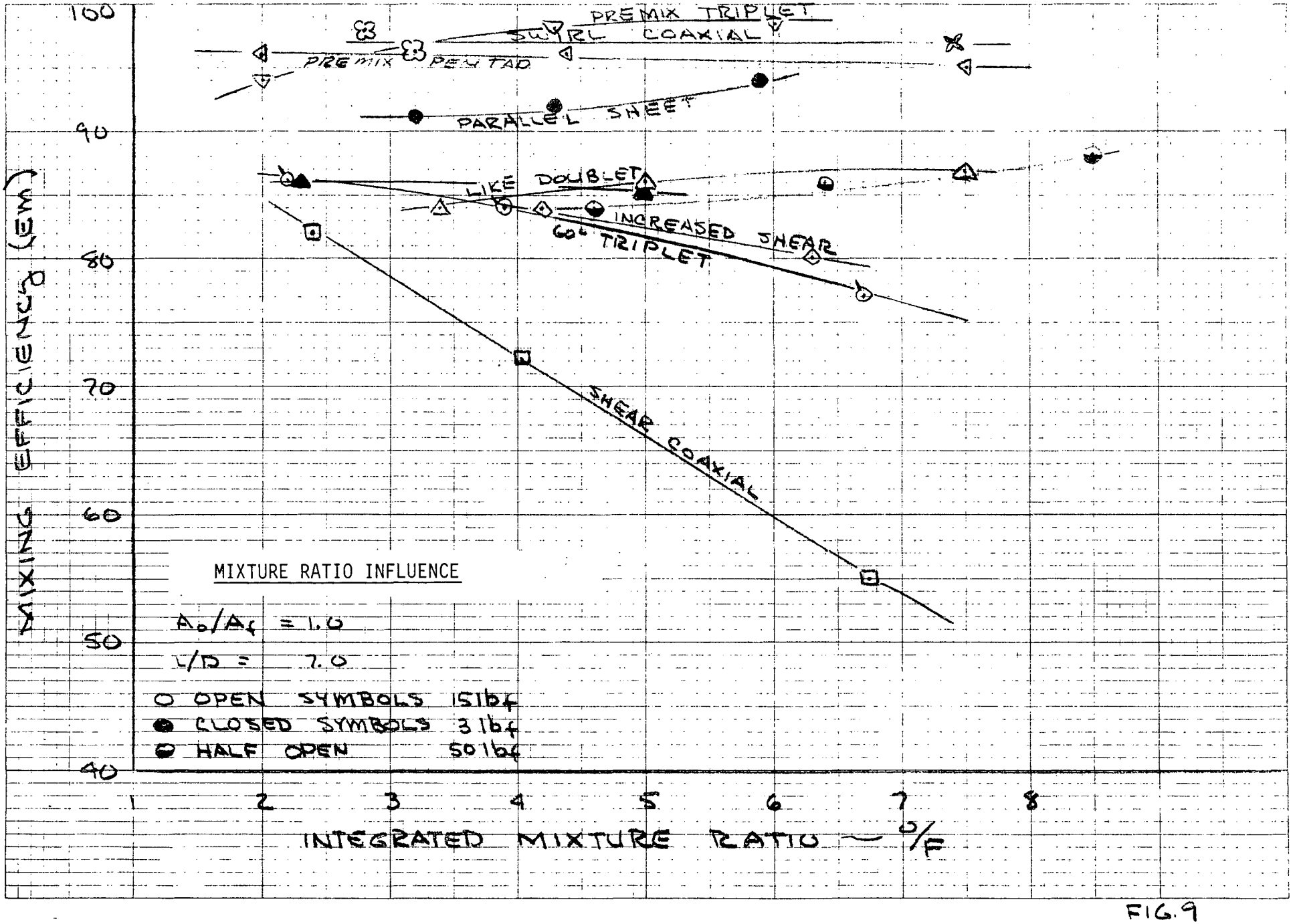
PREMIX TRIPLET
SWIRL COAXIAL
PREMIX
PENTAD
PARALLEL SHEET
LIKE DOUBLET
INCREASED SHEAR
60° TRIPLET
SHEAR COAXIAL
MIXING EFFICIENCY (EM)
100
90
80
70
60
50
40
MIXTURE RATIO INFLUENCE
A_o/A_f = 1.0
L/D = 7.0
OPEN SYMBOLS 15 lbf
CLOSED SYMBOLS 3 lbf
HALF OPEN 50 lbf
1
2
3
4
5
6
7
8
INTEGRATED MIXTURE RATIO — O/F

FIG. 9

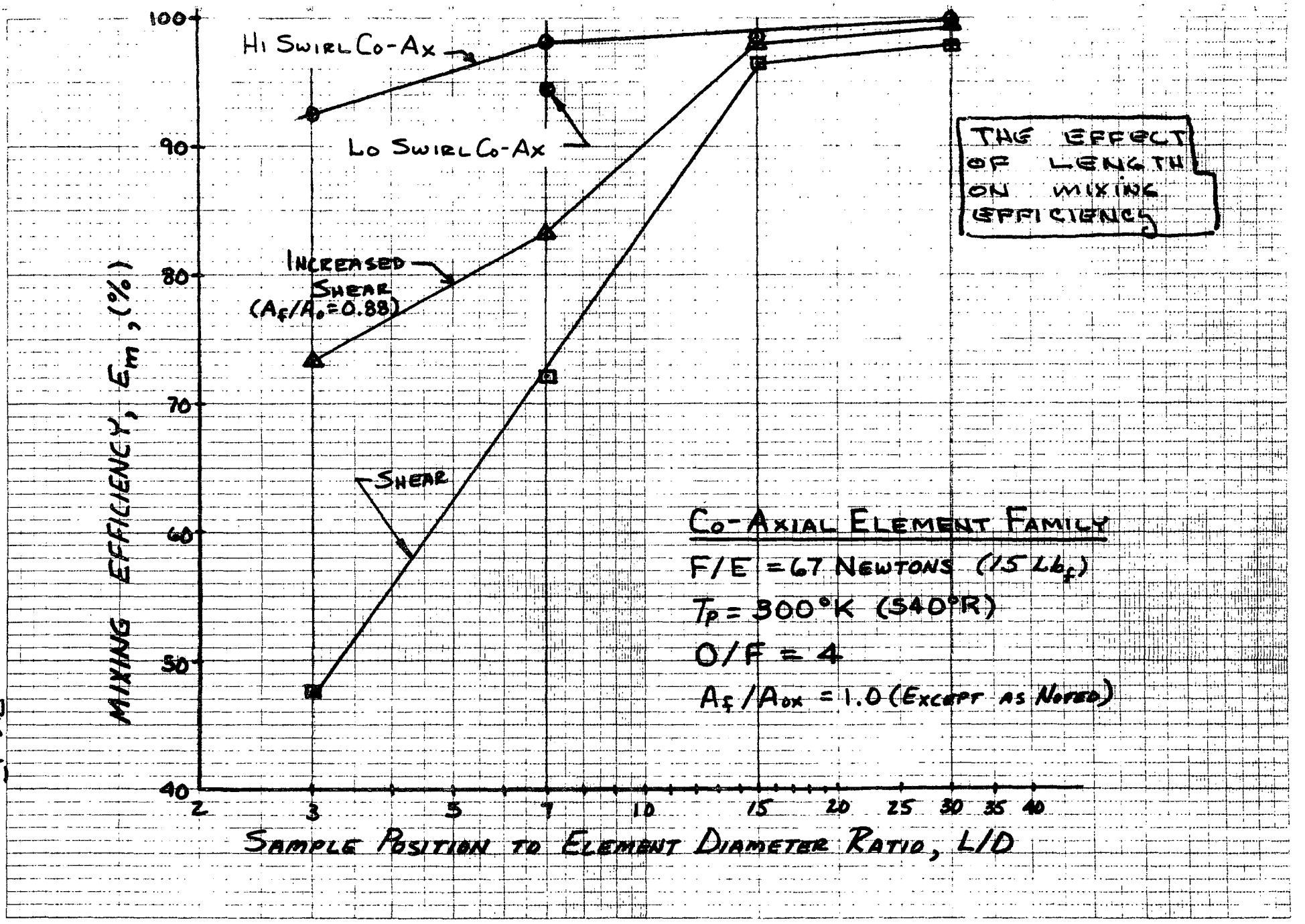
100
90
80
70
60
50
40
MIXING EFFICIENCY, E_m, (%)
HI SWIRL CO-AX
LO SWIRL CO-AX
INCREASED SHEAR (A_f/A_o=0.88)
SHEAR
THE EFFECT OF LENGTH ON MIXING EFFICIENCY
CO-AXIAL ELEMENT FAMILY
F/E = 67 NEWTONS (15 Lb_f)
T_p = 300°K (540°R)
O/F = 4
A_f/A_{ox} = 1.0 (EXCEPT AS NOTED)
2
3
5
7
10
15
20
25
30
35
40
SAMPLE POSITION TO ELEMENT DIAMETER RATIO, L/D

FIG 9

FIG 10

THE EFFECT OF MIXTURE RATIO ON MIXING EFFICIENCY

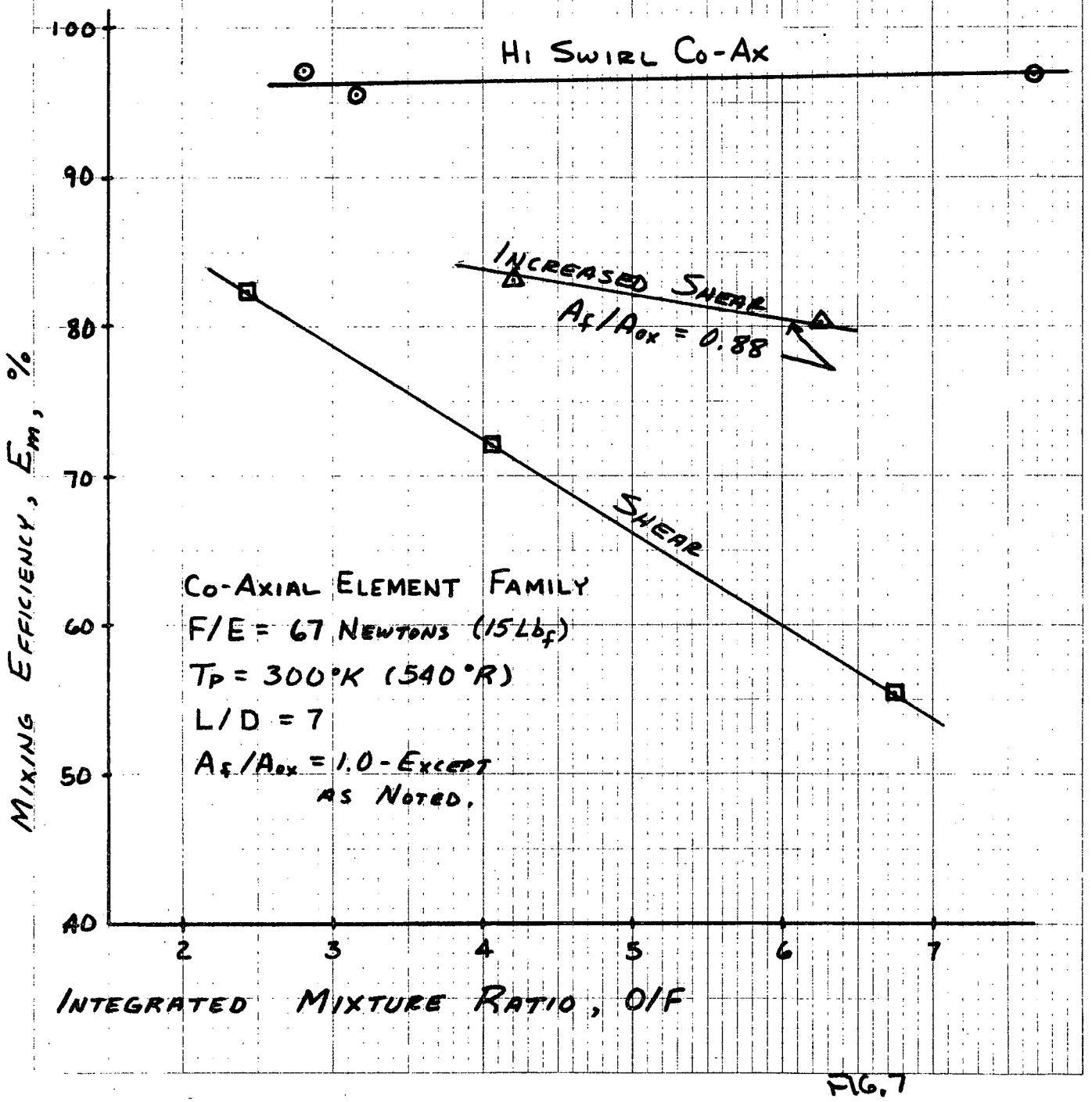

FIG. 7

COAXIAL

THE EFFECT OF A_f/A_o AS A FUNCTION OF F/E

$L' = 1$ IN, 2.54 CM
$O/F = 4$
$T_p = 540°R, 300°K$

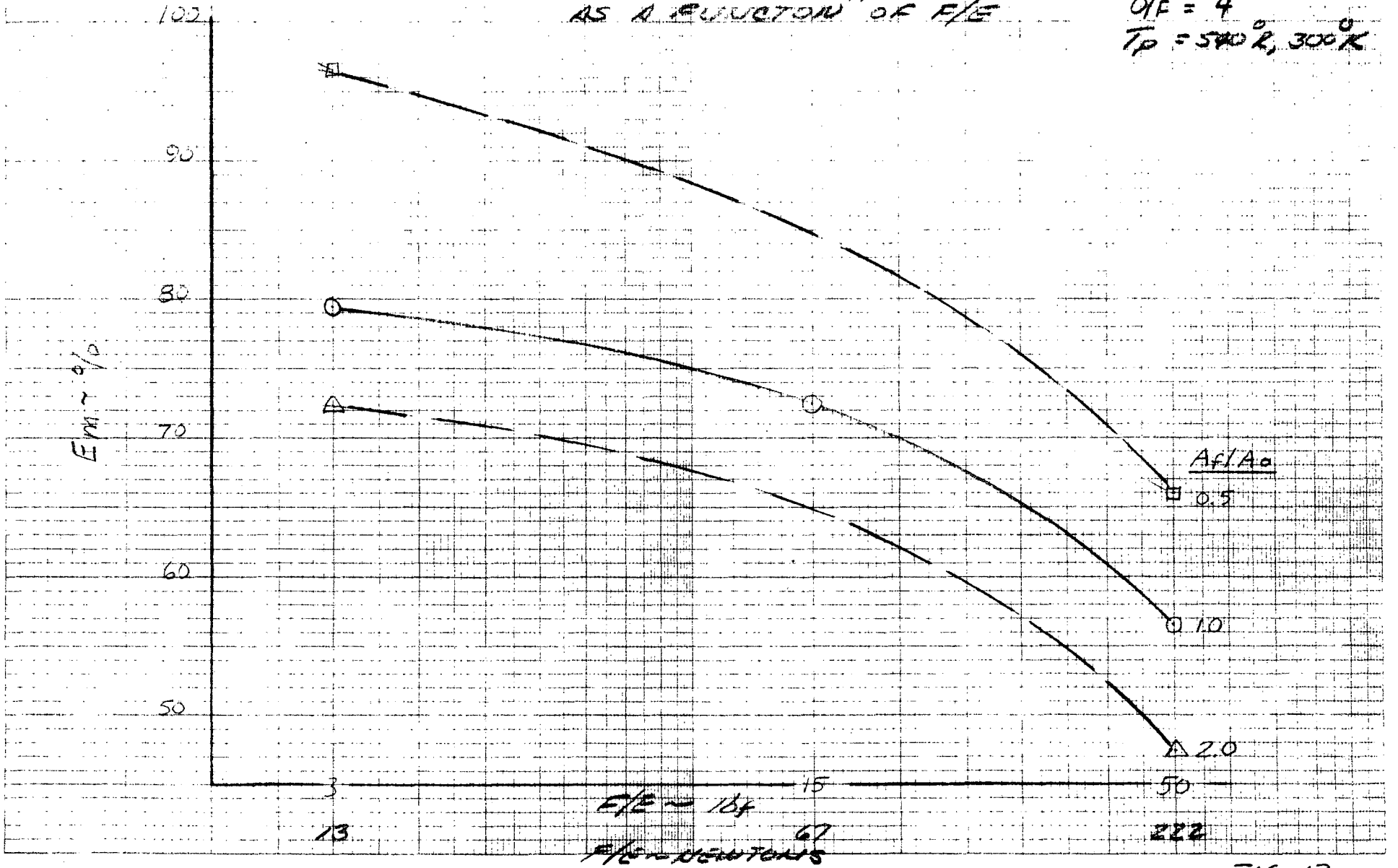

FIG. 12

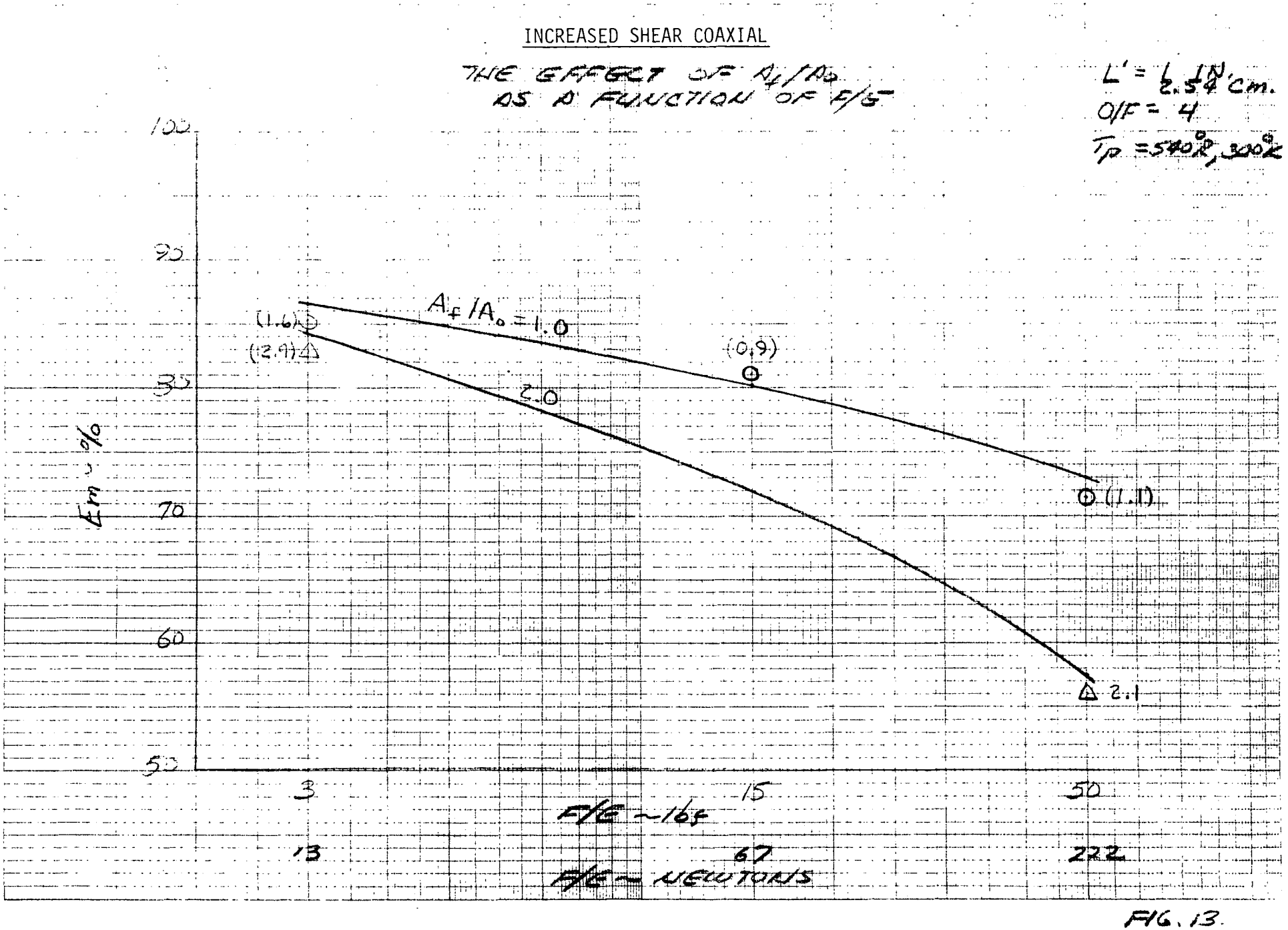
INCREASED SHEAR COAXIAL
THE EFFECT OF A_f/A_o AS A FUNCTION OF F/E
L' = 6 IN 2.54 cm.
O/F = 4
T_p = 540°R, 300°K
100
90
80
70
60
50
η_m, %
A_f/A_o = 1.0
2.0
(1.6)
(2.9)
(0.9)
(1.1)
2.1
3
15
50
F/E ~ lbf
13
67
222
F/E ~ NEWTONS

FIG. 13.

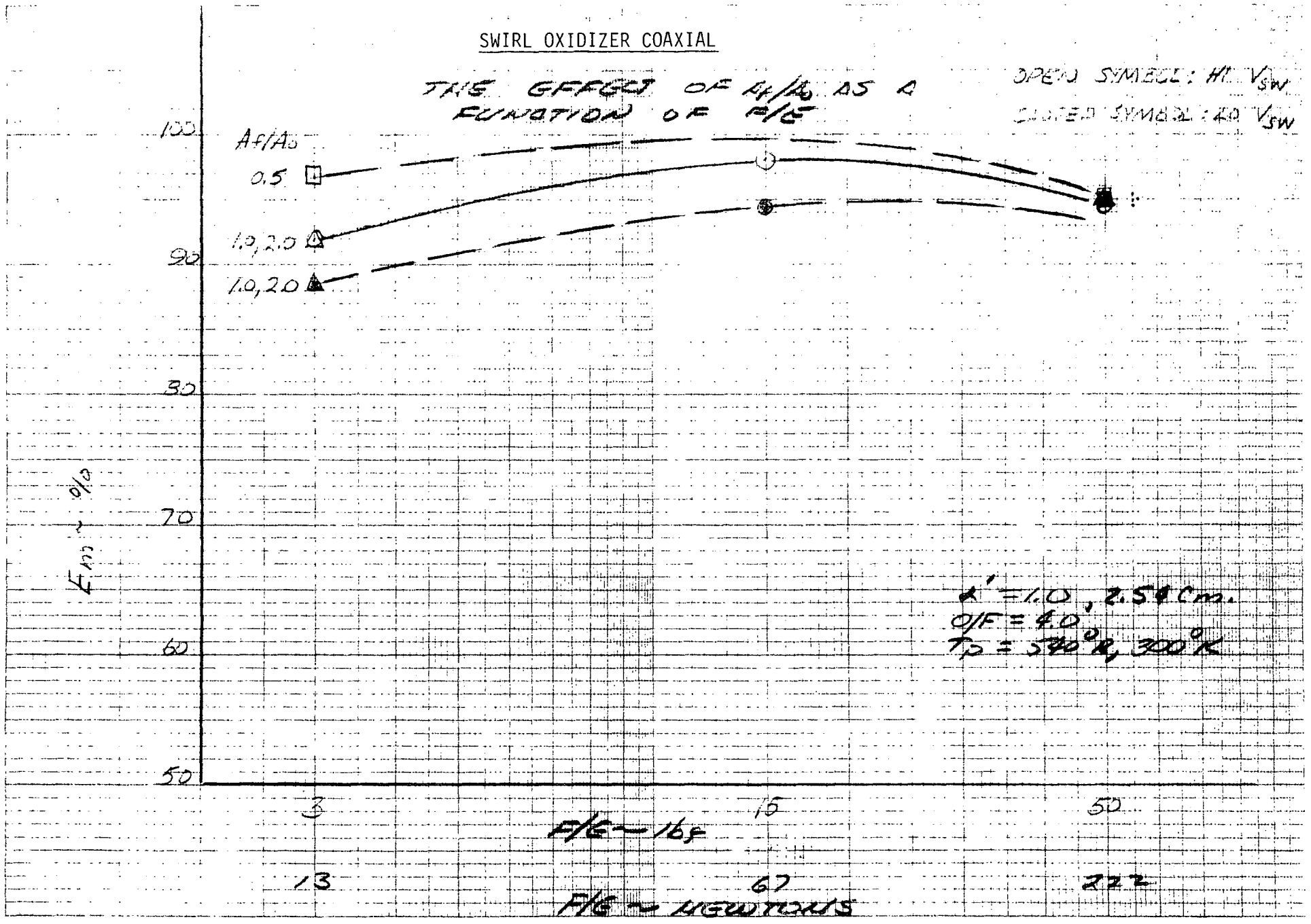
SWIRL OXIDIZER COAXIAL
THE EFFECT OF Af/Ao AS A FUNCTION OF F/C
OPEN SYMBOL: Hi Vsw
CLOSED SYMBOL: Lo Vsw
Af/Ao
0.5
1.0, 2.0
1.0, 2.0
100
90
80
70
60
50
η c*
O/F = 4.0
To = 530°R, 300°K
3
15
50
F/C — lbf
13
67
222
F/C — Newtons

FIG. 14

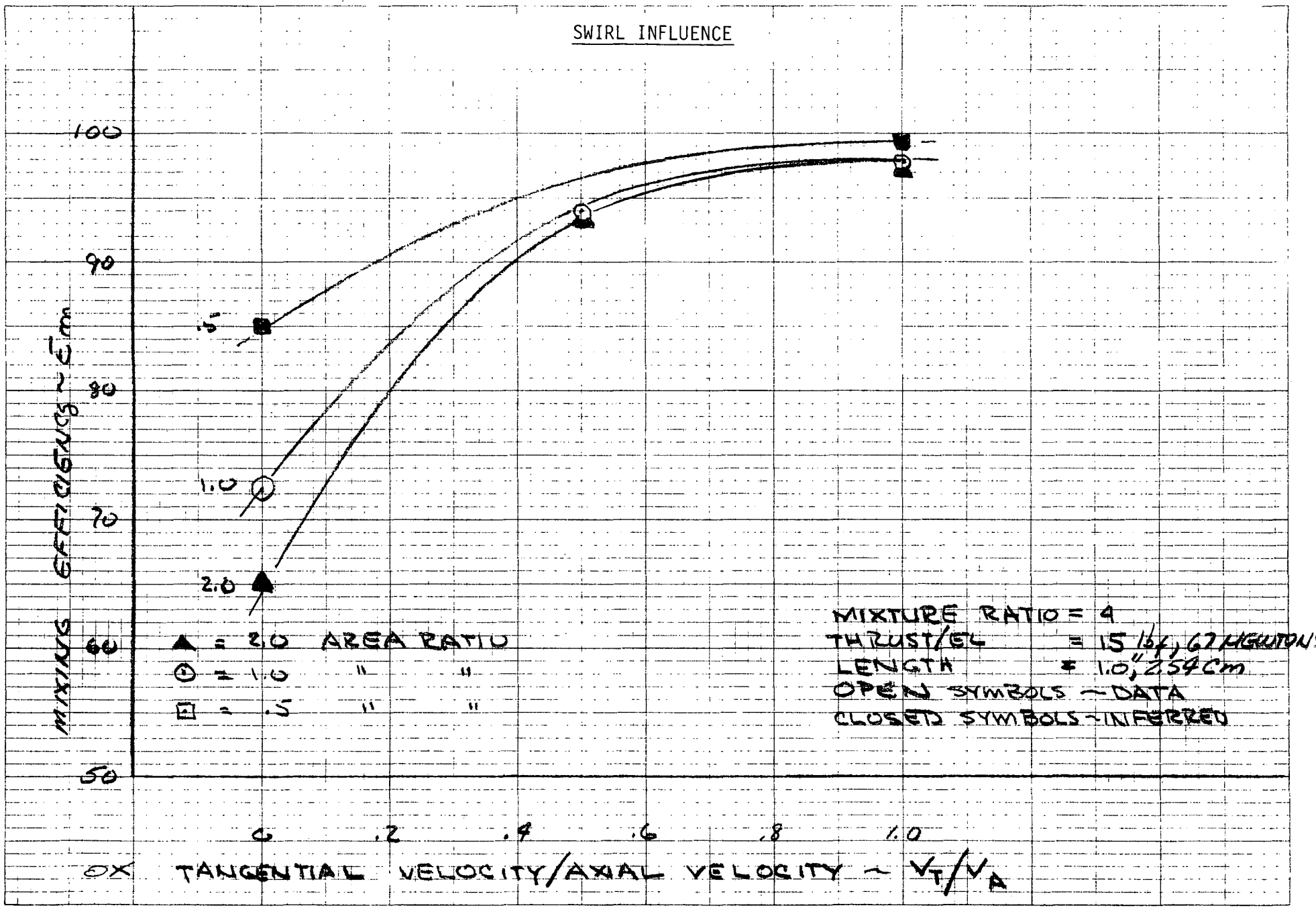
SWIRL INFLUENCE
MIXING EFFICIENCY ~ $\bar{\eta}_m$
100
90
80
70
60
50
.5
1.0
2.0
▲ = 2.0 AREA RATIO
⊙ = 1.0 " "
⊡ = .5 " "
MIXTURE RATIO = 4
THRUST/EL = 15 lbf, 67 NEWTONS
LENGTH = 1.0", 2.54 cm
OPEN SYMBOLS ~ DATA
CLOSED SYMBOLS ~ INFERRED
0
.2
.4
.6
.8
1.0
OX TANGENTIAL VELOCITY/AXIAL VELOCITY ~ V_T/V_A

FIG. 15

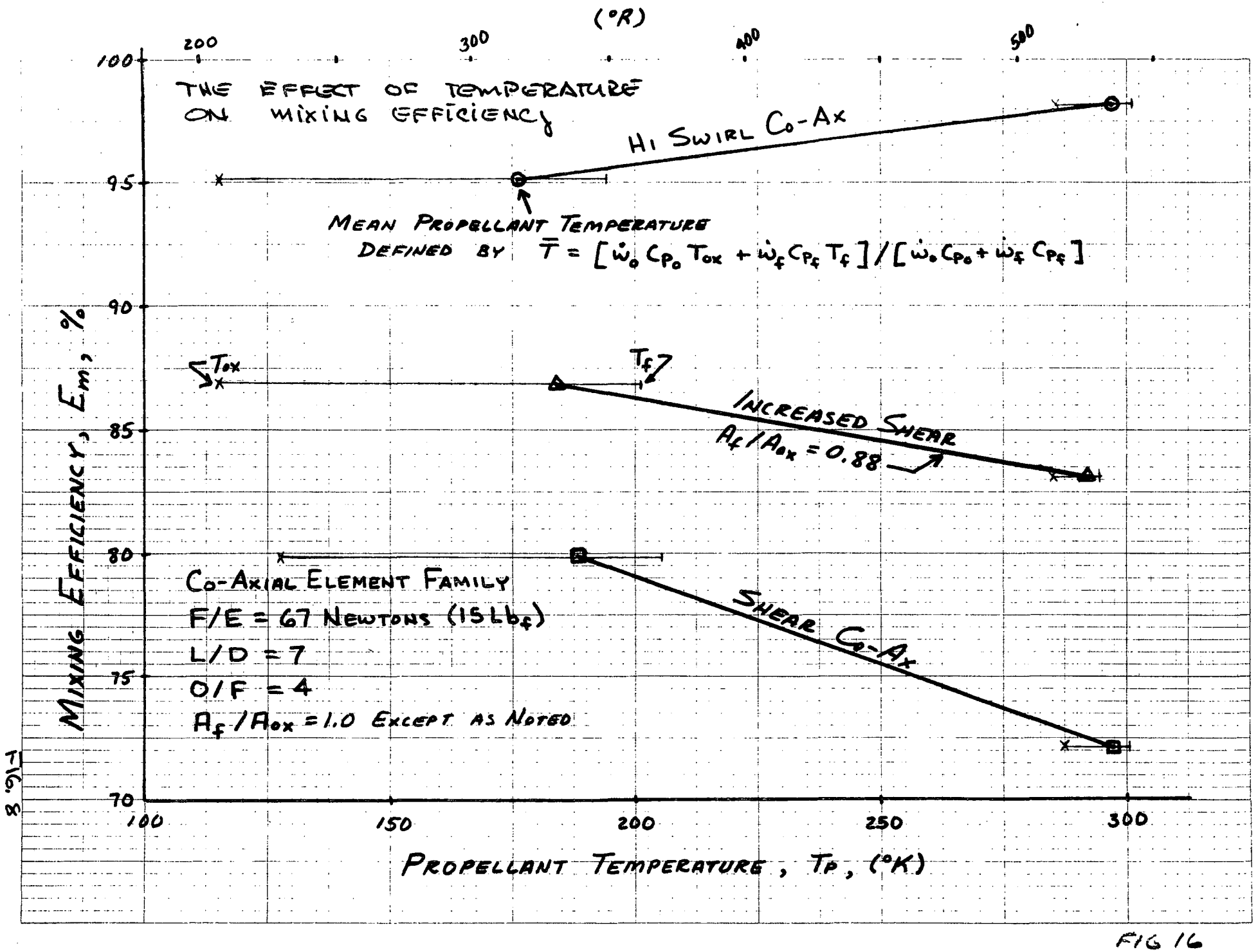
(°R)
200
300
400
500
100
95
90
85
80
75
70
THE EFFECT OF TEMPERATURE ON MIXING EFFICIENCY
HI SWIRL Co-Ax
MEAN PROPELLANT TEMPERATURE DEFINED BY $\bar{T} = [\dot{w}_o C_{p_o} T_{ox} + \dot{w}_f C_{p_f} T_f] / [\dot{w}_o C_{p_o} + \dot{w}_f C_{p_f}]$
Tox
Tf
INCREASED SHEAR
$A_f/A_{ox} = 0.88$
Co-AXIAL ELEMENT FAMILY
F/E = 67 NEWTONS (15Lbf)
L/D = 7
O/F = 4
$A_f/A_{ox} = 1.0$ EXCEPT AS NOTED
SHEAR Co-Ax
MIXING EFFICIENCY, E_m, %
100
150
200
250
300
PROPELLANT TEMPERATURE, T_P, (°K)

FIG 16

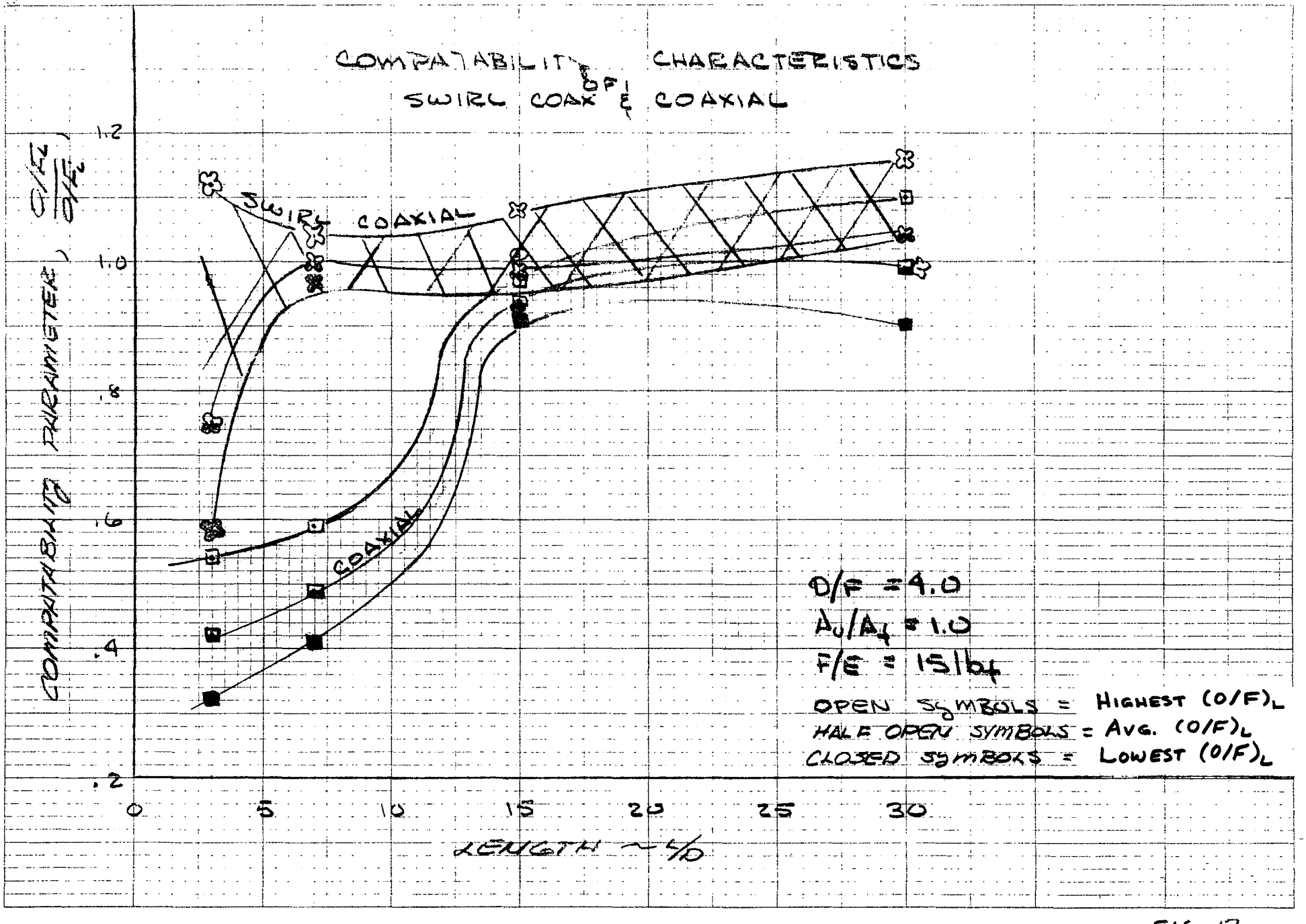

FIG. 17

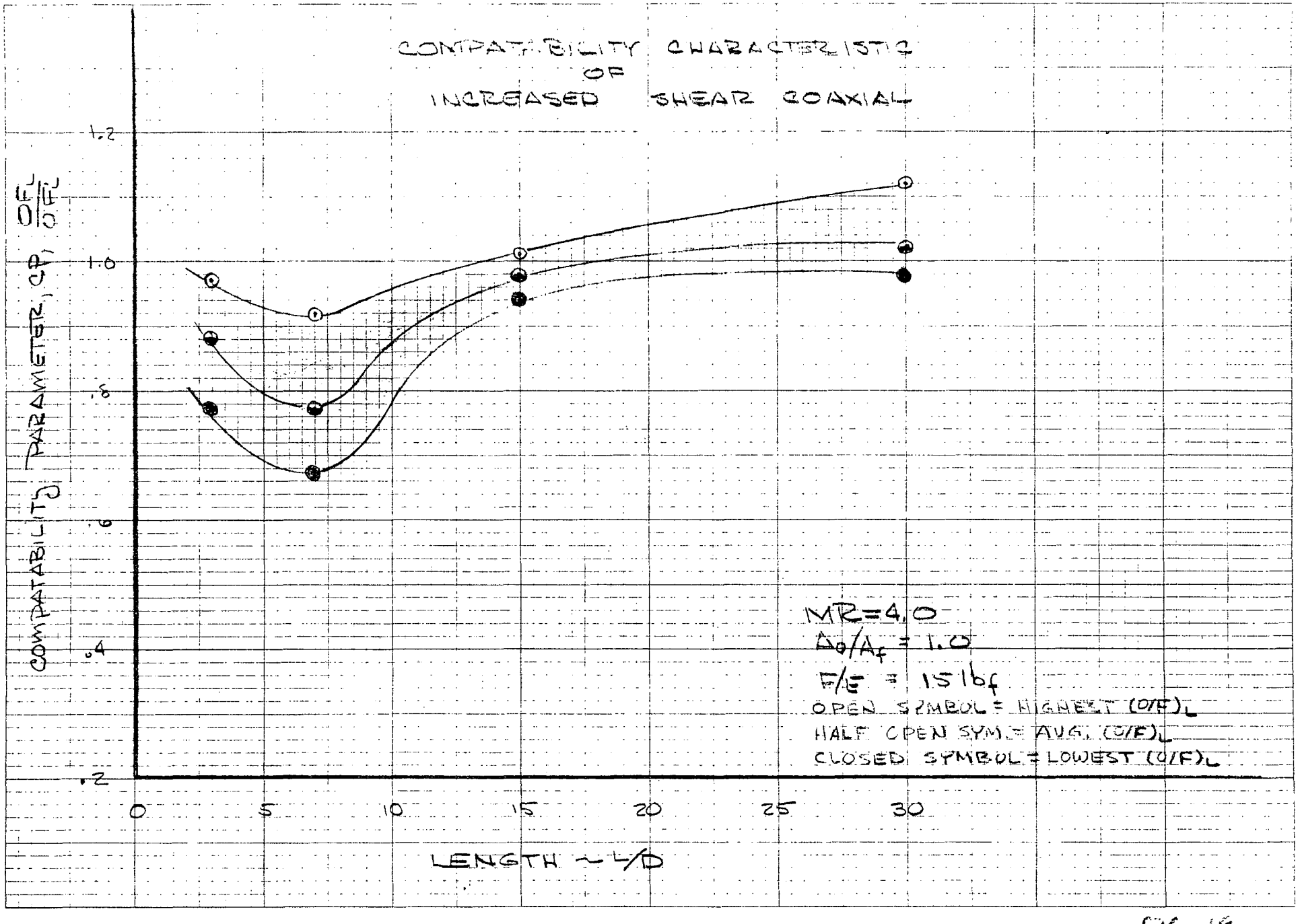

FIG. 18

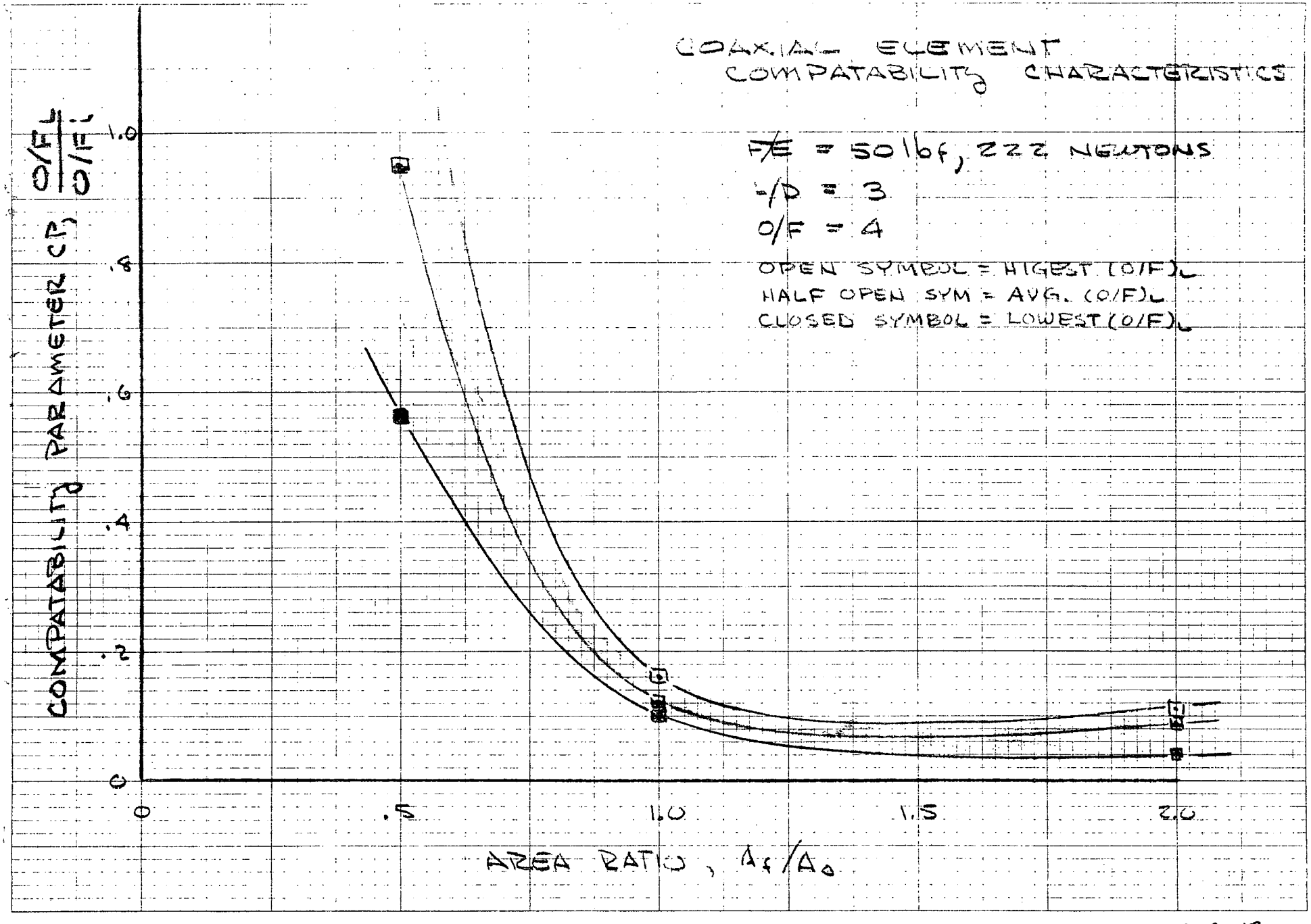
COAXIAL ELEMENT
COMPATABILITY CHARACTERISTICS
F/E = 50 lbf, 222 NEWTONS
-/D = 3
O/F = 4
OPEN SYMBOL = HIGEST (O/F)c
HALF OPEN SYM = AVG. (O/F)c
CLOSED SYMBOL = LOWEST (O/F)c
COMPATABILITY PARAMETER (CP) (O/F)c / (O/F)i
1.0
.8
.6
.4
.2
0
0
.5
1.0
1.5
2.0
AREA RATIO, Af/Ao

FIG. 19

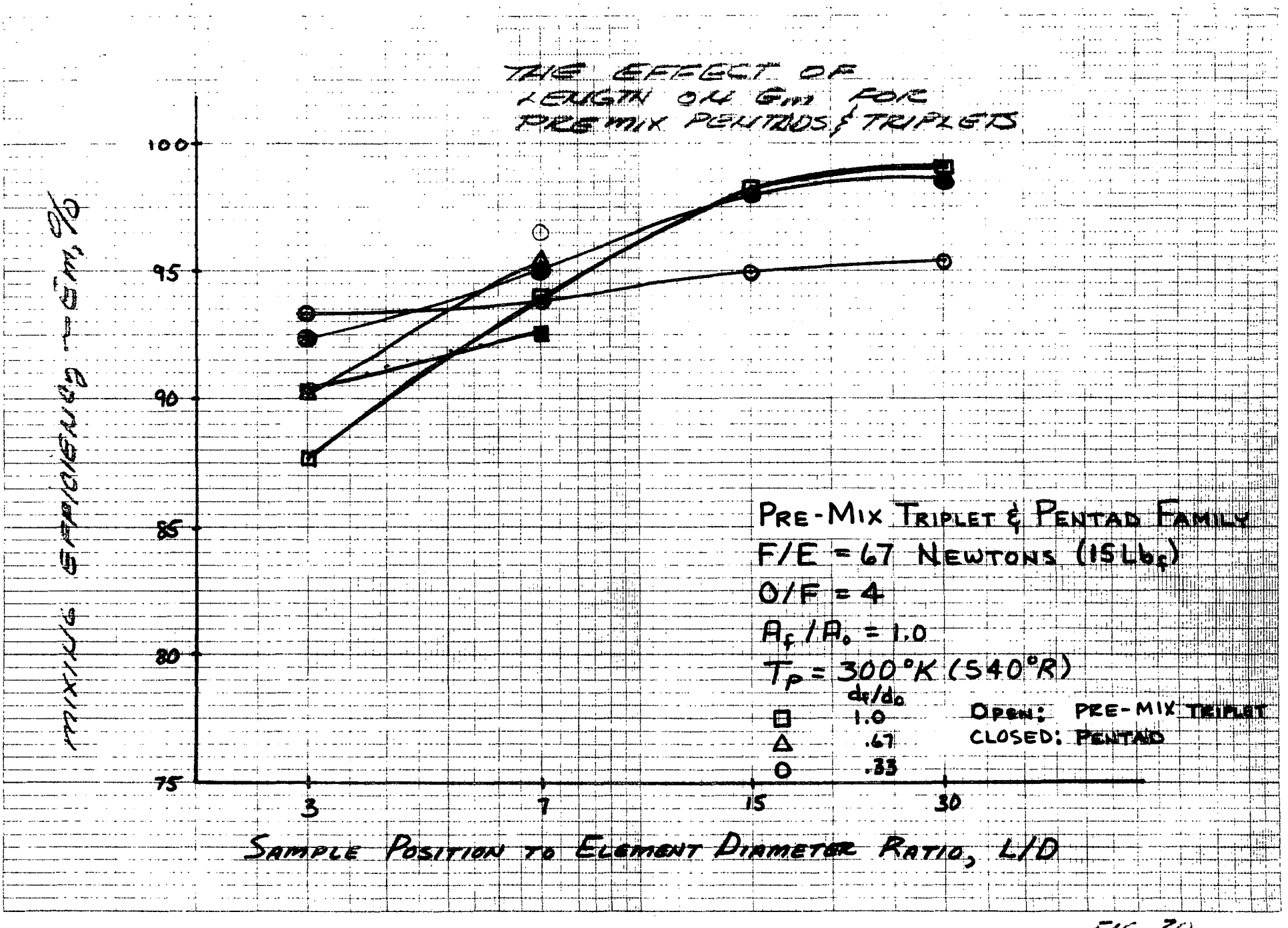
THE EFFECT OF LENGTH ON G_m FOR PRE MIX PENTADS & TRIPLETS
MIXING EFFICIENCY - G_m, %
100
95
90
85
80
75
3
7
15
30
SAMPLE POSITION TO ELEMENT DIAMETER RATIO, L/D
PRE-MIX TRIPLET & PENTAD FAMILY
F/E = 67 NEWTONS (15 Lb_f)
O/F = 4
A_f/A_o = 1.0
T_p = 300°K (540°R)
d_f/d_o
1.0
.67
.33
OPEN: PRE-MIX TRIPLET
CLOSED: PENTAD

FIG. 20

PREMIX PENTAD

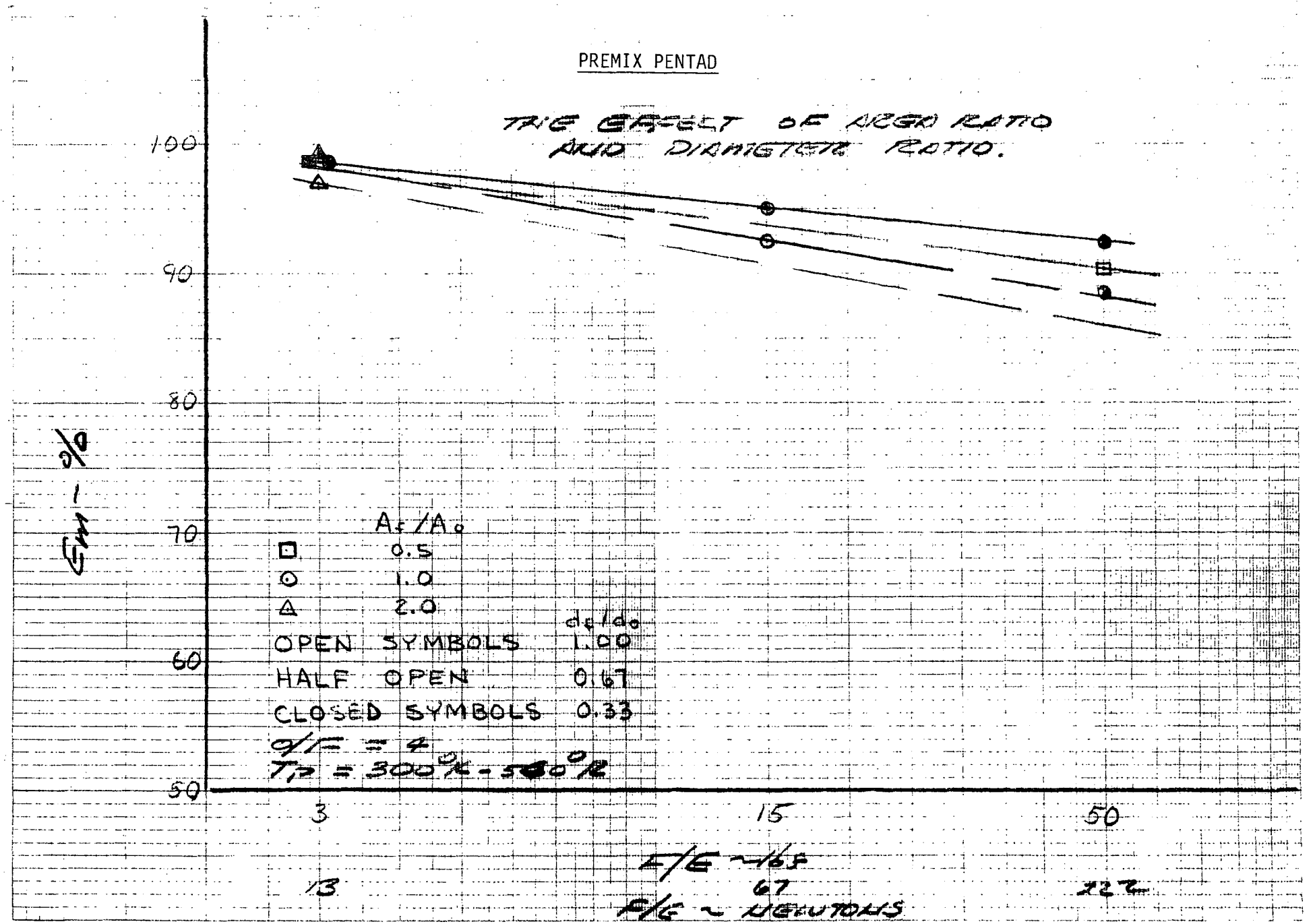

Fig. 21

PREMIX TRIPLET

THE EFFECT OF AREA RATIO AND DIAMETER RATIO

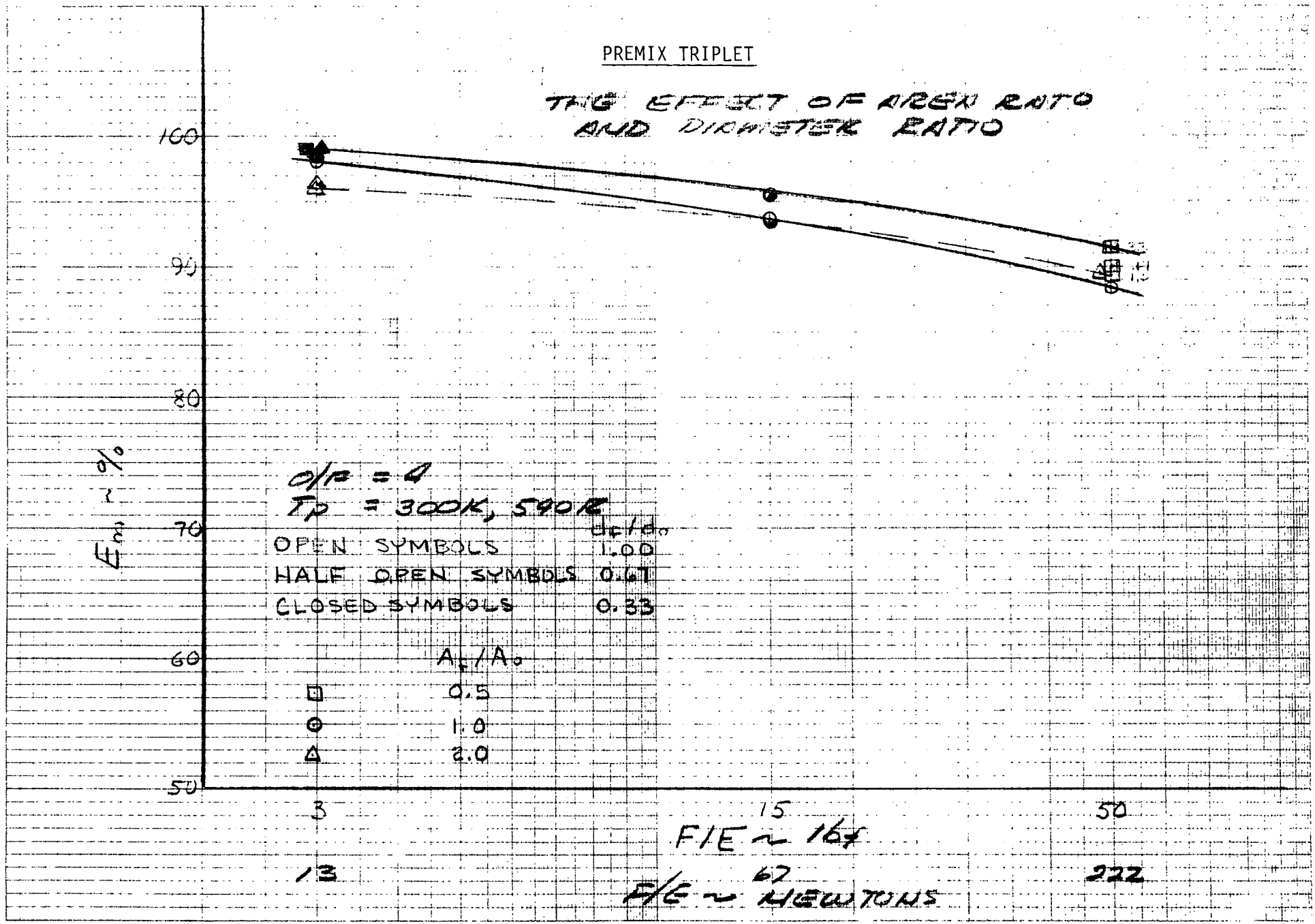

FIG 22

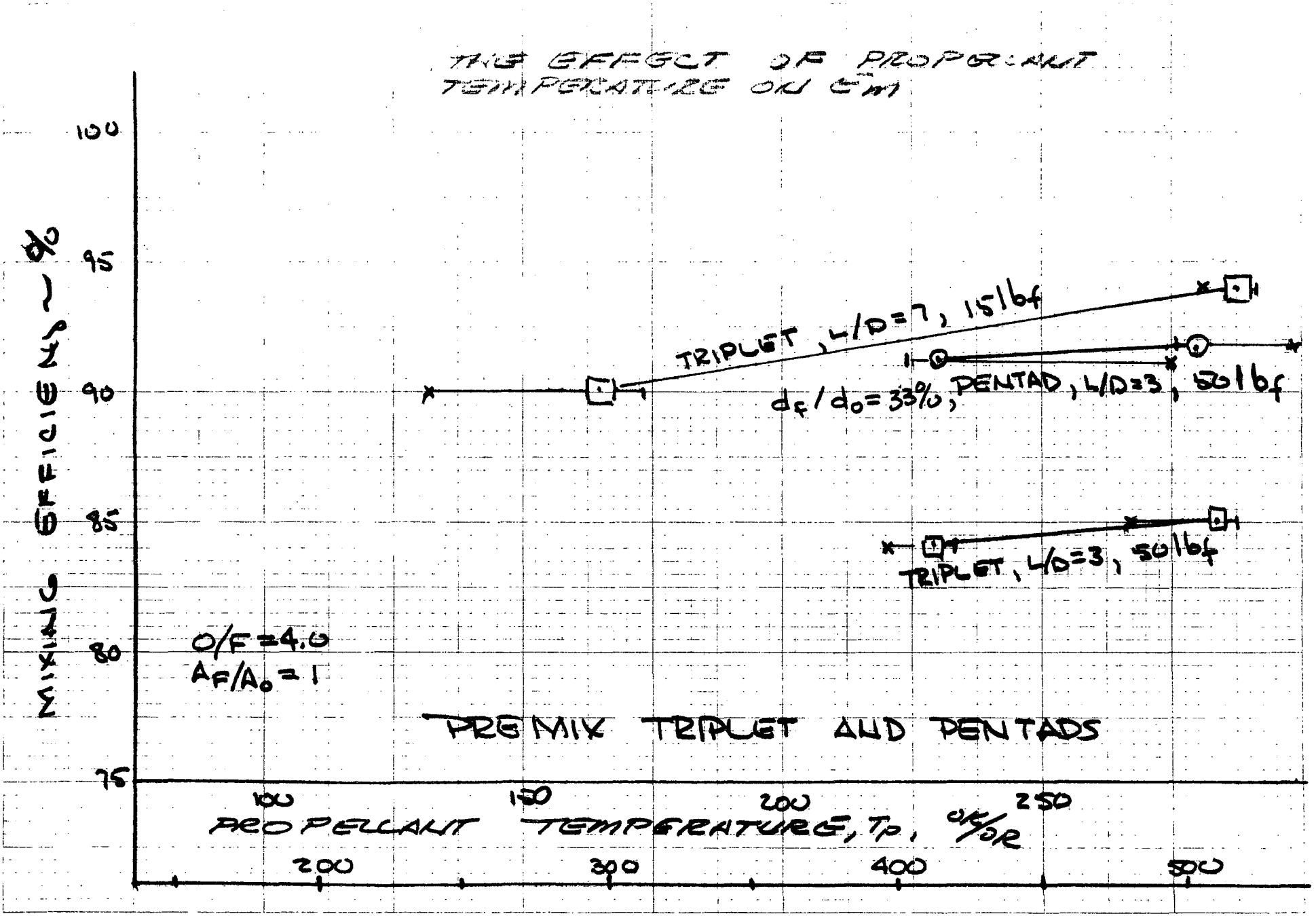
THE EFFECT OF PROPELLANT TEMPERATURE ON η_M
MIXING EFFICIENCY, η_M ~ %
100
95
90
85
80
75
TRIPLET, L/D=7, 15 lbf
d_F/d_o=33%, PENTAD, L/D=3, 50 lbf
TRIPLET, L/D=3, 50 lbf
O/F=4.0
A_F/A_o=1
PREMIX TRIPLET AND PENTADS
100
150
200
250
PROPELLANT TEMPERATURE, T_p, °F/°R
200
300
400
500

FIG. 23

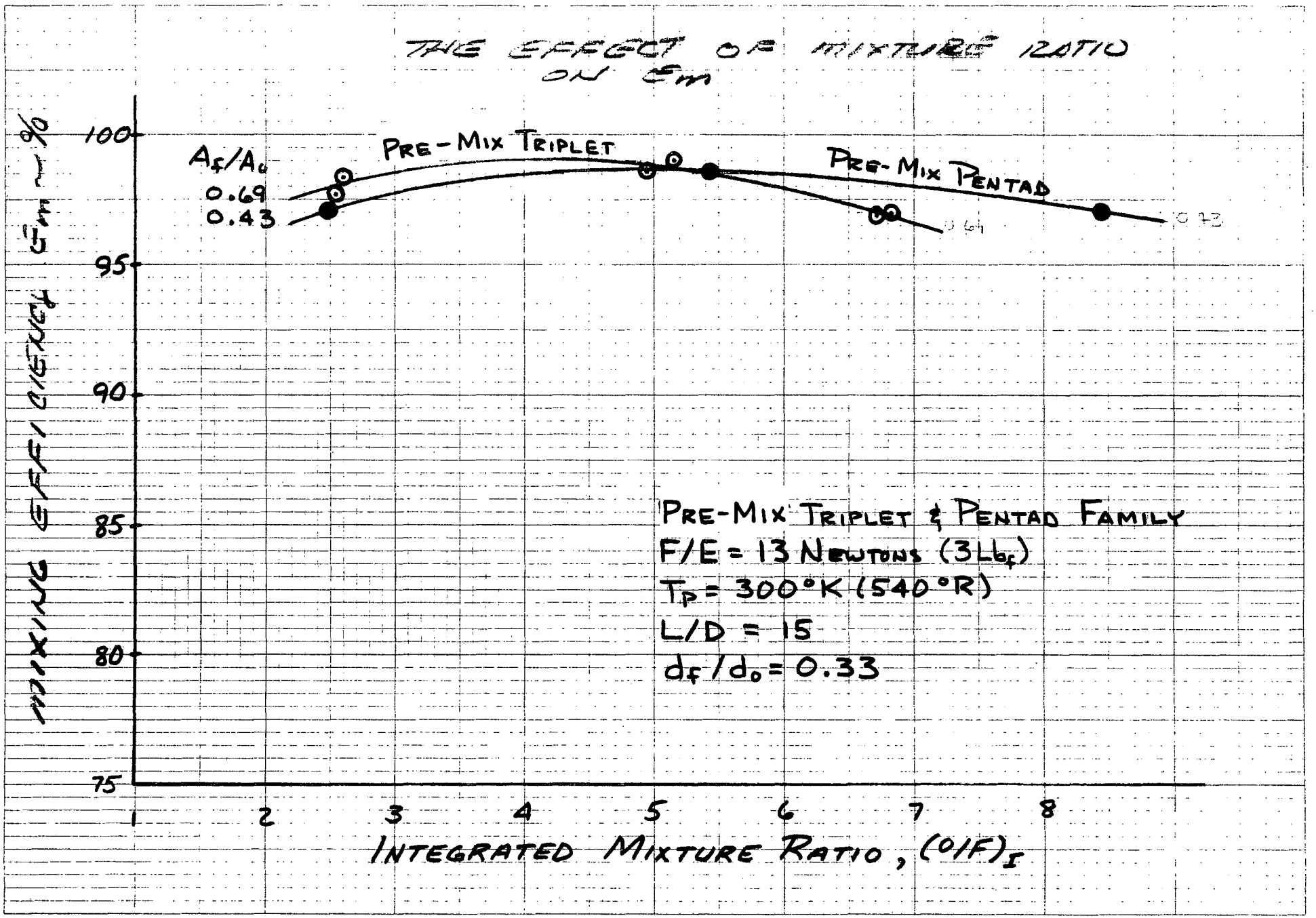

FIG 24

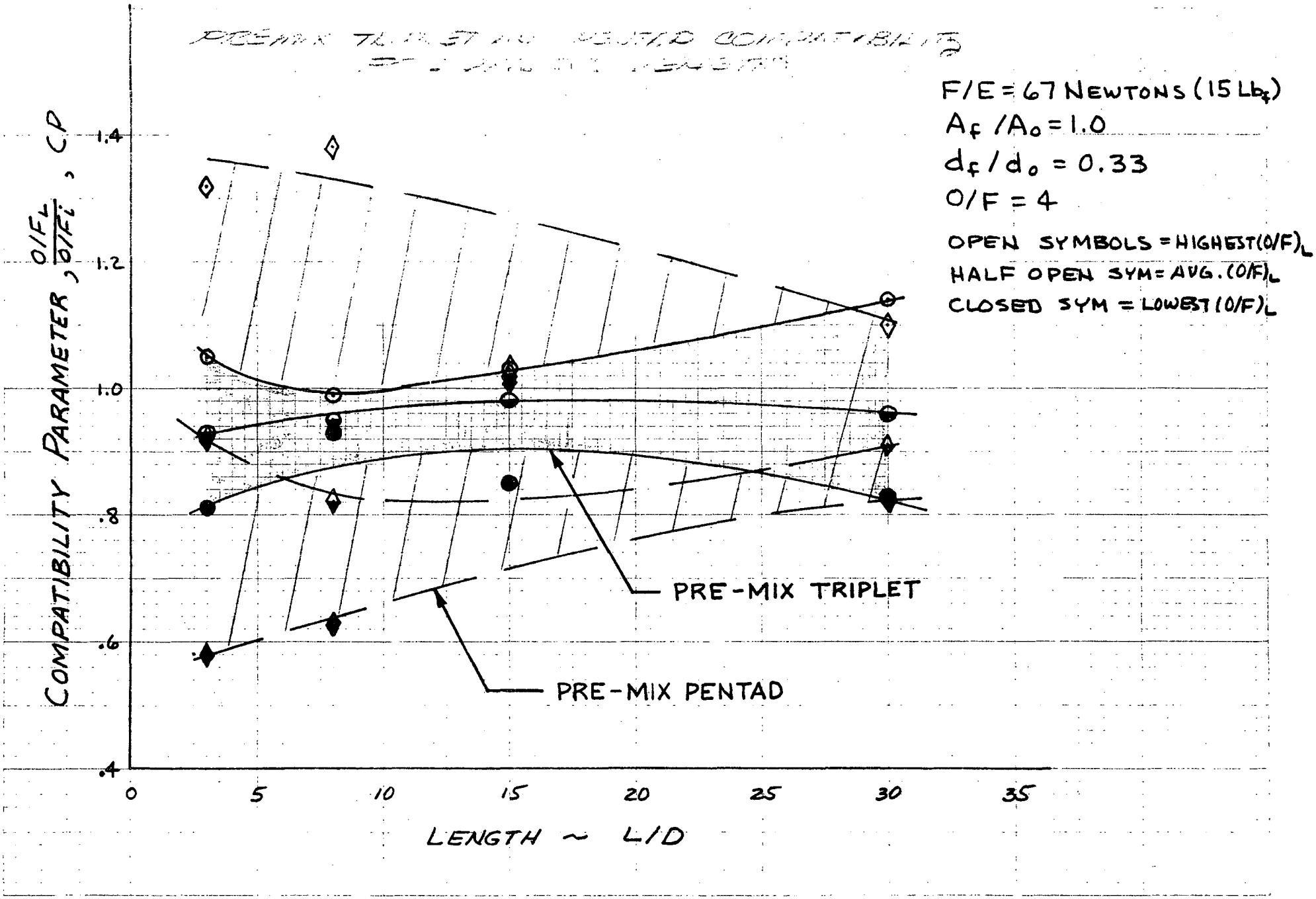
F/E = 67 NEWTONS (15 Lbf)
Af/Ao = 1.0
df/do = 0.33
O/F = 4
OPEN SYMBOLS = HIGHEST (O/F)L
HALF OPEN SYM = AVG. (O/F)L
CLOSED SYM = LOWEST (O/F)L
PRE-MIX TRIPLET
PRE-MIX PENTAD
COMPATIBILITY PARAMETER, O/FL / O/Fi , CP
LENGTH ~ L/D
1.4
1.2
1.0
.8
.6
.4
0
5
10
15
20
25
30
35

FIG 25

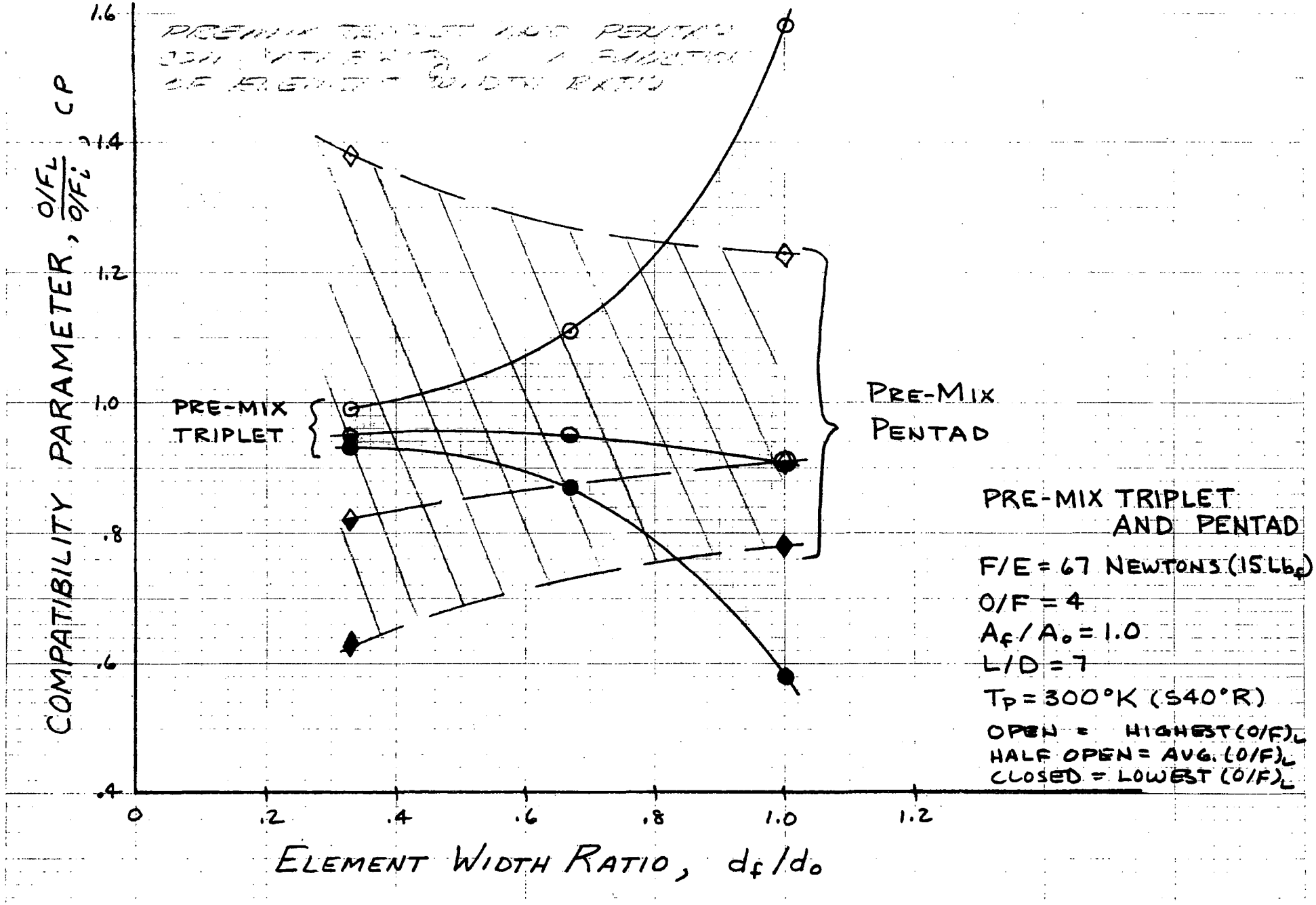
COMPATIBILITY PARAMETER, $\frac{O/F_L}{O/F_i}$, CP
1.6
1.4
1.2
1.0
.8
.6
.4
0
.2
.4
.6
.8
1.0
1.2
ELEMENT WIDTH RATIO, d_f/d_o
PRE-MIX TRIPLET
PRE-MIX PENTAD
PRE-MIX TRIPLET AND PENTAD
F/E = 67 NEWTONS (15 Lb_f)
O/F = 4
$A_f/A_o = 1.0$
L/D = 7
T_P = 300°K (540°R)
OPEN = HIGHEST $(O/F)_L$
HALF OPEN = AVG. $(O/F)_L$
CLOSED = LOWEST $(O/F)_L$

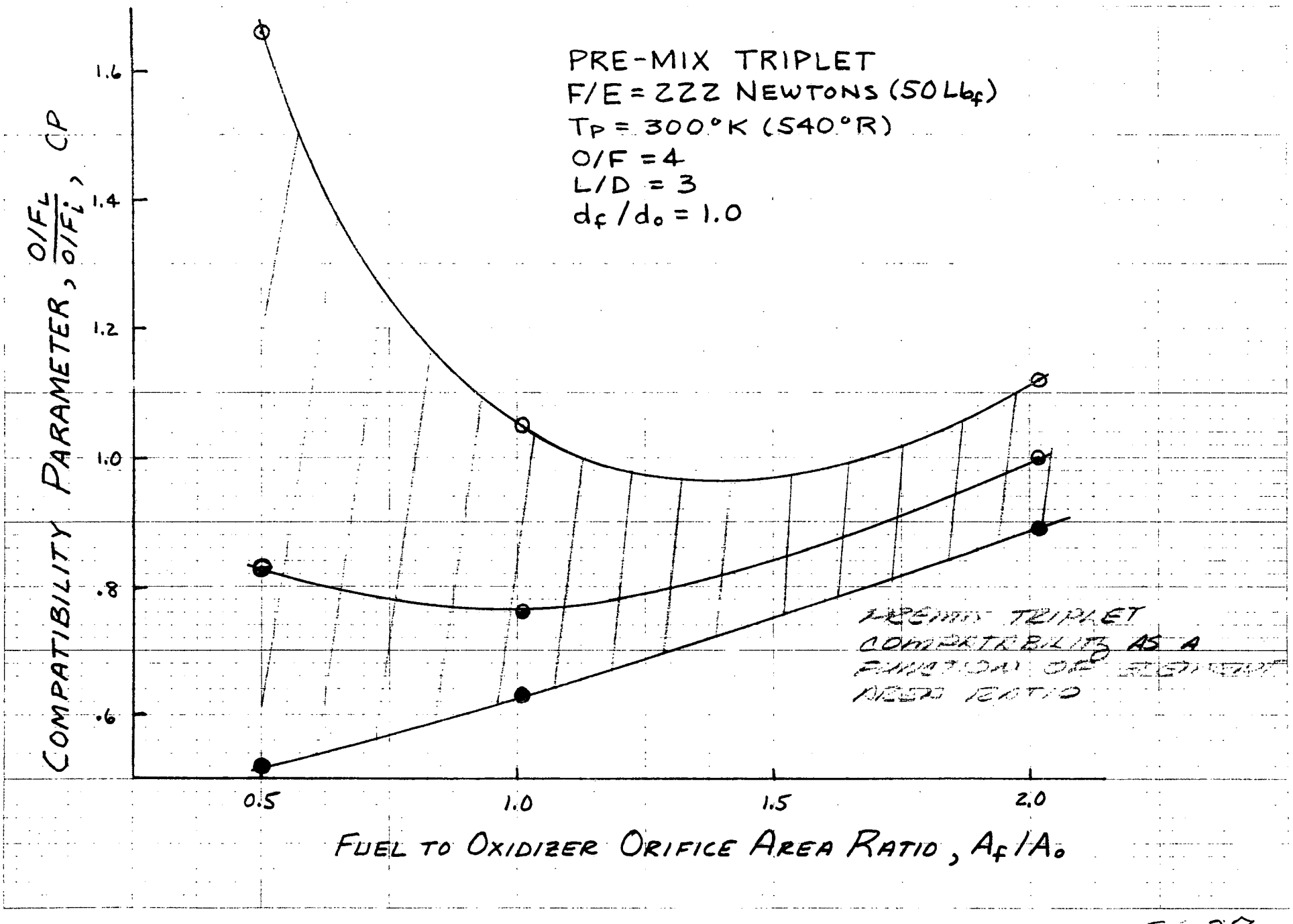
PRE-MIX TRIPLET
F/E = 222 NEWTONS (50 Lbf)
Tp = 300°K (540°R)
O/F = 4
L/D = 3
df / do = 1.0
COMPATIBILITY PARAMETER, O/FL / O/Fi, CP
1.6
1.4
1.2
1.0
.8
.6
0.5
1.0
1.5
2.0
FUEL TO OXIDIZER ORIFICE AREA RATIO, Af/Ao

FIG 27

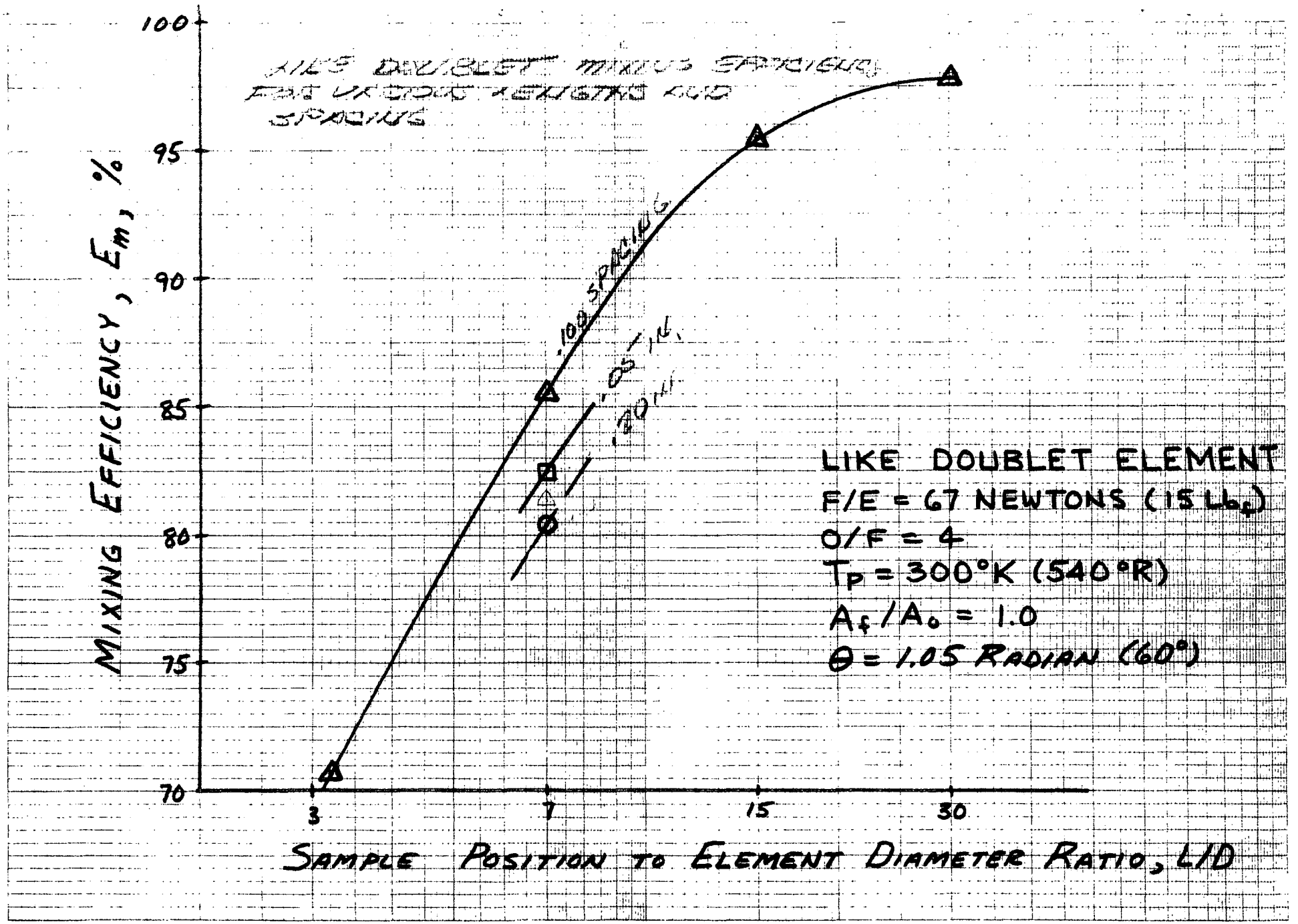
AXIS DOUBLET MINUS SPACING
FAT OXIDIZER HEATED AND
SPACING
100
95
90
85
80
75
70
MIXING EFFICIENCY, E_m, %
.10
.20
.30
3
7
15
30
SAMPLE POSITION TO ELEMENT DIAMETER RATIO, L/D
LIKE DOUBLET ELEMENT
F/E = 67 NEWTONS (15 Lb$_f$)
O/F = 4
T_P = 300°K (540°R)
A_f/A_o = 1.0
θ = 1.05 RADIAN (60°)

FIG 22

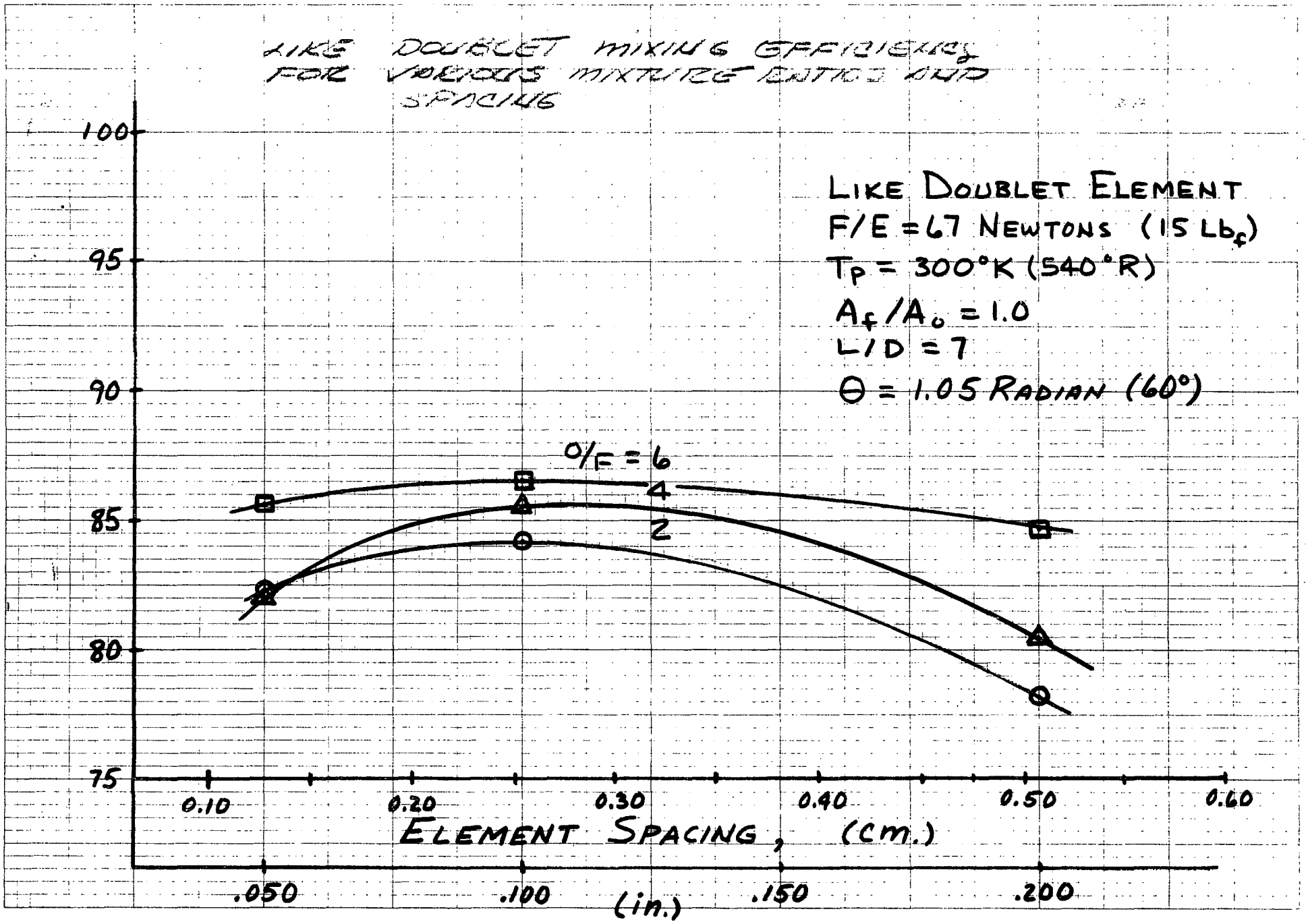

FIG 29

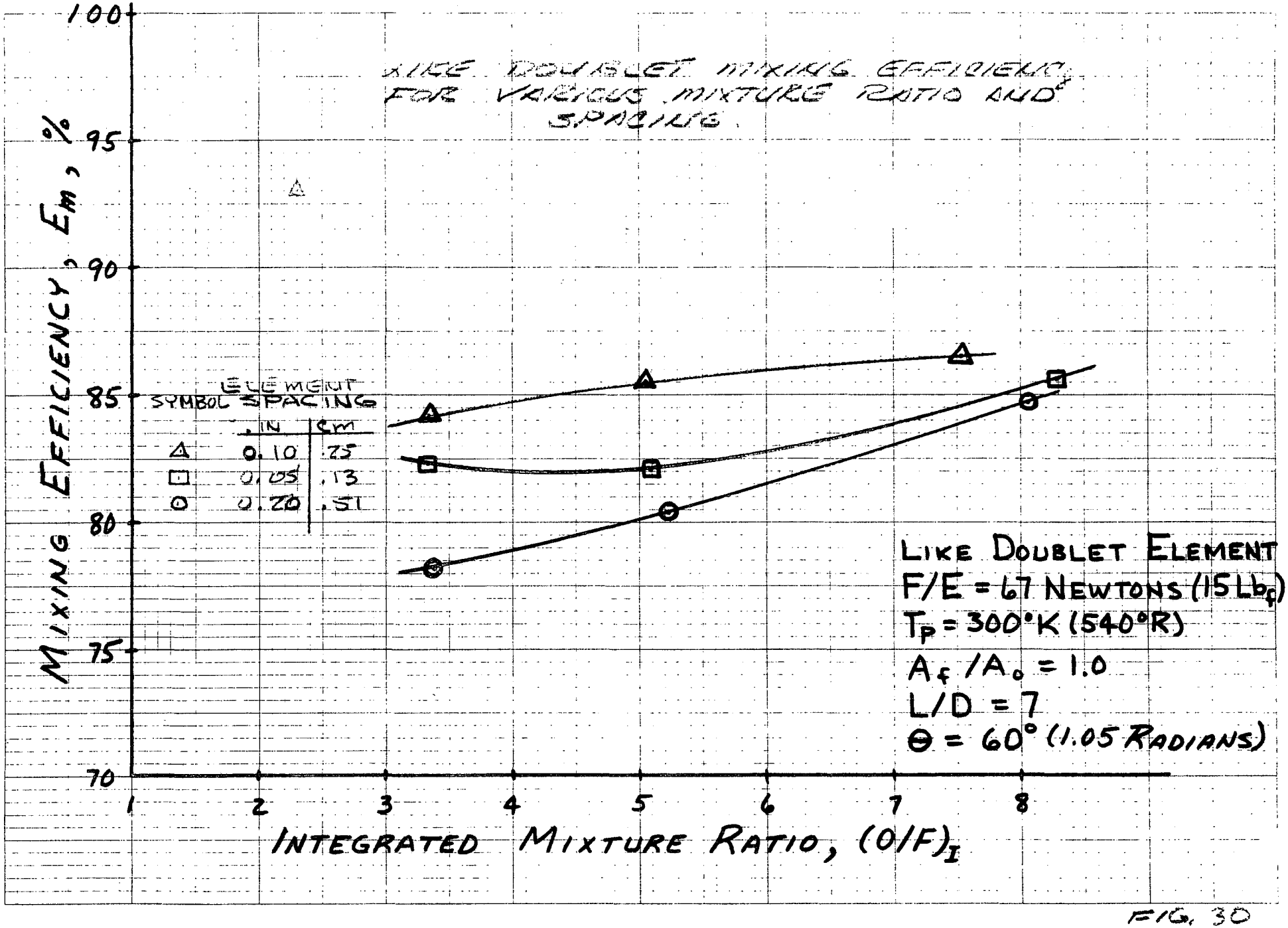
LIKE DOUBLET MIXING EFFICIENCY FOR VARIOUS MIXTURE RATIO AND SPACING
MIXING EFFICIENCY, E_m, %
100
95
90
85
80
75
70
ELEMENT SYMBOL SPACING
IN
ℓ_m
△ 0.10 .25
□ 0.05 .13
○ 0.20 .51
LIKE DOUBLET ELEMENT
F/E = 67 NEWTONS (15 Lb_f)
T_p = 300°K (540°R)
A_f/A_o = 1.0
L/D = 7
Θ = 60° (1.05 RADIANS)
1
2
3
4
5
6
7
8
INTEGRATED MIXTURE RATIO, $(O/F)_I$

FIG. 30

LIKE DOUBLET MIXING EFFICIENCY AS A FUNCTION OF MRED RATIO

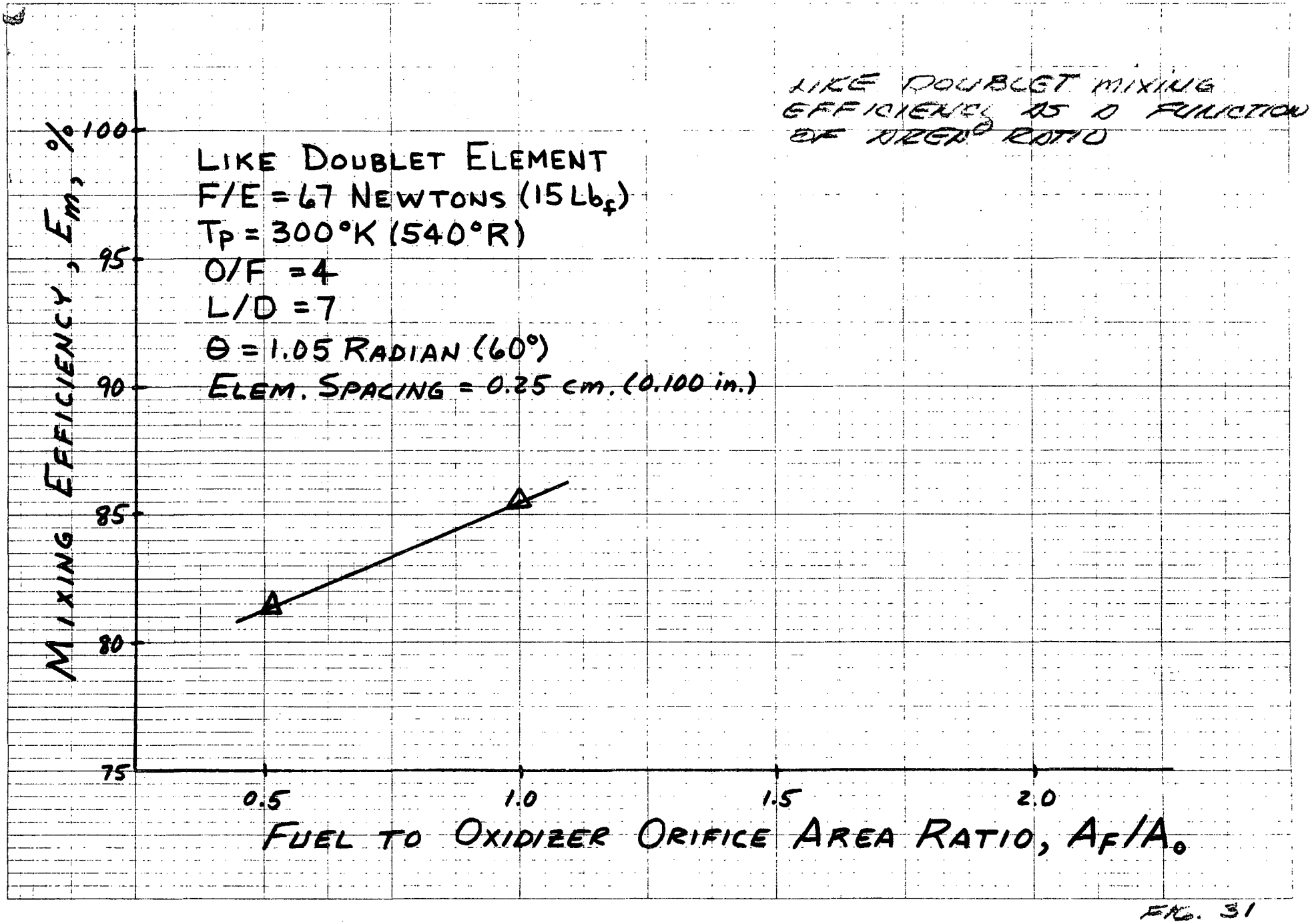

FIG. 31

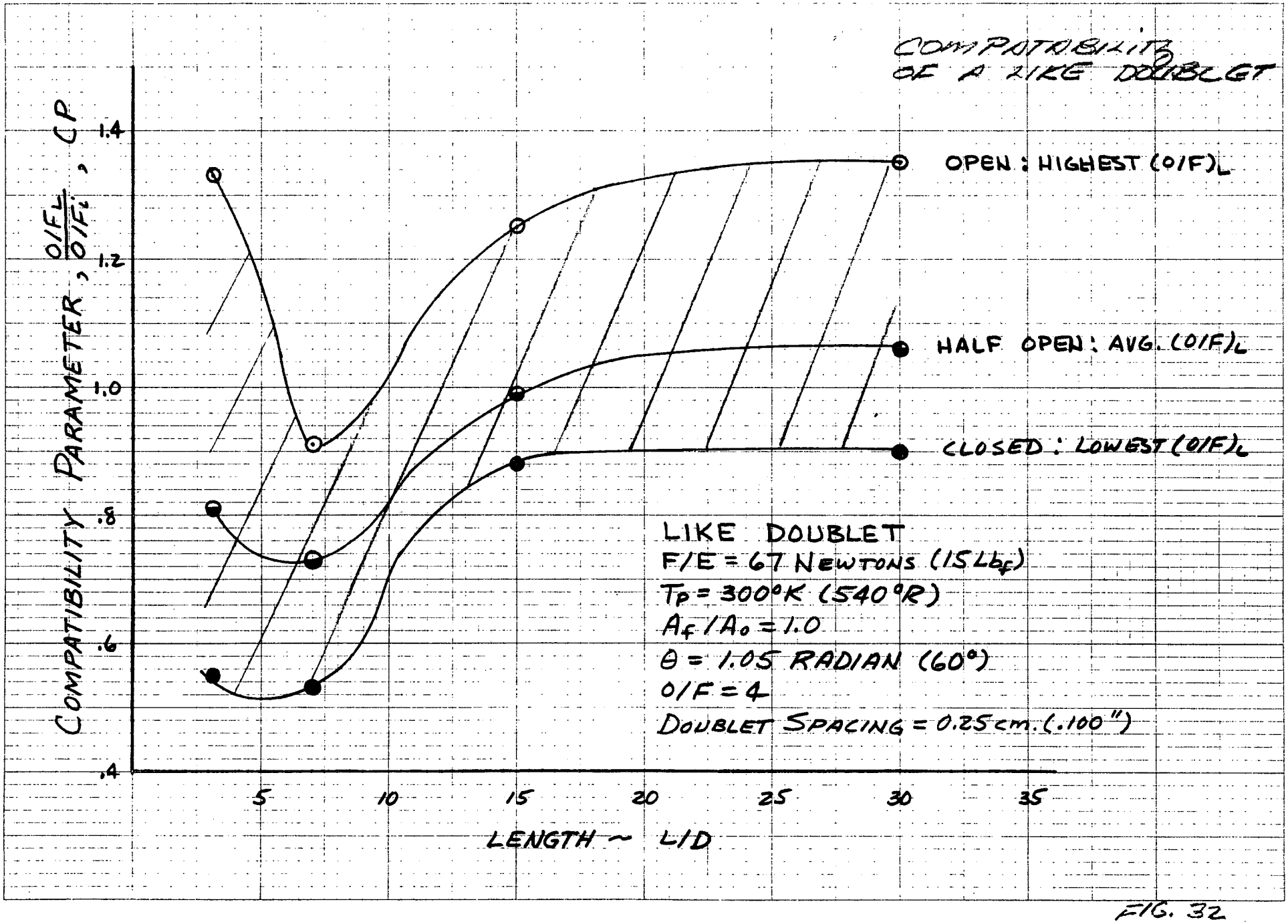

FIG. 32

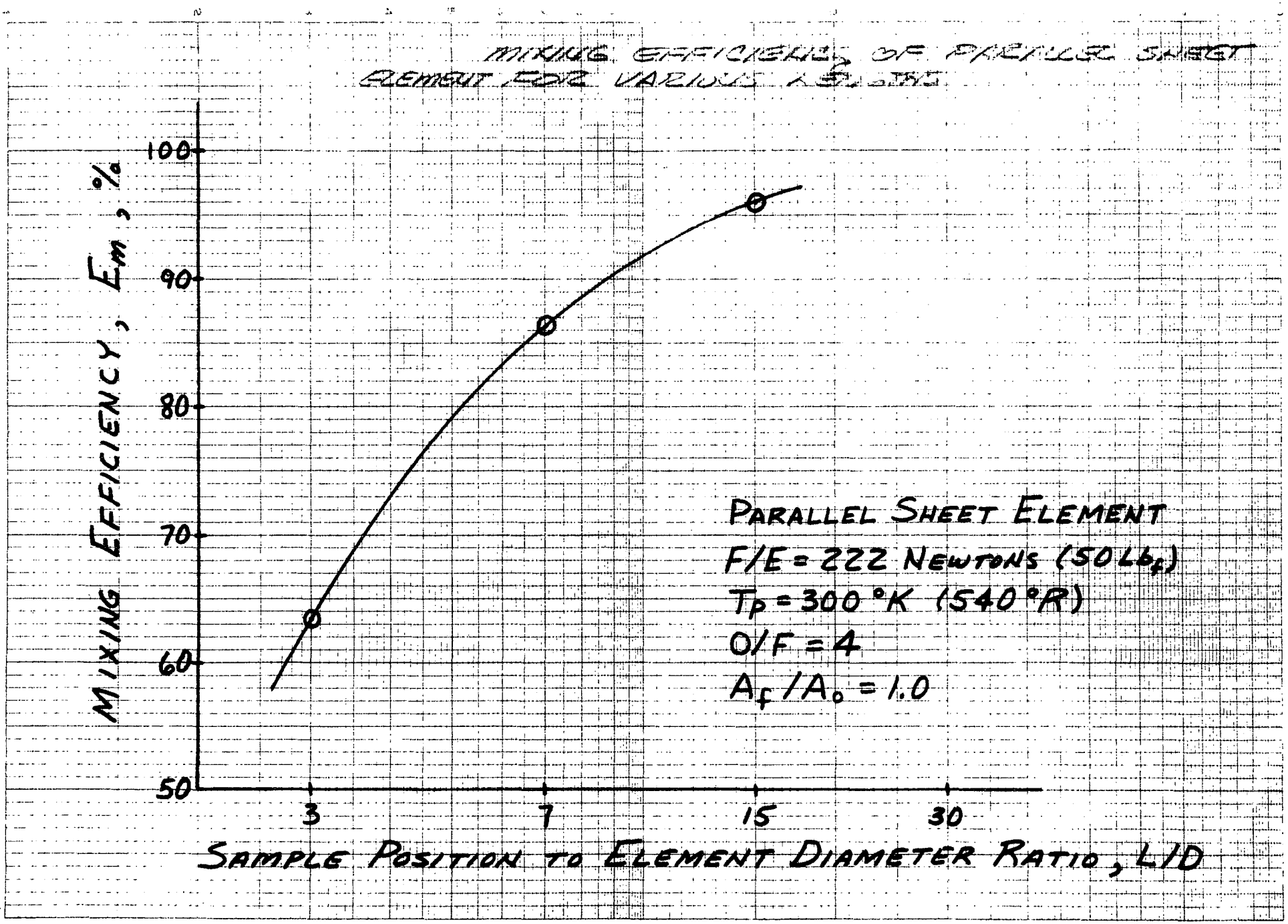
MIXING EFFICIENCY OF PARALLEL SHEET ELEMENT VERSUS L/D
MIXING EFFICIENCY, E_m, %
100
90
80
70
60
50
3
7
15
30
SAMPLE POSITION TO ELEMENT DIAMETER RATIO, L/D
PARALLEL SHEET ELEMENT
F/E = 222 NEWTONS (50 Lbf)
T_p = 300 °K (540 °R)
O/F = 4
A_f/A_o = 1.0

FIG 33

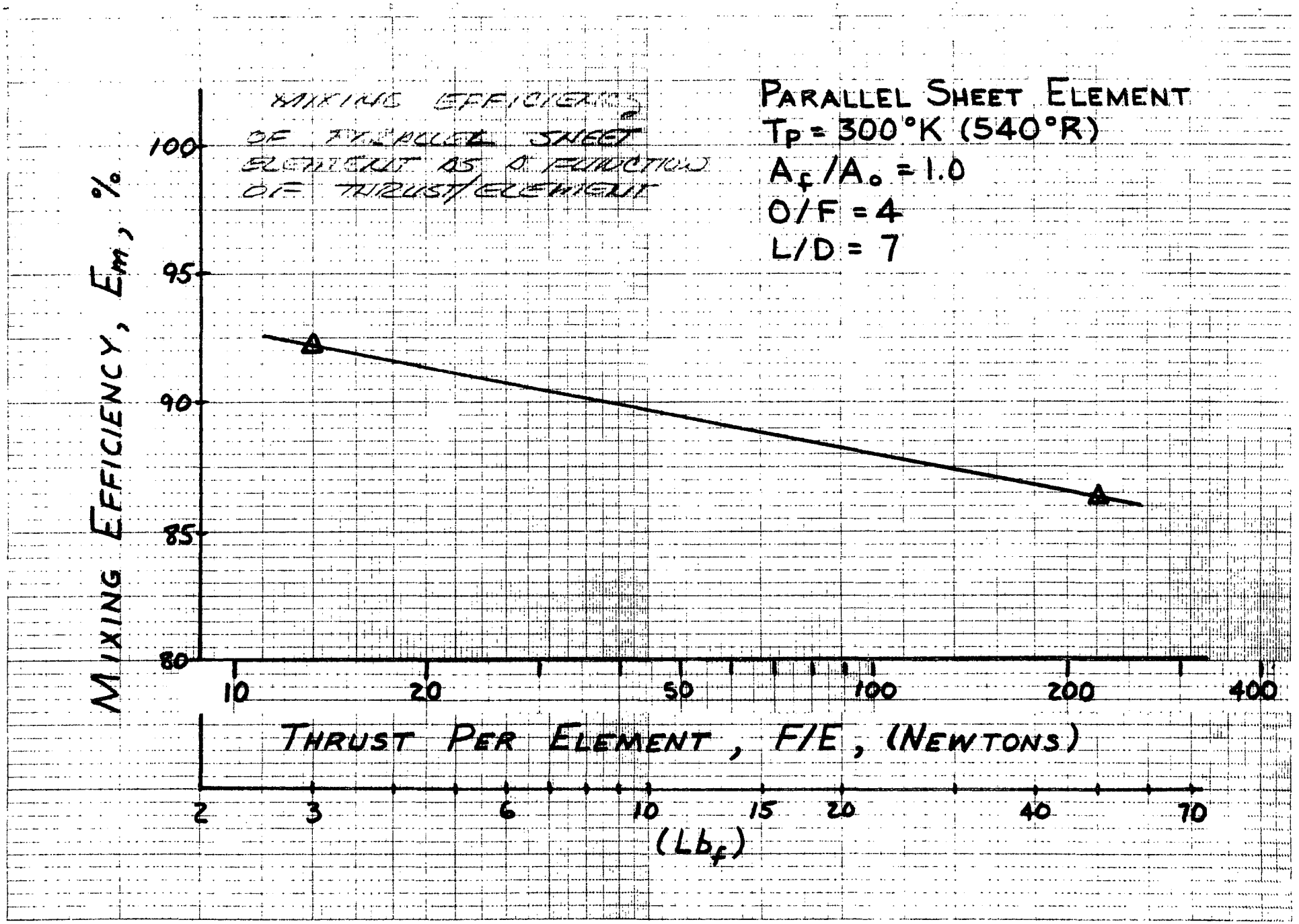
MIXING EFFICIENCY OF PARALLEL SHEET ELEMENT AS A FUNCTION OF THRUST/ELEMENT
PARALLEL SHEET ELEMENT
T_p = 300°K (540°R)
A_f/A_o = 1.0
O/F = 4
L/D = 7
MIXING EFFICIENCY, E_m, %
100
95
90
85
80
10
20
50
100
200
400
THRUST PER ELEMENT, F/E, (NEWTONS)
2
3
6
10
15
20
40
70
(Lb_f)

FIG. 37

MIXING EFFICIENCY OF PARALLEL SHEET ELEMENT AS A FUNCTION OF PROPELLANT TEMP

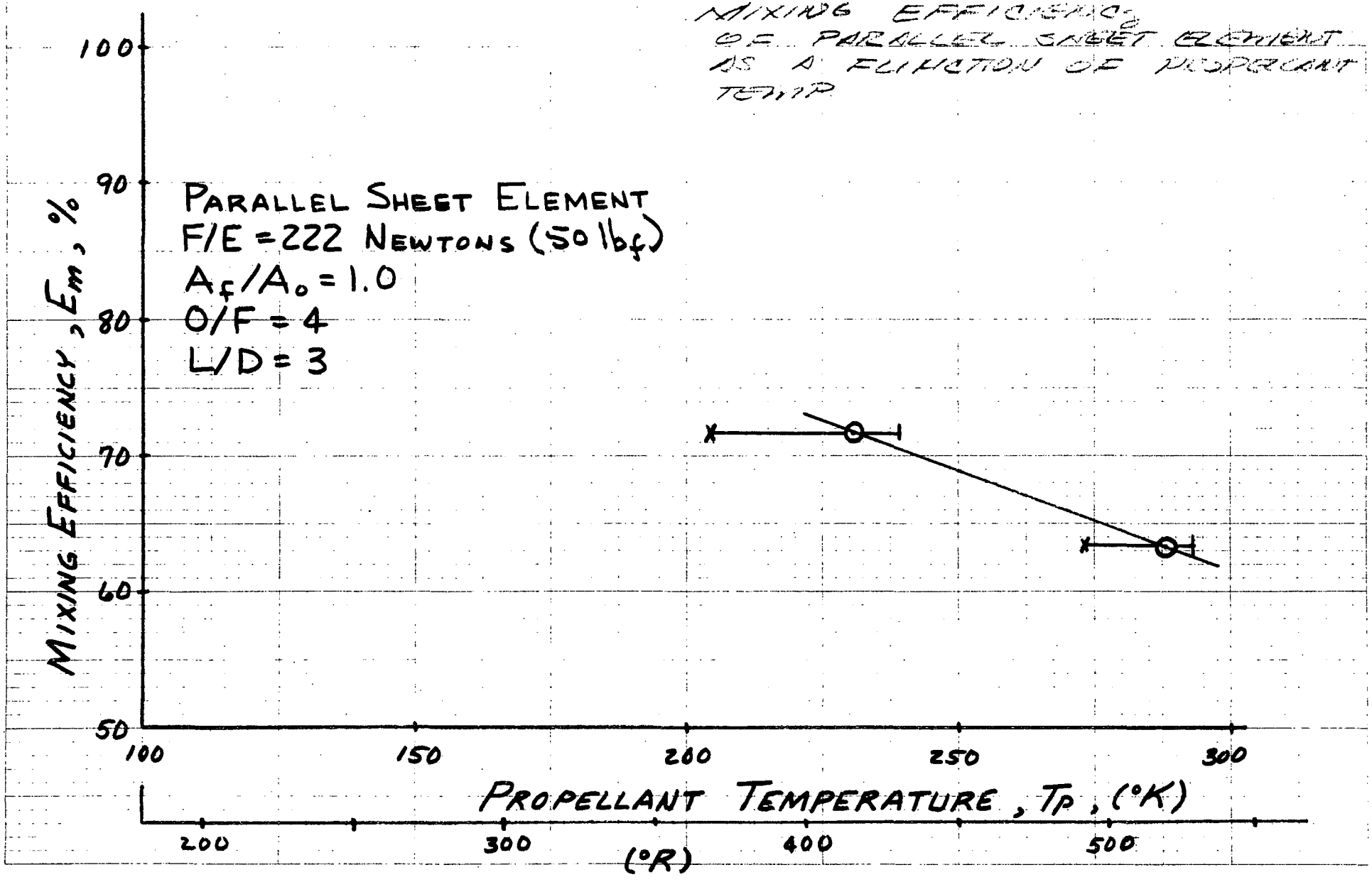

FIG 35

MIXING OF PARALLEL SHEET ELEMENT AS A FUNCTION OF INTEGRATED MIXTURE RATIO

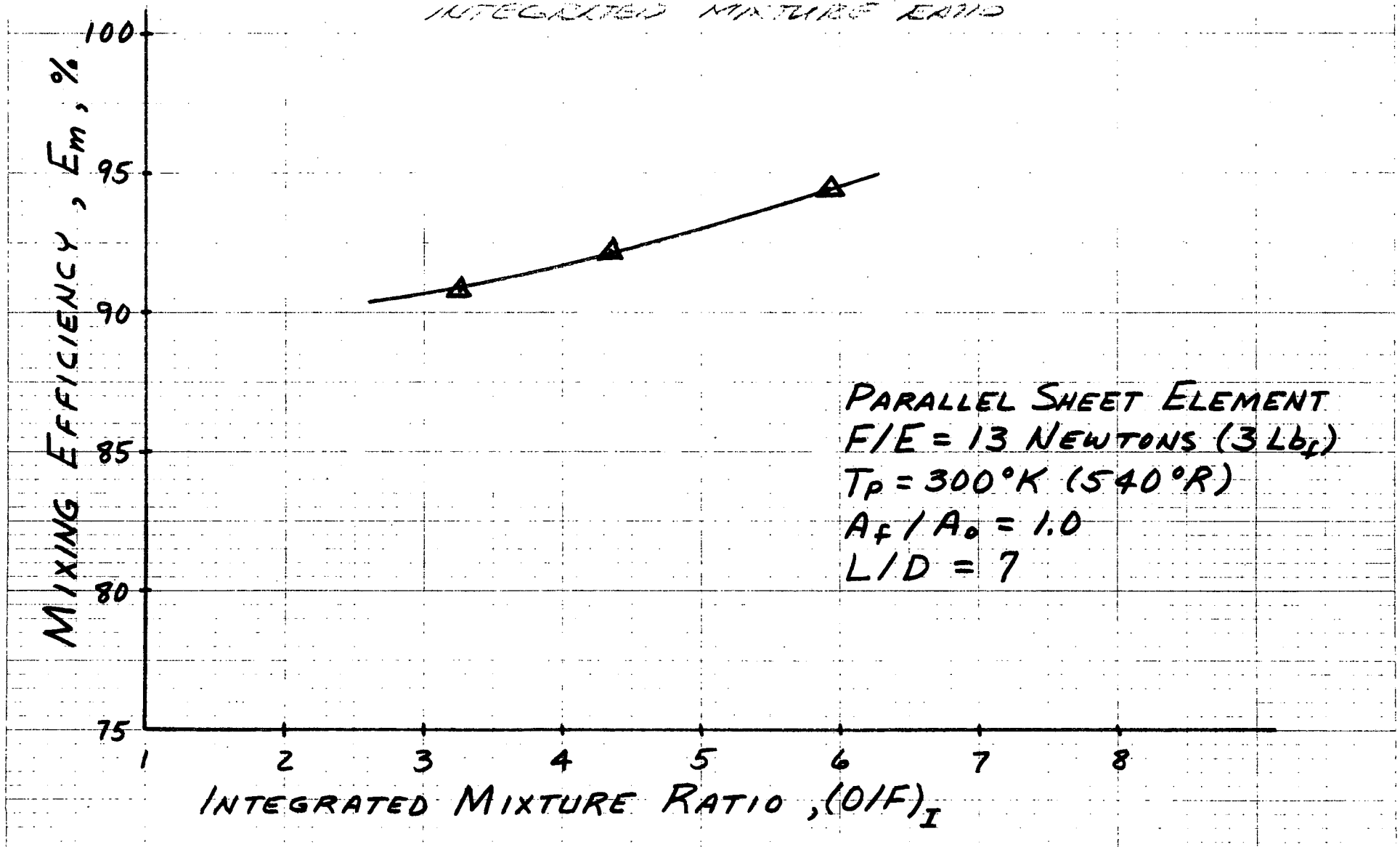

FIG. 36

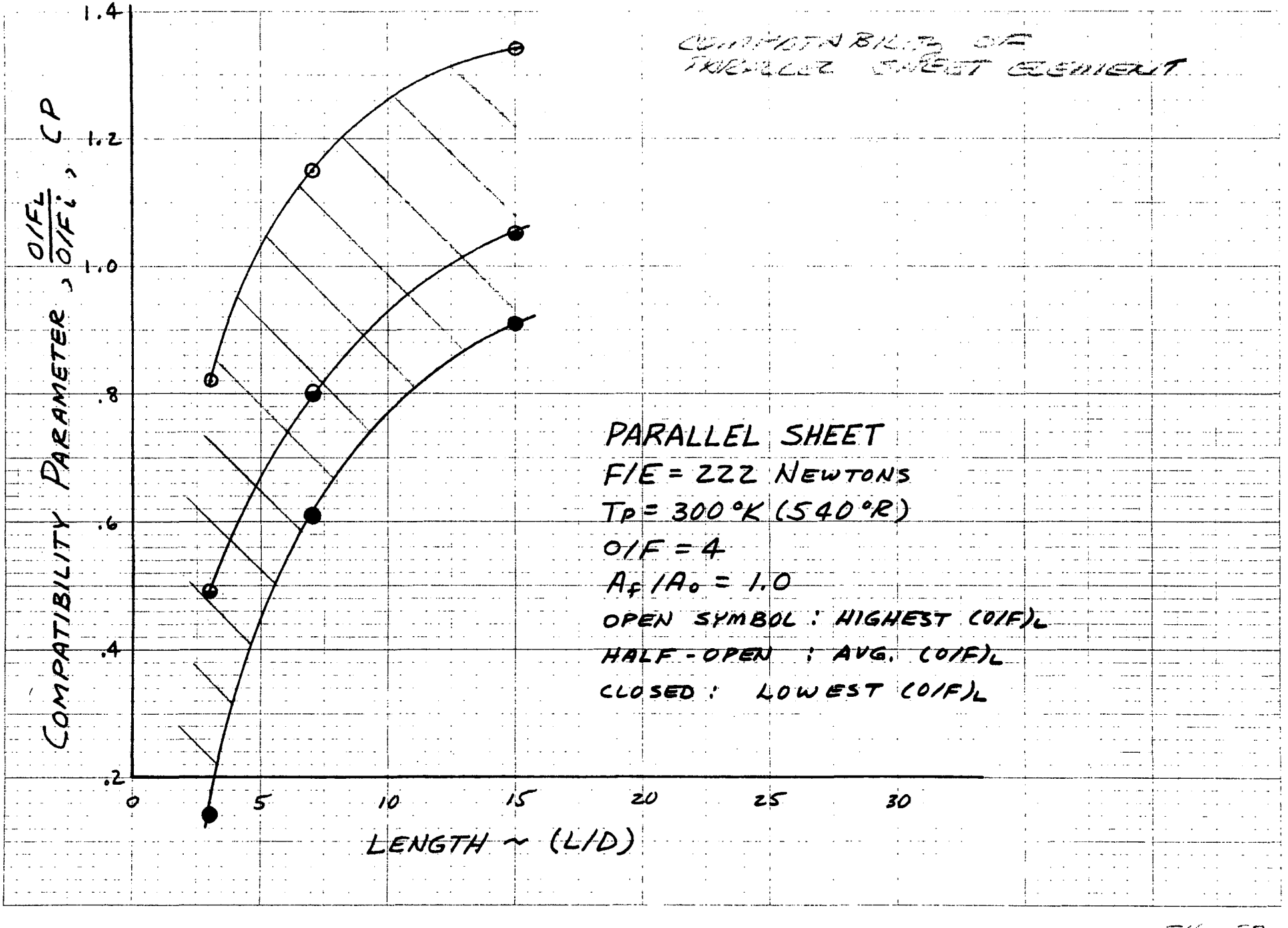
COMPATIBILITY PARAMETER, $\frac{O/F_L}{O/F_i}$, CP
1.4
1.2
1.0
.8
.6
.4
.2
0
5
10
15
20
25
30
LENGTH ~ (L/D)
COMBUSTIBLE OF
PROPELLED SWEPT SEGMENT
PARALLEL SHEET
F/E = 222 NEWTONS
T_P = 300°K (540°R)
O/F = 4
A_f/A_o = 1.0
OPEN SYMBOL : HIGHEST $(O/F)_L$
HALF-OPEN : AVG. $(O/F)_L$
CLOSED : LOWEST $(O/F)_L$

FIG. 57

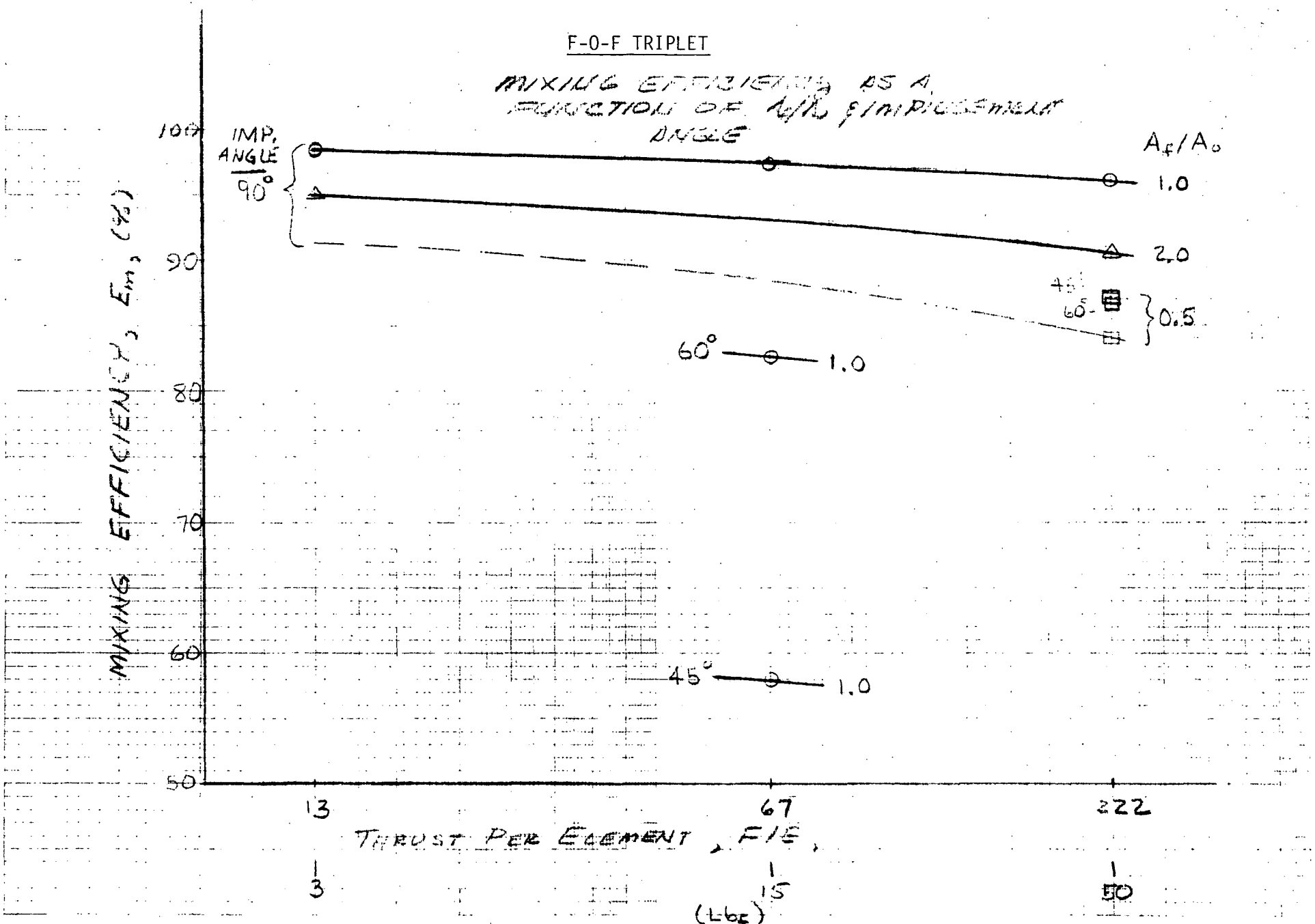
F-O-F TRIPLET
MIXING EFFICIENCY AS A FUNCTION OF A_f/A_o & IMPINGEMENT ANGLE
IMP. ANGLE
90°
A_f/A_o
1.0
2.0
0.5
45°
60°
60°
1.0
45°
1.0
MIXING EFFICIENCY, E_m, (%)
100
90
80
70
60
50
13
67
222
THRUST PER ELEMENT, F/E,
$\frac{1}{3}$
$\frac{1}{15}$
$\frac{1}{50}$
(Lbf)

FIG 38

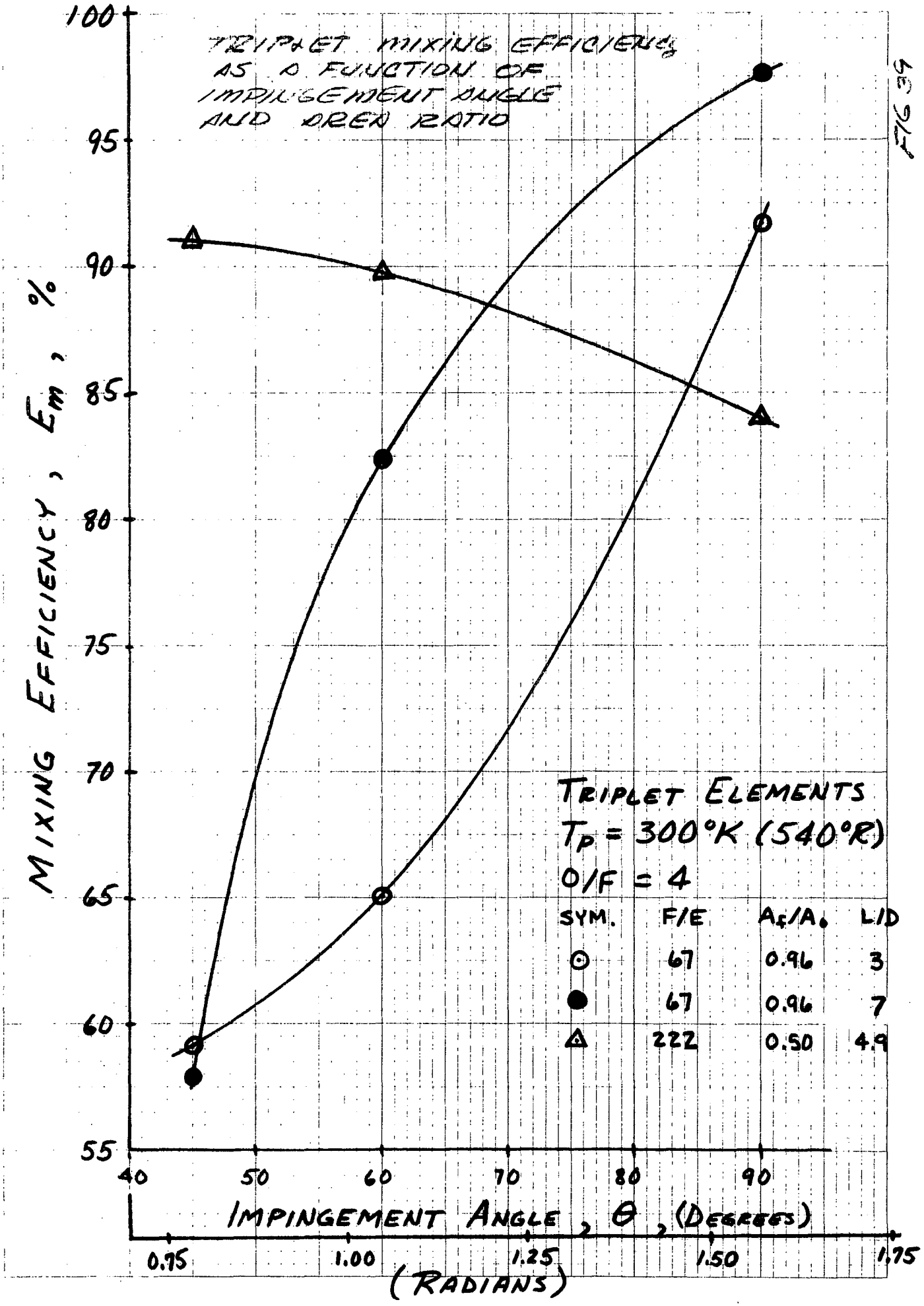
TRIPLET MIXING EFFICIENCY AS A FUNCTION OF IMPINGEMENT ANGLE AND ORIFICE RATIO
MIXING EFFICIENCY, E_m, %
100
95
90
85
80
75
70
65
60
55
TRIPLET ELEMENTS
T_P = 300°K (540°R)
O/F = 4
SYM. F/E A_c/A_o L/D
67 0.96 3
67 0.96 7
222 0.50 4.9
40 50 60 70 80 90
IMPINGEMENT ANGLE, θ, (DEGREES)
0.95 1.00 1.25 1.50 1.75
(RADIANS)

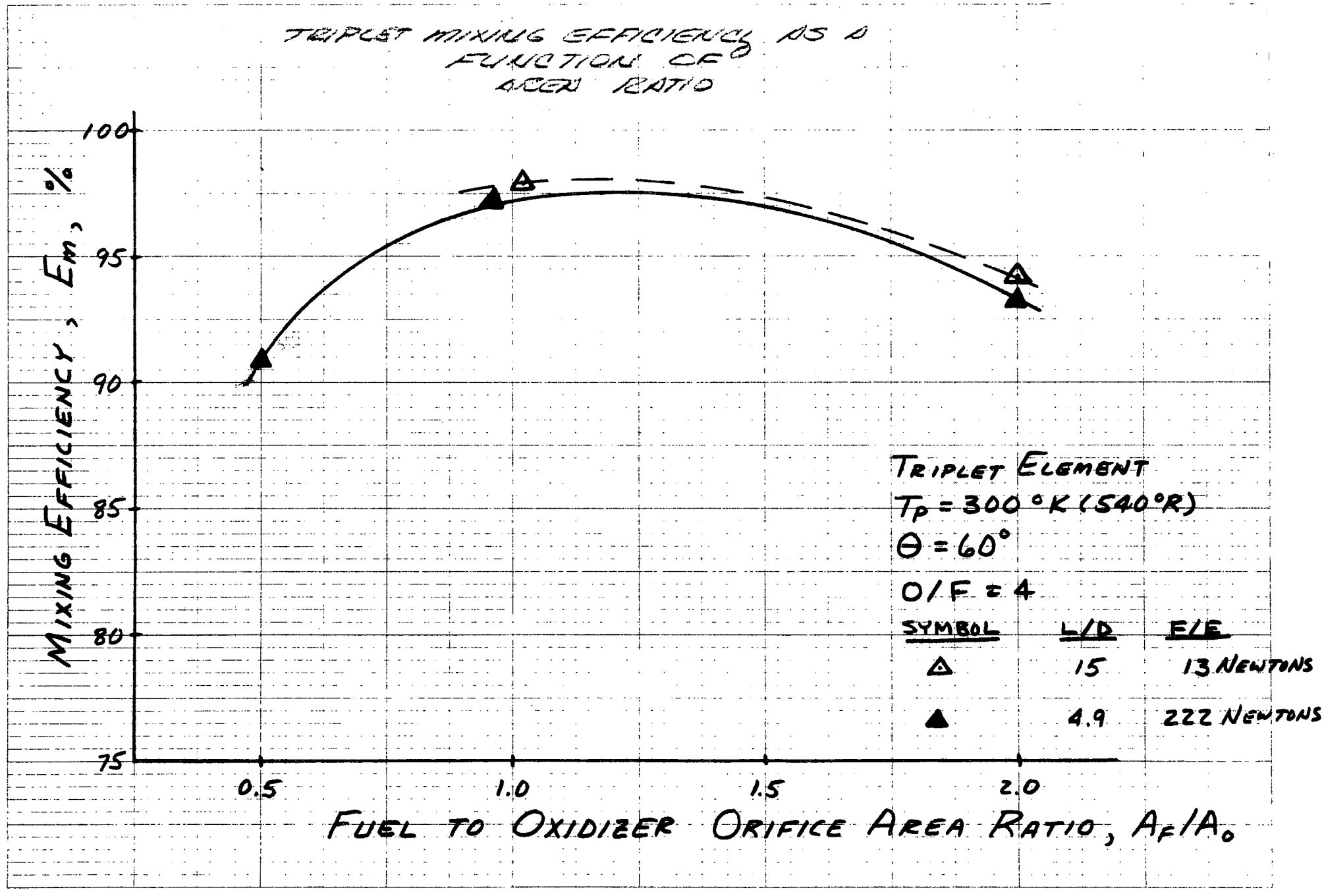
TRIPLET MIXING EFFICIENCY AS A FUNCTION OF ORIFICE RATIO
MIXING EFFICIENCY, E_m, %
100
95
90
85
80
75
0.5
1.0
1.5
2.0
FUEL TO OXIDIZER ORIFICE AREA RATIO, A_F/A_O
TRIPLET ELEMENT
$T_P = 300°K (540°R)$
$\theta = 60°$
O/F = 4
SYMBOL | L/D | F/E
△ | 15 | 13 NEWTONS
▲ | 4.9 | 222 NEWTONS

FIG. 40

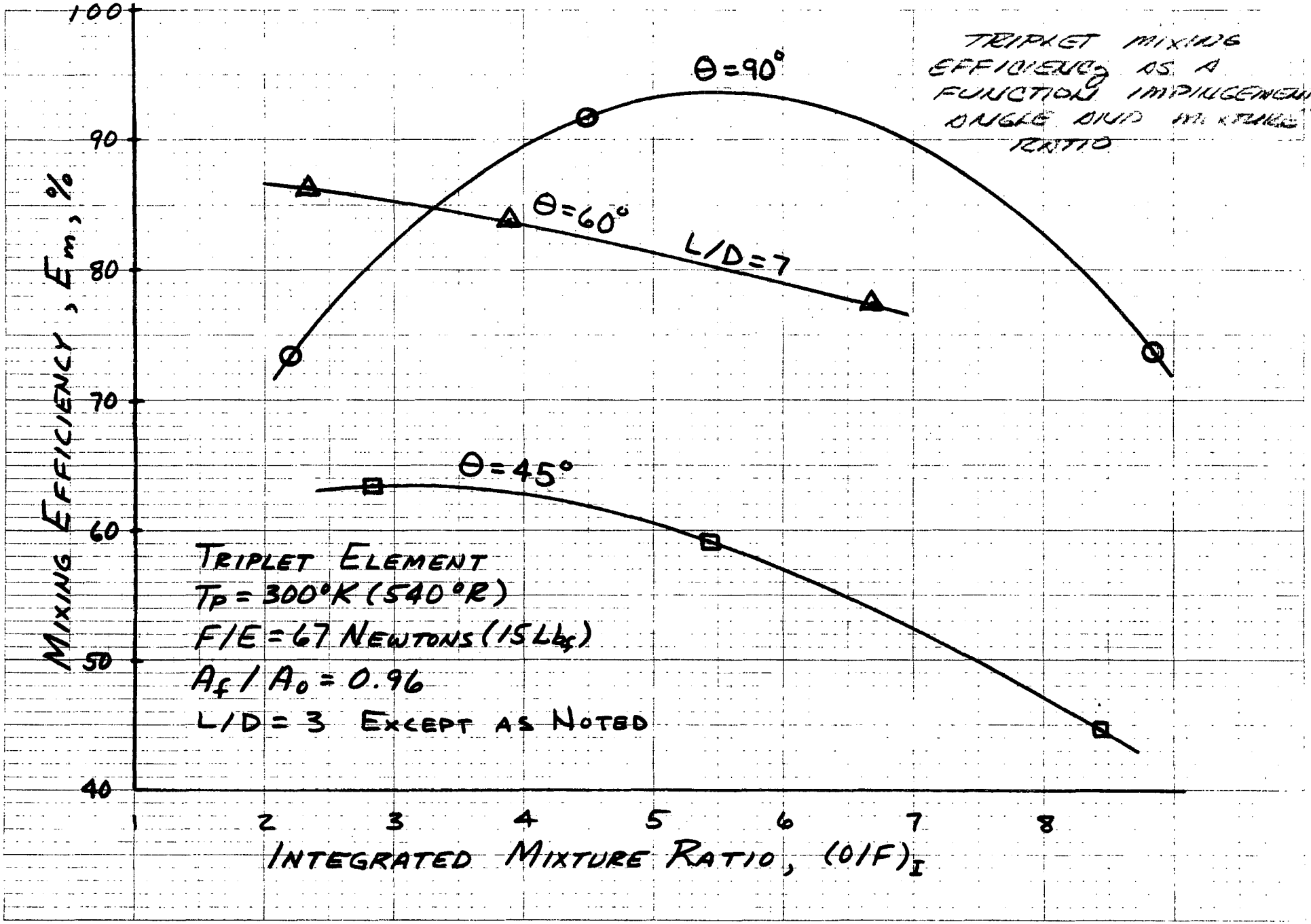
TRIPLET MIXING EFFICIENCY AS A FUNCTION IMPINGEMENT ANGLE AND MIXTURE RATIO
θ=90°
θ=60°
L/D=7
θ=45°
TRIPLET ELEMENT
T_P = 300°K (540°R)
F/E = 67 NEWTONS (15 Lb_f)
A_f / A_o = 0.96
L/D = 3 EXCEPT AS NOTED
MIXING EFFICIENCY, E_m, %
100
90
80
70
60
50
40
1
2
3
4
5
6
7
8
INTEGRATED MIXTURE RATIO, $(O/F)_I$

FIG 41

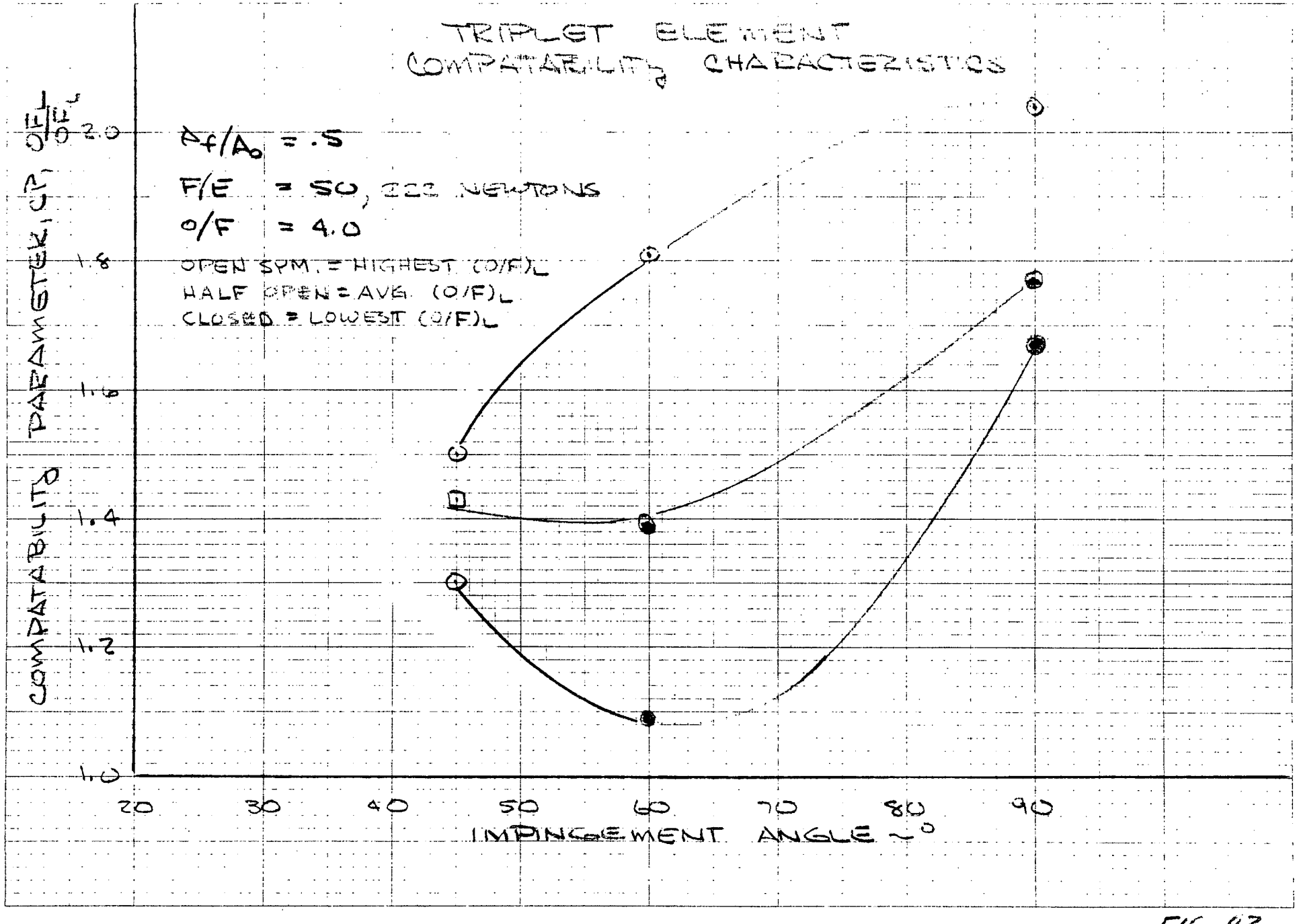
TRIPLET ELEMENT
COMPATABILITY CHARACTERISTICS
A_f/A_o = .5
F/E = 50, 222 NEWTONS
O/F = 4.0
OPEN SYM. = HIGHEST $(O/F)_L$
HALF OPEN = AVG. $(O/F)_L$
CLOSED = LOWEST $(O/F)_L$
COMPATABILITY PARAMETER, $\frac{(O/F)_L}{(O/F)_T}$
2.0
1.8
1.6
1.4
1.2
1.0
20
30
40
50
60
70
80
90
IMPINGEMENT ANGLE ~ °

FIG. 42

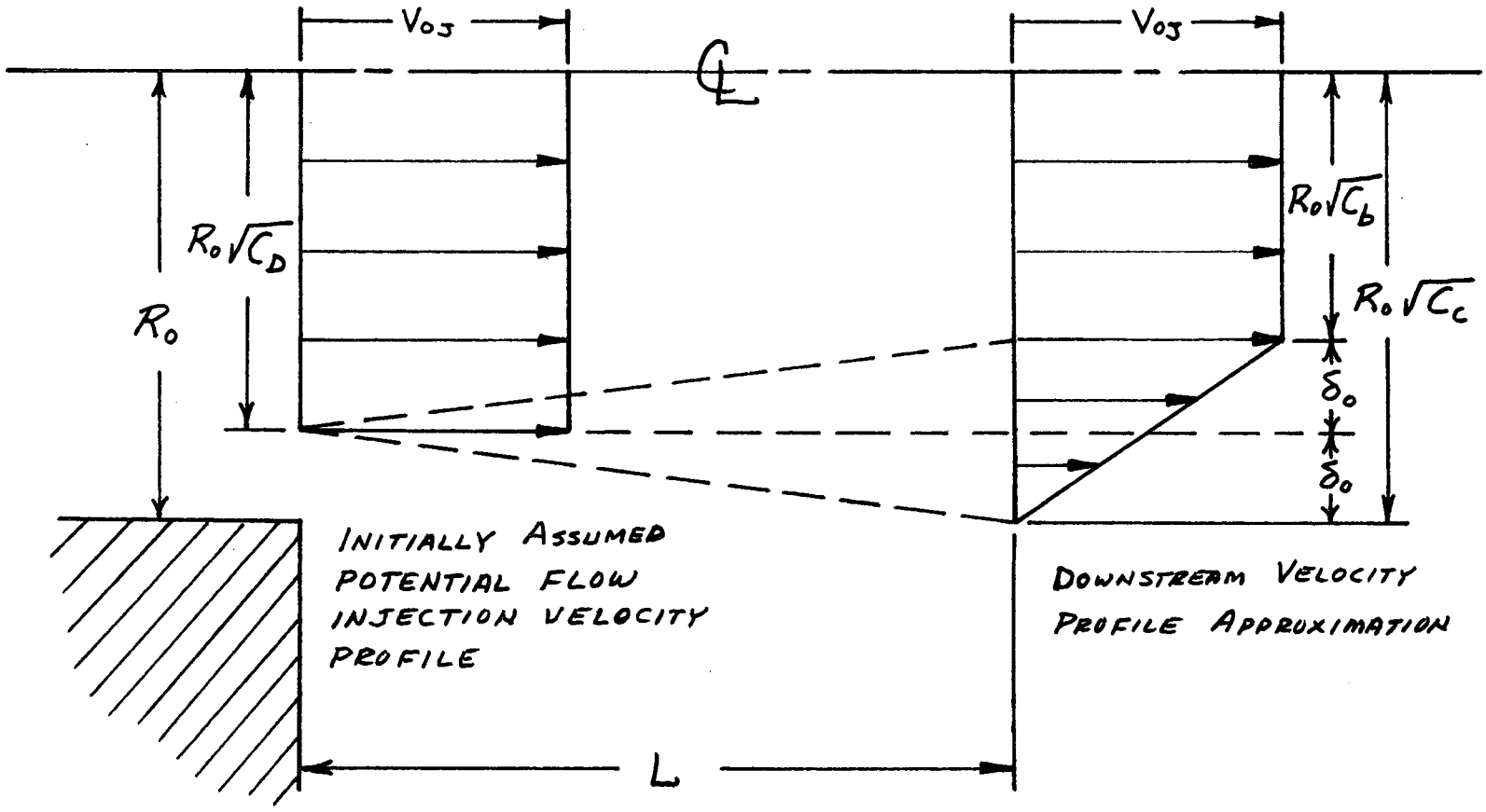
V_{oJ}
V_{oJ}
$R_o\sqrt{C_D}$
R_o
$R_o\sqrt{C_b}$
$R_o\sqrt{C_c}$
δ_o
δ_o
INITIALLY ASSUMED POTENTIAL FLOW INJECTION VELOCITY PROFILE
DOWNSTREAM VELOCITY PROFILE APPROXIMATION
L

FIG. 43

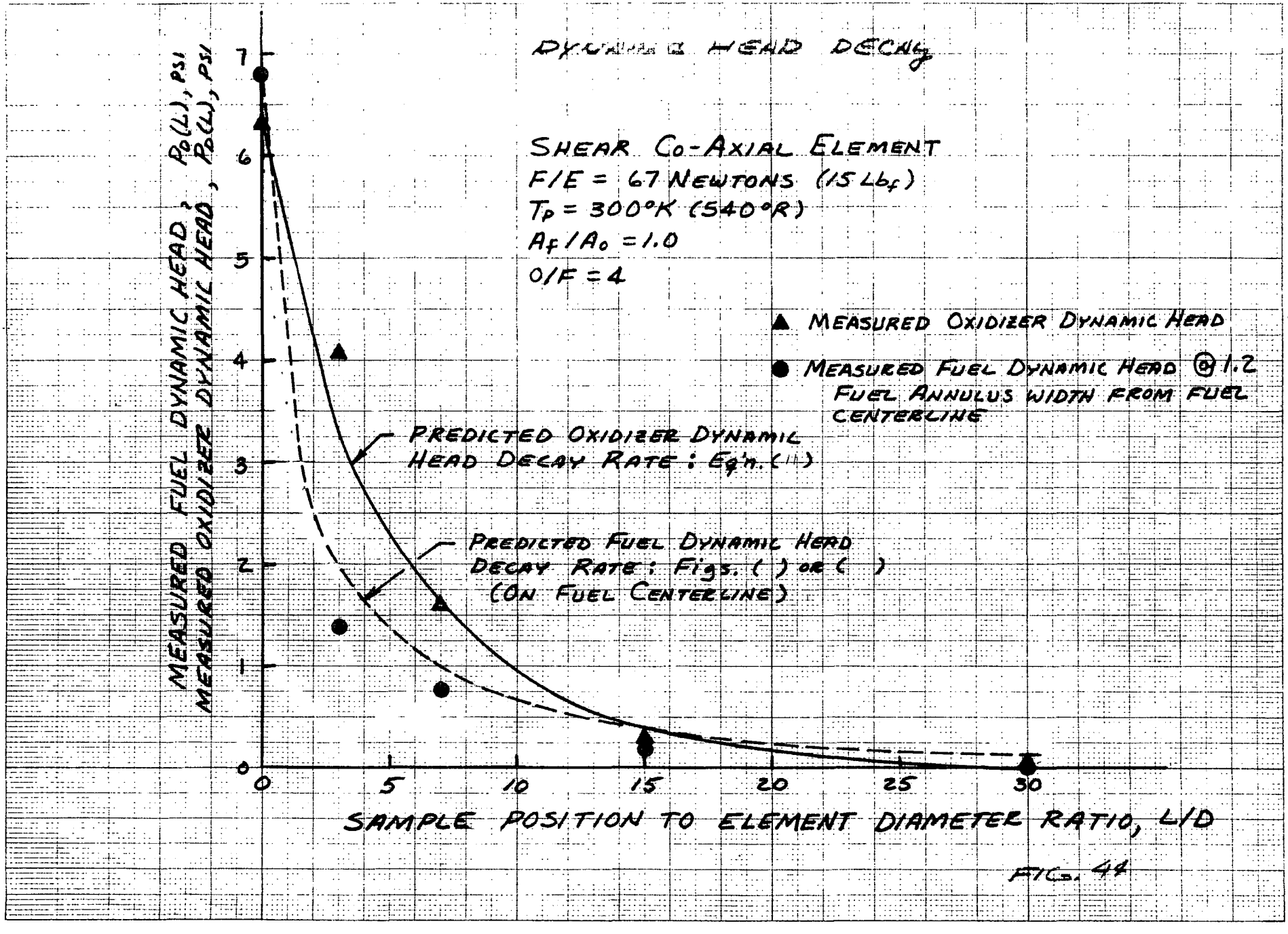
DYNAMIC HEAD DECAY
SHEAR CO-AXIAL ELEMENT
F/E = 67 NEWTONS (15 Lbf)
Tp = 300°K (540°R)
Af/Ao = 1.0
O/F = 4
▲ MEASURED OXIDIZER DYNAMIC HEAD
● MEASURED FUEL DYNAMIC HEAD @ 1.2 FUEL ANNULUS WIDTH FROM FUEL CENTERLINE
PREDICTED OXIDIZER DYNAMIC HEAD DECAY RATE: Eq'n. (11)
PREDICTED FUEL DYNAMIC HEAD DECAY RATE: Figs. ( ) OR ( ) (ON FUEL CENTERLINE)
MEASURED FUEL DYNAMIC HEAD, Po(L), PSI
MEASURED OXIDIZER DYNAMIC HEAD, Pf(L), PSI
0
1
2
3
4
5
6
7
0
5
10
15
20
25
30
SAMPLE POSITION TO ELEMENT DIAMETER RATIO, L/D

FIG. 44

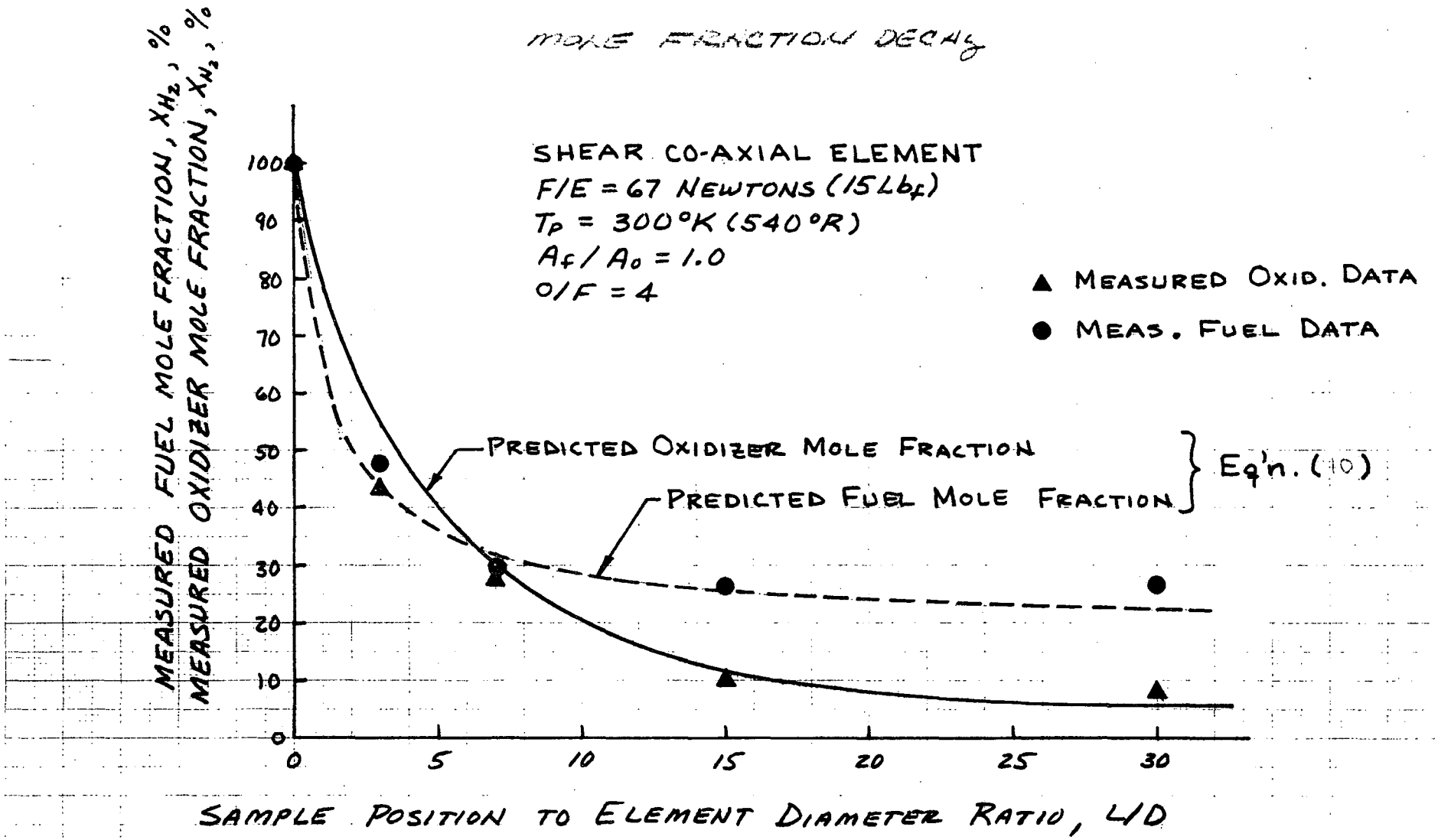
MOLE FRACTION DECAY
SHEAR CO-AXIAL ELEMENT
F/E = 67 NEWTONS (15Lbf)
T_P = 300°K (540°R)
A_f / A_o = 1.0
O/F = 4
▲ MEASURED OXID. DATA
● MEAS. FUEL DATA
PREDICTED OXIDIZER MOLE FRACTION
PREDICTED FUEL MOLE FRACTION
Eq'n. (10)
MEASURED FUEL MOLE FRACTION, X_{H_2}, %
MEASURED OXIDIZER MOLE FRACTION, X_{N_2}, %
100
90
80
70
60
50
40
30
20
10
0
0
5
10
15
20
25
30
SAMPLE POSITION TO ELEMENT DIAMETER RATIO, L/D

FIG. 45

FIG 96

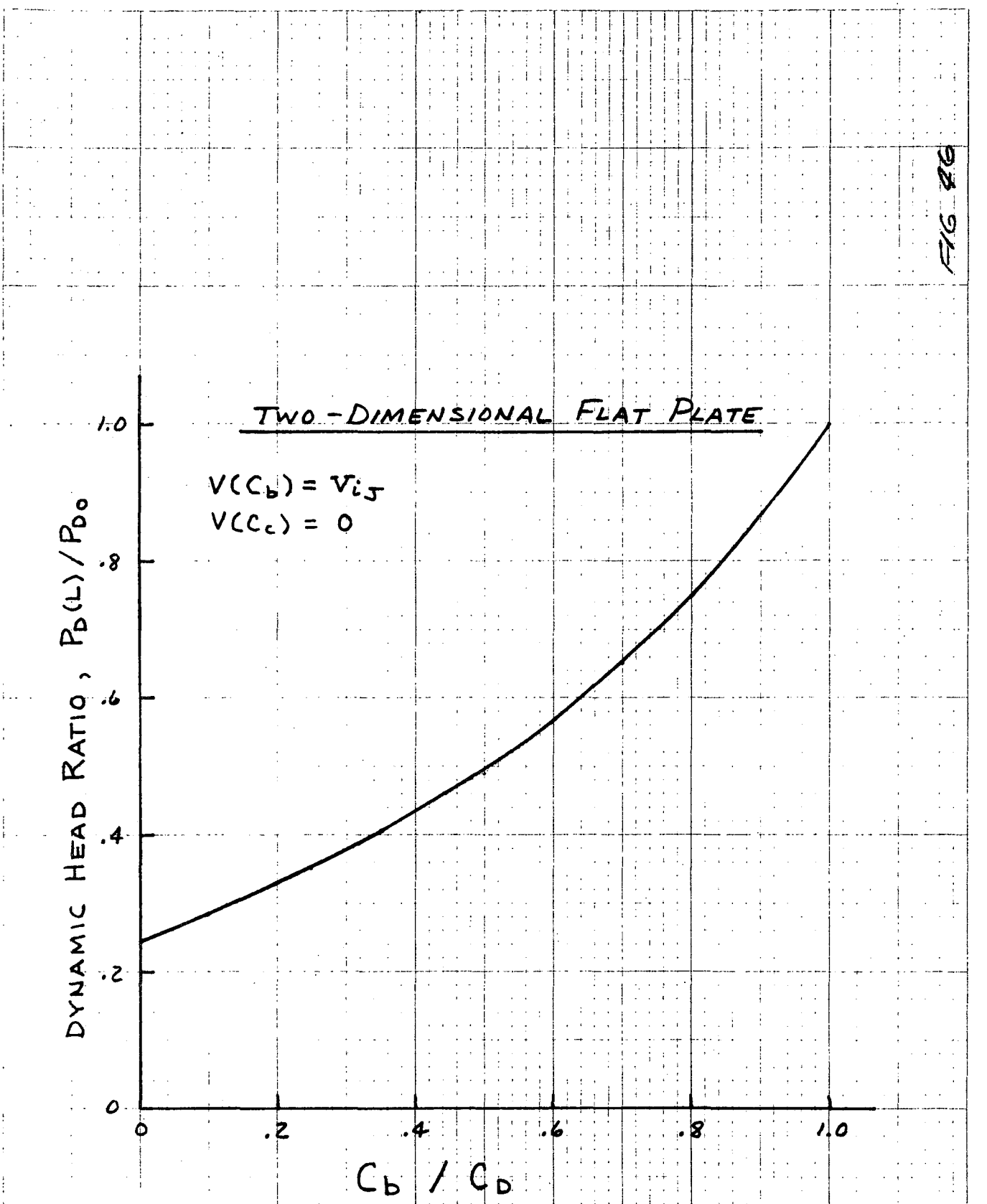

Figure EFFECT OF POTENTIAL FLOW RATIO ON TWO DIMENSIONAL JET DYNAMIC HEAD RATIO

FIG 96

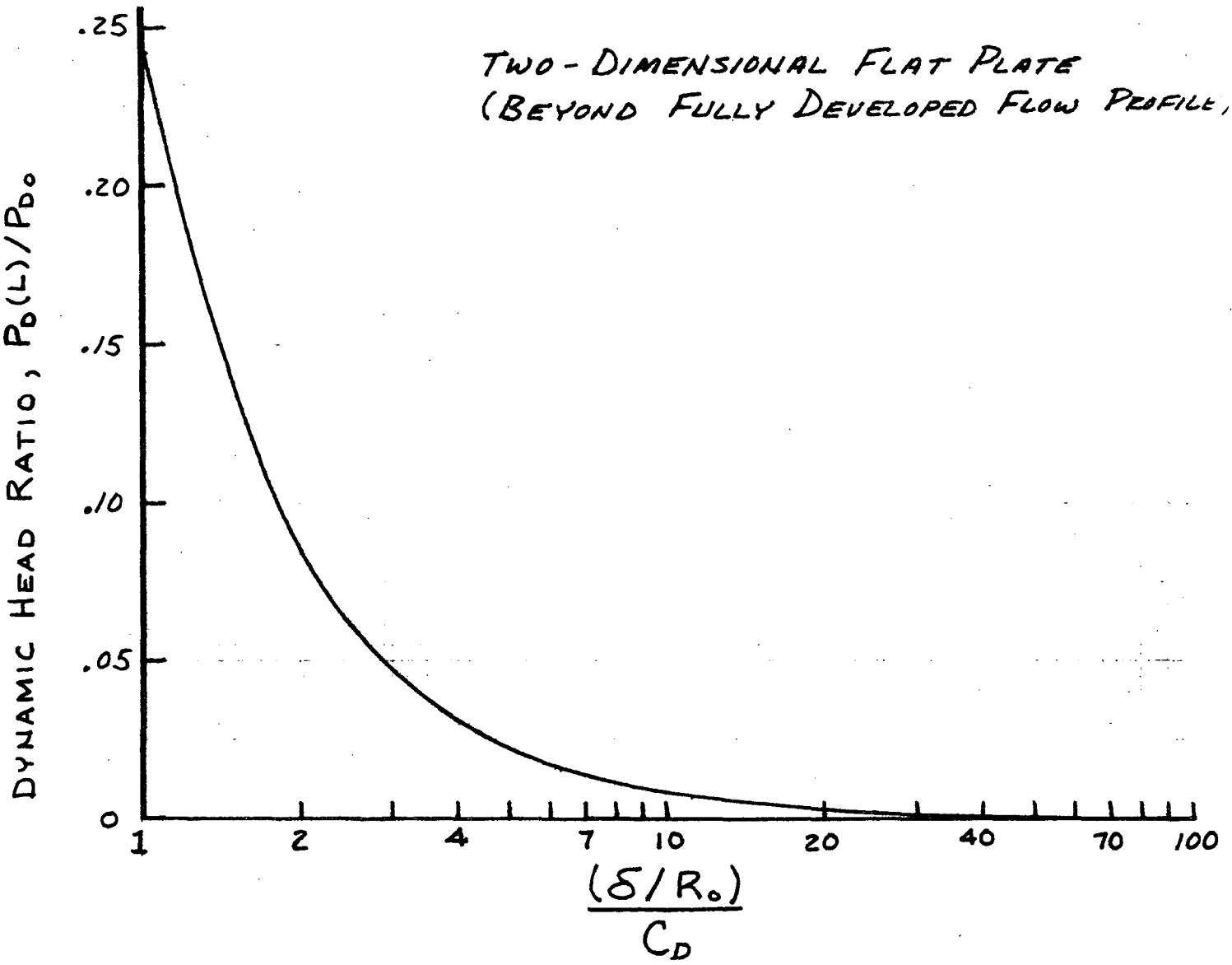
TWO-DIMENSIONAL FLAT PLATE
(BEYOND FULLY DEVELOPED FLOW PROFILE)
DYNAMIC HEAD RATIO, $P_b(L)/P_{b_0}$
.25
.20
.15
.10
.05
0
1
2
4
7
10
20
40
70
100
$\frac{(\delta/R_0)}{C_D}$

FIG 47

Analytical Correlation of Experimental Data

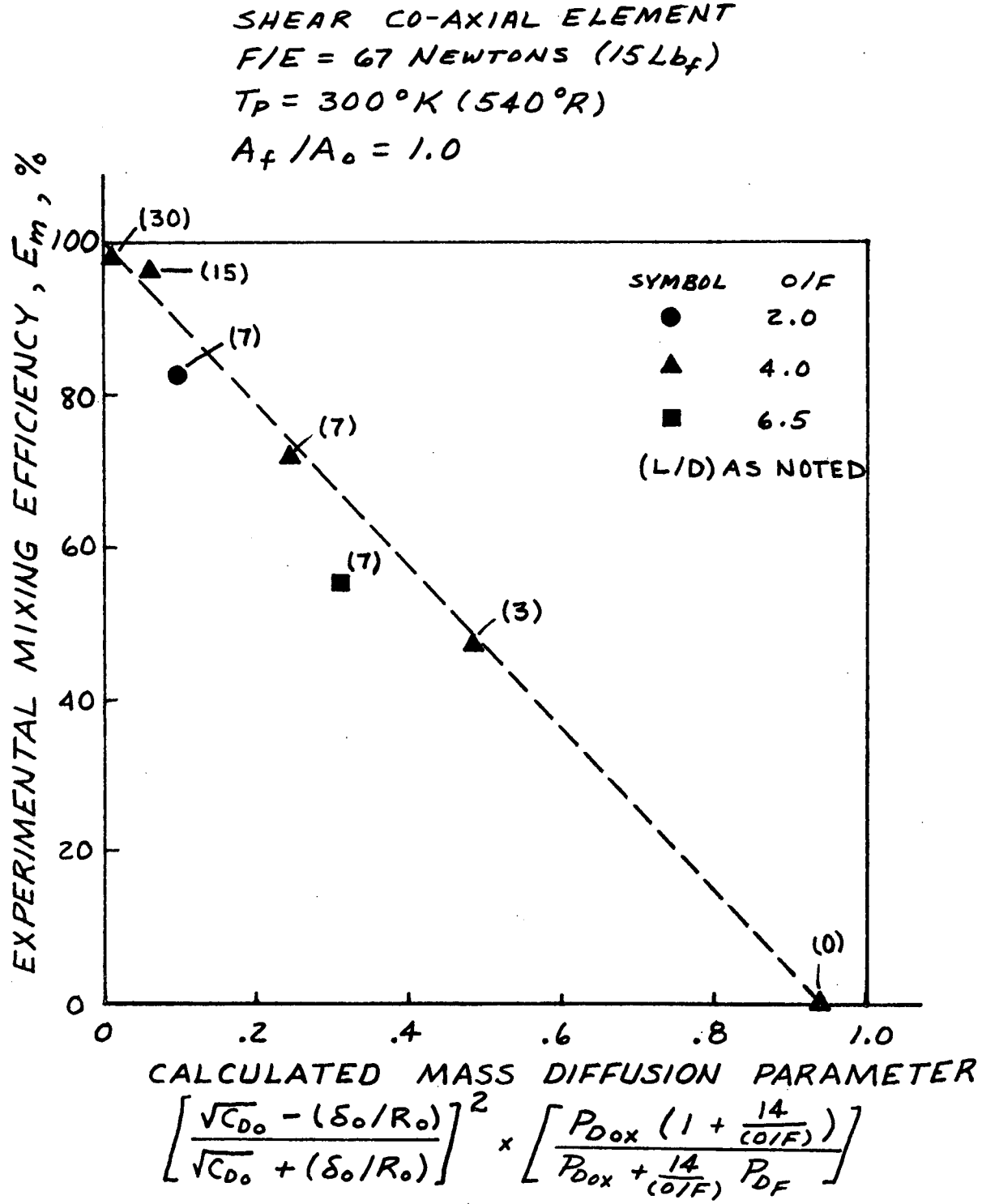

AXIAL LENGTH VARIATION OF MOLE FRACTION

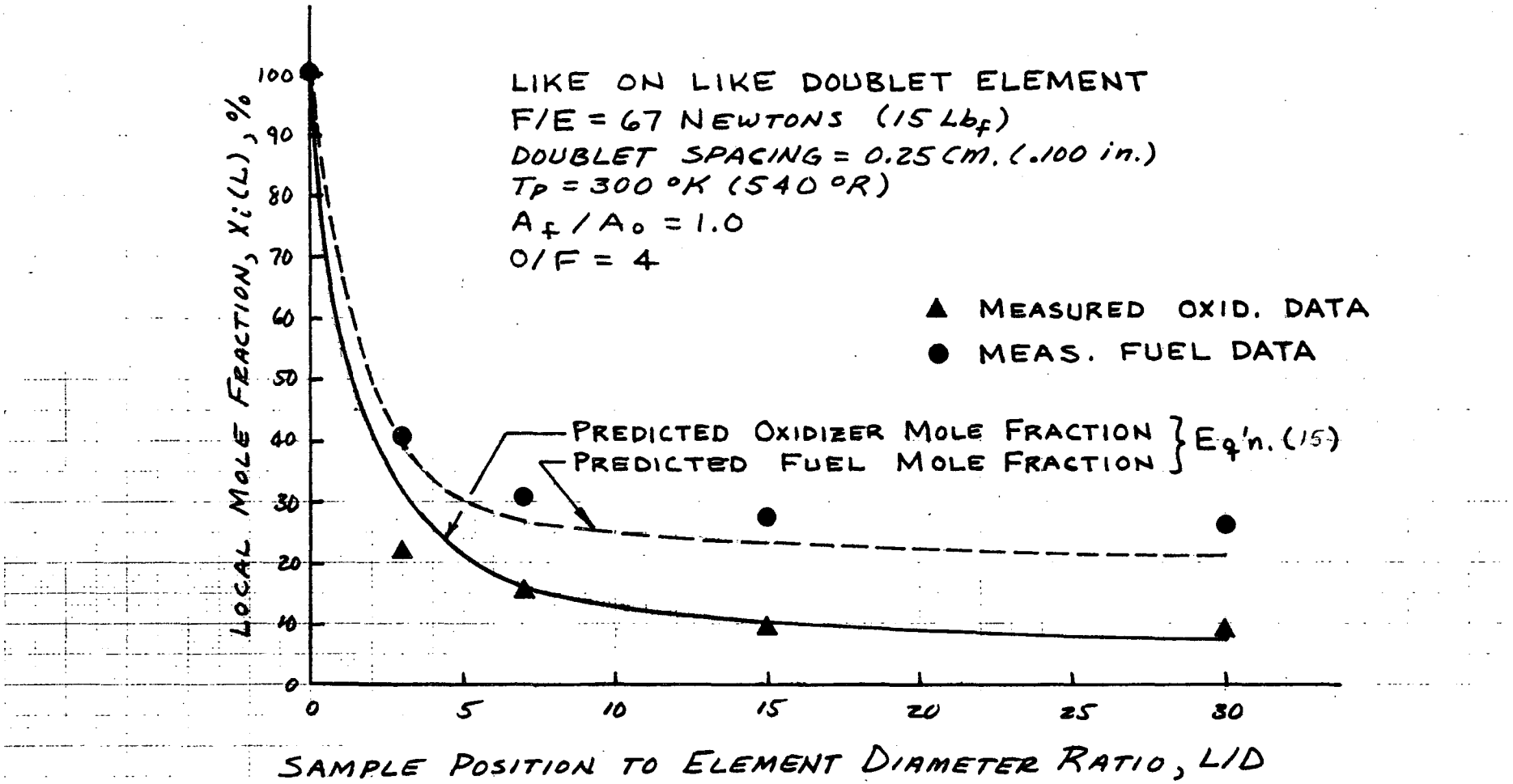

FIG 49

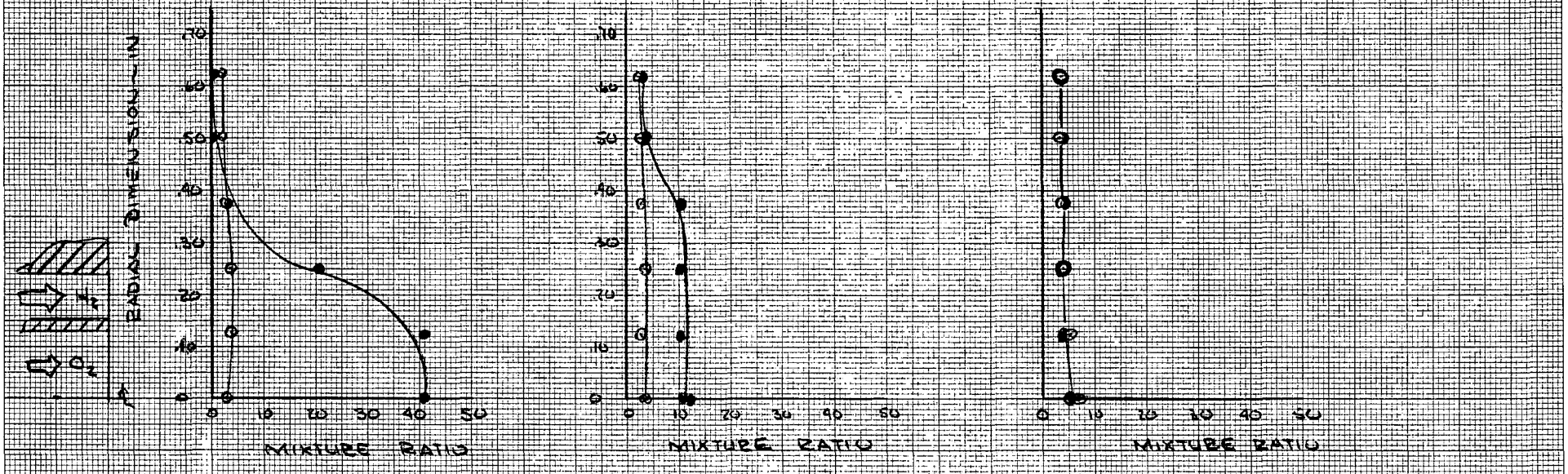

LENGTH = 3.03 IN, 7.65 CM
L/D = 8.7

LENGTH = 5.15 IN, 13.1 CM
L/D = 19.9

LENGTH = 7.17 IN, 18.20 CM
L/D = 27.4

OVERALL MIXTURE RATIO = 4
CHAMBER PRESSURE = ONE ATMOSPHERE
CLOSED SYBOLS ● HOT FLOW
OPEN SYBOLS ○ COLD FLOW

THE COMPARISON OF HOT & COLD MIXTURE RATIO PROFILES FOR A SWIRL COAXIAL ELEMENT

FIG. 50

SWIRL ELEMENT COMBUSTION

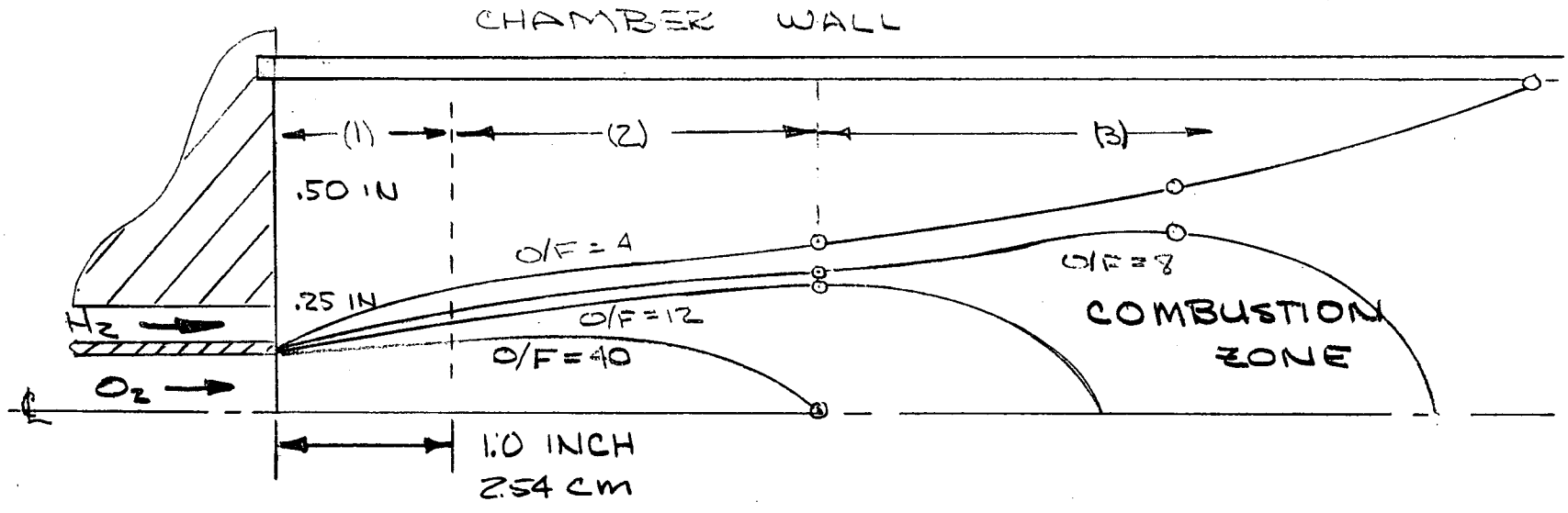

(1) REGION OF HIGH MASS TRANSFER; COMBUSTION INITIATION.

(2) REGION OF HIGH DIFFUSION RATES; PROBABLE COLLAPSE OF OXIDIZER HOLLOW CONE.

(3) CONTINUED ROTATION OF OXIDIZER-RICH CORE PROMOTES RADIAL DIFFUSION.

FIG. 51

HOT FIRE CHAMBERS

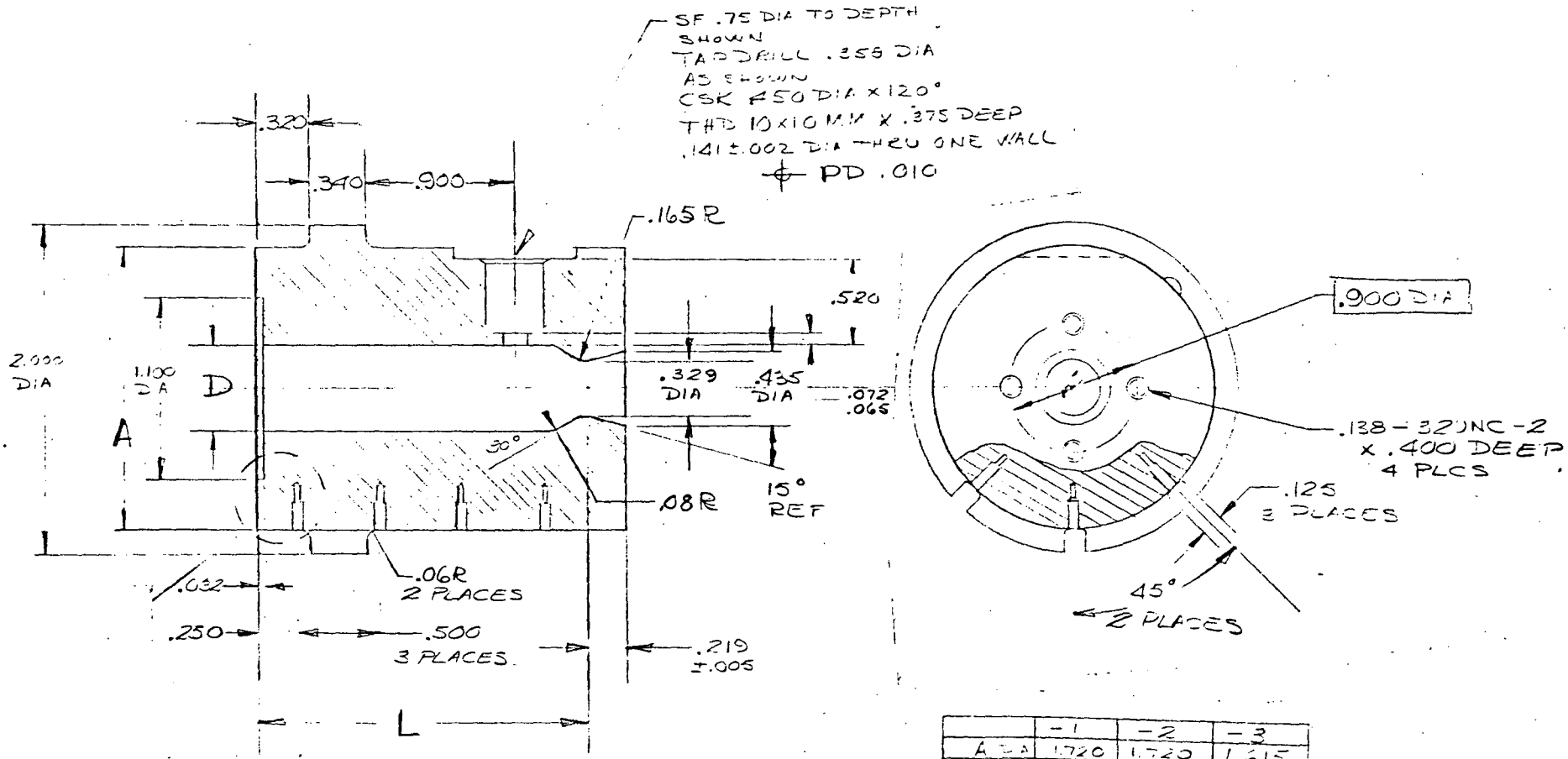

	-1	-2	-3
A DIA	1.720	1.720	1.615
B	.27	.27	.225
D DIA	.520	.520	.615
L	2.000	2.000	2.000

FIG. 52